Obstacle-resolving large-eddy simulation of dispersion in urban environments
Effects of stability and roughness geometry

Tomas, Jasper

DOI
10.4233/uuid:5d93a697-be49-4f63-b871-b763bc327139

Publication date
2016

Document Version
Final published version

Citation (APA)
Tomas, J. (2016). *Obstacle-resolving large-eddy simulation of dispersion in urban environments: Effects of stability and roughness geometry*. [Dissertation (TU Delft), Delft University of Technology]. https://doi.org/10.4233/uuid:5d93a697-be49-4f63-b871-b763bc327139

OBSTACLE-RESOLVING LARGE-EDDY SIMULATION OF DISPERSION IN URBAN ENVIRONMENTS

Effects of stability and roughness geometry

PROEFSCHRIFT

ter verkrijging van de graad van doctor
aan de Technische Universiteit Delft,
op gezag van de Rector Magnificus, prof. ir. K.C.A.M. Luyben;
voorzitter van het College voor Promoties,
in het openbaar te verdedigen op
vrijdag 8 juli 2016 om 12:30 uur

door

Jasper Michiel TOMAS
Werktuigbouwkundig Ingenieur
Universiteit Twente
geboren te Leiden

This dissertation has been approved by the

Promotor:	Prof. dr. H.J.J. Jonker
Copromotor:	Dr. ir. M.J.B.M. Pourquie

Composition of the doctoral committee:

Rector Magnificus	chairman
Prof. dr. H.J.J. Jonker	Delft University of Technology
Dr. ir. M.J.B.M. Pourquie	Delft University of Technology
Independent members:	
Prof. dr. E. Fedorovich	University of Oklahoma, USA
Prof. dr. ir. M. van Reeuwijk	Imperial College, UK
Prof. dr. M.C. Krol	Wageningen University
Prof. dr. A.P. Siebesma	Delft University of Technology
Prof. dr. ir. B.J. Boersma	Delft University of Technology

This research is supported by the Dutch Technology Foundation STW, which is part of the Netherlands Organisation for Scientific Research (NWO) and partly funded by the Ministry of Economic Affairs (project number 11989). Use is made of the computational resources of SURFsara with funding of NWO (project number SG-015).

Front cover:	Instantaneous temperature field in a stable boundary layer approaching urban terrain (Chapter 4)
Back cover:	Corresponding instantaneous concentration field emitted by a line source
Printed by:	Gildeprint – Enschede

ISBN 978-94-6186-675-2
An electronic version of this dissertation is available at
http://repository.tudelft.nl/

SUMMARY

There is an increasing demand for accurate predictions of urban air quality in order to quantify the health risks due to planned and existing pollutant emission sources. Therefore, predicting the transport of pollutants in urban environments is of great interest. However, current models for pollutant dispersion are incapable of accurately capturing the flow near the obstacles that make up the urban environment. Moreover, the effects of atmospheric stability on the flow in urban regions are largely unknown as the combination of flow over obstacles and stably stratified flow is a rather unexplored field.

The work presented in this thesis contains an investigation on this topic by means of large-eddy simulation (LES). The developed LES model contains an immersed boundary method (IBM) such that the flow around obstacles could be accurately resolved. In addition, methods to generate realistic turbulent velocity and temperature boundary layers were implemented, such that streamwise developing situations could be studied. The model was employed to investigate the flow and dispersion behaviour in regions where the character of the surface roughness changes from a rural to an urban type of roughness. Pollutant emissions from line sources were considered, where the pollutants were assumed to behave as a passive tracer.

Firstly, the effects of a single two-dimensional obstacle, a fence, on the flow and pollutant dispersion in neutral and stable boundary layers were studied. The validity of two simplifications was assessed; either neglect the presence of the obstacle, or neglect thermal stratification effects. It is concluded that both simplifications do not hold when pollutant dispersion is considered. In additon, it is found that for stable conditions the turbulence added by the obstacle remains present for a much greater distance than for neutral conditions.

Subsequently, the flow in a rural-to-urban roughness transition was investigated by considering a smooth-wall boundary layer approaching an array of cubical roughness elements. Both neutral and stable conditions were taken into account, and the effects on dispersion from a pollutant emission near the surface, as well as from an elevated source, were examined. It is found that the profile of the mean streamwise velocity component becomes neary indistinguishable from the fully-developed case after approximately 24 streets. However, this does not hold for stable conditions. In addition, the budget of turbulence kinetic energy reveals that buoyancy effects are reduced inside the internal boundary layer, which is induced by the roughness transition. Nevertheless, the buoyancy destruction term increases approximately linearly with height up to the value found for the smooth-wall flow. As a result in stable conditions the pollutant concentrations from emissions below the urban canopy are higher than for neutral conditions due to decreased advection and decreased internal boundary-layer growth.

Furthermore, the case of a rural-to-urban roughness transition was further investigated by focussing on the influence of the geometry of the roughness elements. The spanwise aspect ratio of the roughness elements was varied, and the results from the LES were compared with results acquired from simultaneous stereoscopic particle image velocimetry (PIV) and laser-induced fluorescence (LIF) measurements in water-tunnel experiments. It is found that both methods independently predict practically the same velocity and concentration statistics. In addition, the dominant mechanisms that govern pollutant dispersion were studied. In all cases in the first three streets the mean vertical pollutant flux out of the street canyons is dominated by the advective pollutant flux, after which the vertical pollutant flux shows similar behaviour as found for fully-developed cases. The mean flow structure that is responsible for street canyon ventilation was identified by means of linear stochastic estimation. This structure is characterized by low momentum fluid passing over the street canyons. Furthermore, the vertical length scale of this structure increases with increasing spanwise aspect ratio of the obstacles. While considering the various spanwise aspect ratios it was observed that a spanwise aspect ratio of two results in a relatively large surface drag that is related to a large-scale secondary flow.

The work in this thesis shows that obstacle-resolving LES can be used to investigate flow and pollutant dispersion in urban regions. Currently, the required computational resources for these simulations limit their use to dedicated pollutant studies and academic studies. Therefore, from the results obtained in this research perspectives are given on derived models that are expected to outperform current practical dispersion models.

SAMENVATTING

Er is een toenemende vraag naar nauwkeurige voorspellingen van luchtkwaliteit in stedelijke omgeving met als doel de gezondheidsrisico's van bestaande en toekomstige vervuilende emissies te kwantificeren. Het is daarom van belang de verspreiding van vervuilende stoffen in stedelijke gebieden goed te voorspellen. Echter, huidige verspreidingsmodellen zijn niet in staat om de stroming rond stedelijke bebouwing te beschrijven. Bovendien is er weinig bekend over de effecten van atmosferische stabiliteit in stedelijke gebieden, omdat de combinatie van luchtstroming over obstakels en stabiele condities nauwelijks is onderzocht.

Dit proefschrift bevat een onderzoek op dit gebied waarbij gebruik is gemaakt van 'large-eddy simulation' (LES). De ontwikkelde LES bevat een 'immersed boundary method' (IBM) zodat de stroming rond obstakels nauwkeurig kan worden opgelost. Daarnaast zijn methoden geïmplementeerd om realistische snelheids- en temperatuursgrenslagen te kunnen genereren, zodat situaties kunnen worden beschouwd waarin de stroming zich in de stroomrichting kan ontwikkelen. Het model is gebruikt om de stroming en de verspreiding te onderzoeken in gebieden waar het karakter van de oppervlakteruwheid verandert van 'landelijke ruwheid' naar 'stedelijke ruwheid'. Emissies van lijnbronnen zijn beschouwd, waarbij is aangenomen dat de vervuiling zich gedraagt als een passieve 'tracer'.

Allereerst zijn de effecten onderzocht van een enkel twee-dimensionaal obstakel; een scherm. De geldigheid van twee aannames is getoetst; óf de aanwezigheid van het obstakel verwaarlozen, óf de effecten van thermische stratificatie weglaten. De conclusie is dat beide aannames niet gegrond zijn wanneer verspreiding van vervuiling wordt beschouwd. Daarnaast blijkt dat voor stabiele condities de turbulentie die is toegevoegd door het obstakel over een grotere afstand standhoudt dan voor neutrale condities.

Vervolgens is de stroming over een landelijke-naar-stedelijke ruwheidstransitie onderzocht door een 'gladde wand' grenslaag te beschouwen die een rooster van kubische ruwheidselementen nadert. Zowel neutrale als stabiele condities zijn beschouwd en de invloed op de verspreiding van een bron dichtbij het oppervlak én van een verhoogde bron zijn bestudeerd. Het profiel van de snelheidscomponent in de stroomrichting is na ongeveer 24 straten niet te onderscheiden van de volledig ontwikkelde situatie. Dit is echter niet zo voor stabiele condities. Daarnaast laat het budget van de turbulente kinetische energie zien dat dichtheidseffecten zijn verminderd in de interne grenslaag, welke is onstaan door de ruwheidstransitie. Desalniettemin neemt de 'buoyancy-destructie' term bij benadering lineair toe in de hoogte, tot de waarde die geldt voor de stroming over een gladde wand. Voor emissies op een lokatie lager dan de obstakelhoogte is de concentratie voor stabiele condities hoger dan voor neutrale condities, ten gevolge van een lagere advectiesnelheid en een verminderde interne grenslaaggroei.

De situatie van een landelijke-naar-stedelijke ruwheidstransitie is verder bestudeerd door de invloed van de geometrie van de ruwheidselementen te onderzoeken. De lengte-breedte verhouding van de ruwheidselementen is gevarieerd en de resultaten zijn vergeleken met resultaten verkregen met stereoscopische 'particle image velocimetry' (PIV) metingen en 'laser-induced fluorescence' (LIF) metingen in watertunnelexperimenten. De simulaties en de experimenten laten onafhankelijk van elkaar nagenoeg dezelfde snelheids- en concentratiestatistieken zien. De dominante mechanismen die verantwoordelijk zijn voor verspreiding van vervuiling zijn onderzocht. In alle beschouwde situaties wordt de gemiddelde verticale concentratieflux in de eerste drie straten gedomineerd door de advectieve concentratieflux, waarna de verticale concentratieflux vergelijkbaar gedrag gaat vertonen als in de situatie voor een volledig ontwikkelde stroming. Daarnaast is door middel van linaire stochastische benadering de stromingsstructuur geïdentificeerd die verantwoordelijk is voor de ventilatie van straten. Deze structuur is gekarakteriseerd door een stromingsgebied van lage impuls die boven de straten passeert. De verticale lengteschaal van deze structuur neemt toe wanneer de breedte-lengte verhouding van de obstakels toeneemt. Daarnaast tonen de resultaten bij een breedte-lengte verhouding van twee een relatief grote oppervlakteweerstand die samenhangt met een secundaire stroming op grote schaal.

Het werk in dit proefschrift laat zien dat 'obstacle-resolving' LES gebruikt kan worden om de stroming en verspreiding in stedelijke gebieden te onderzoeken. Door de benodigde rekenkracht blijft op dit moment het gebruik van dergelijke simulaties beperkt tot specifieke verspreidingsstudies en academische studies. Daarom worden aan de hand van de resultaten uit dit onderzoek perspectieven geboden voor afgeleide modellen waarvan verwacht kan worden dat ze huidige praktische verspreidingsmodellen zullen overtreffen in nauwkeurigheid.

CONTENTS

NOMENCLATURE

ACRONYMS

ABL	atmospheric boundary layer
AR	aspect ratio
BL	boundary layer
CFD	computational fluid dynamics
CFL	Courant-Friedrichs-Lewy
D	Driver
DALES	Dutch Atmospheric Large-Eddy Simulation
DNS	direct numerical simulation
HWA	hot-wire anemometry
IBM	immersed boundary method
JPDF	joint probability density function
LDA	laser doppler anemometry
LES	large-eddy simulation
LIF	laser-induced fluorescence
LSE	linear stochastic estimate
MO	Monin-Obukhov
PIV	particle image velocimetry
PR	Periodic Roughness
RANS	Reynolds-averaged Navier-Stokes
Rh-B	Rhodamime B
Rh-WT	Rhodamime WT
RT	Roughness Transition
RMS	root mean square

SGS subgrid-scale

TBL turbulent boundary layer

TKE turbulence kinetic energy

UBL urban boundary layer

V Validation

LIST OF SYMBOLS

Latin Symbols

Symbol	Description	Units
A	advection of TKE	m^2/s^3
A_f	frontal area of all obstacles in a street	m^2
A_{street}	top view area of a single street	m^2
A_t	total top view area	m^2
A_s	total area of all surfaces in a street	m^2
b	obstacle width	m
c	dimensionless concentration	-
c^*	concentration	kg/m^3
c_0	empirical constant in MO similarity velocity profile	-
C_{1-5}	concentration from emission sources 1-5	kg/m^3
C_f	skin friction coefficient	-
C_{max}	maximum Courant number	-
C_p	form drag coefficient	-
c_s	experimental source concentration	kg/m^3
d	displacement height according to Jackson (1981)	m
d^*	zero-plane displacement height (log-law fit)	m
D_τ	average skin frictional drag	N/m^2
D_p	average form drag	N/m^2
D_{sgs}	dissipation of TKE in the SGS	m^2/s^3
D_v	resolved viscous dissipation of TKE	m^2/s^3
$E\left(k_y\right)$	spanwise energy spectrum	m^2/s^2

F_τ	average skin friction force	N
F_p	average form drag force	N
g	gravitational acceleration	m/s^2
$g_i = (0, 0, -g)$	gravitational acceleration vector	m/s^2
H	shape factor (δ_1/δ_2)	-
h	obstacle height	m
k_y	spanwise wavenumber	$1/m$
L	Obukhov length scale	m
l	obstacle length	m
l_x, l_y	experimental emission source dimensions in x and y	m
L_x, L_y, L_z	computational domain dimensions in x, y, and z	m
$l_x^{u_i u_i}$, $l_y^{u_i u_i}$	integral length scales in x- and y-direction	m
L_R	reattachment length downstream of the obstacle	m
$\mathcal{L}_x$, $\mathcal{L}_z$	length scales of low momentum region in x and z	m
N_x, N_y, N_z	no. of grid cells in each dimension for the domain	-
n_x, n_y, n_z	no. of grid cells in each dimension for a cube	-
p	pressure	Pa
P_b	TKE production by buoyancy fluctuations	m^2/s^3
P_t	TKE production by shear	m^2/s^3
Pr	Prandtl number	-
Pr_{sgs}	SGS Prandtl number	-
Q	mass flow rate of the emission source	kg/s
q_i	SGS scalar flux vector for θ and c^*	-
Re	Reynolds number	-
Re_τ	wall-friction Reynolds number	-
Ri	bulk Richardson number	-
$\mathrm{Ri}_{\mathrm{grad}}$	gradient Richardson number	-
Ri_{f}	flux Richardson number	-
$R_{u_i u_i}$	two-point correlation of u_i	m^2/s^2
Sc	Schmidt number	-
Sc_{sgs}	SGS Schmidt number	-
S_{ij}	rate of strain tensor	1/s
$\mathcal{S}$	volumetric source term for scalars ϕ	-
T	time scale	s
t	time	s

T_e	eddy turnover time scale	s
T_p	TKE transport by pressure fluctuations	m^2/s^3
T_{sgs}	TKE transport by SGS stresses	m^2/s^3
T_t	TKE transport by turbulent velocity fluctuations	m^2/s^3
T_v	TKE transport by viscous stresses	m^2/s^3
Δt	timestep	s
U	bulk velocity	m/s
$\Delta\overline{u}$	difference in velocity with smooth-wall case	m/s
$u_i = (u, v, w)$	velocity in x-, y-, and z-direction	m/s
U_h	mean undisturbed velocity at obstacle height	m/s
u_τ	friction velocity	m/s
U_∞	freestream velocity	m/s
$x_i = (x, y, z)$	Cartesian coordinates	m
x_s	x-coordinate of emission source location	m
x_R	x-coordinate of downstream reattachment location	m
$\Delta x_i = (\Delta x, \Delta y, \Delta z)$	increment in Cartesian coordinates	m
z_0	roughness length scale	m

Greek Symbols

Symbol	Description	Units
α_θ	thermal diffusivity	m^2/s
α_{c^*}	diffusivity of concentration in the fluid	m^2/s
α_{sgs}	subgrid diffusivity	m^2/s
β	coefficient of thermal expansion	1/K
δ	boundary-layer depth	m
δ_0	boundary-layer depth at domain inlet	m
δ_1	displacement thickness	m
δ_2	momentum thickness	m
δ_{99}	BL depth defined by $\overline{u}\,(z = \delta_{99}) = 0.99U_\infty$	m
δ_i	internal boundary-layer depth	m
δ_{ij}	Kronecker delta	-
δ_T	thermal boundary-layer depth	m

θ	temperature	K
θ_0	temperature at the ground	K
θ_∞	temperature in the freestream	K
$\Delta\overline{\theta}$	difference in temperature with smooth-wall case	K
κ	von Kármán constant	-
λ	obstacle area density	-
Λ	length scale of dominating flow structure	m
λ_f	frontal area density	-
λ_p	plan area density	-
μ	dynamic viscosity	Pa·s
ν	kinematic viscosity	m^2/s
ν_{sgs}	SGS viscosity	m^2/s
Π	modified pressure	$\mathrm{m}^2/\mathrm{s}^2$
ρ	density	kg/m^3
τ_{ij}	SGS stress tensor	Pa
ϕ	scalars θ and c^*	-
ϕ_s	volume flow rate of emission source	m^3/s
ψ	prognostic variables u_i, θ, c^*	-

Operator Symbols

Symbol	Description	Units
$(..)''$	unresolved (subgrid-scale) motion	-
$(..)'$	turbulent fluctuation	-
$\widetilde{(..)}$	filtering operation	-
$\overline{(..)}$	temporal average, i.e. 'mean'	-
$\overline{(..)}^\mathrm{e}$	conditional average	-
$\overline{\langle..\rangle}$	spatial average	-

1 INTRODUCTION

1.1 BACKGROUND

The number of people living in urban areas compared to the number of people living in rural areas is increasing (United Nations, 2014). This growth of urban environments, so-called 'urbanization', also leads to an increase of pollutant emissions near populated areas. In order to quantify the health risks due to planned and existing emission sources there is an increasing demand for accurate predictions of urban air quality. Therefore, predicting the transport of pollutants in urban environments is of great interest.

In addition, in the unfortunate event of a release of hazardous material in the atmosphere, such as during fires, chemical spills, or nuclear disasters, an accurate prediction of the transport of these substances in urban regions is an important part of emergency response, as it can be used in deciding if and where evacuation should be initiated.

The modelling of the transport of contaminants in the atmosphere due to advection and turbulent diffusion, i.e. pollutant dispersion, is often done by assuming that the pollutant concentration takes the form of a Gaussian distribution. Such a 'Gaussian plume' is an analytical solution of a strongly idealized form of the pollutant transport equation for statistically steady conditions (Roberts, 1923). Since it is an analytical solution, it requires low computational effort to find the concentration field for a specific case. This makes it an appealing model when multiple situations need to be considered, e.g. several wind directions or atmospheric conditions. Most dispersion models that are approved by national authorities for air quality and risk assessment, are based on the Gaussian plume formulation (e.g. in the Netherlands the 'Nieuw Nationaal Model' is used (Projectgroep Revisie Nationaal Model, 1998; Minister VROM, 2007)).

However, the Gaussian plume solution is not entirely correct since its underlying assumptions do not hold. For example, the model assumes that the mean wind and the turbulence are uniform, which is not valid in atmospheric flows. Nevertheless, by means of empirical constants the model is used to approximate plumes from elevated pollutant emissions. However, the underlying assumptions limit the model from being used for pollutant emissions and dispersion in urban regions. In addition, there are no alternative models for urban regions that have a similar simplicity and range of applicability as the Gaussian plume model for rural environments. Some

attempts have been made to make dispersion models for general urban situations, mostly based on the local geometry of buildings and empirical relations (Berkowicz, 2000; Soulhac et al., 2011; Barnes et al., 2014). Unfortunately, they do not allow for a more detailed analysis of the flow and disperion behaviour for specific cases, nor can they be applied for all atmospheric conditions.

The reason that mostly empirical models are used instead of theoretical models, is because the fluid mechanics in urban environments are not fully understood. Dispersion of pollutants can occur through mean advection in streets as well as through turbulent mixing of the flow. However, buildings induce complex flow features, which make parameterization of the mean flow and turbulence characteristics difficult. Besides that, the heterogeneity of the surface roughness increases this complexity. Furthermore, the influence of atmospheric stability on the flow in urban regions is largely unknown.

Consequently, there is a need for a proper understanding of the flow and the dispersion behaviour in urban environments. One approach to improve our knowledge on these topics is to do real-life measurements (Allwine and Leach, 2007; Wood et al., 2010; Barlow, 2014). However, assessing the influence of specific parameters proves to be difficult, because the atmospheric conditions are variable in time, and the spatial resolution and size of the measurements are often limited. Therefore, the approach used in this thesis is to address the case of urban pollutant dispersion by means of simulation, i.e. by solving the equations that govern the relevant physics. The method of *large-eddy simulation* (LES) is used, which allows for an accurate and controlled investigation.

1.2 SCOPE AND OBJECTIVES

The focus of this study is the transport of pollutants, and consequently the flow, in the region of urban roughness. The lower part of the *atmospheric boundary layer* (ABL) that is mostly affected by the interaction with the surface is called the 'surface layer' (Stull, 1988). Specifically, the boundary layer in urban regions is called the *urban boundary layer* (UBL) (Barlow, 2014). Pollutant dispersion in the ABL is largely dominated by turbulence; the fluctuations in the three-dimensional wind field. There are two sources of turbulence in the ABL: turbulence produced by strong velocity gradients and turbulence produced by buoyancy differences. The ratio of these two sources in the production of turbulence kinetic energy (TKE) is called the flux Richardson number

$$\mathrm{Ri_f} = \frac{\beta g \overline{w'\theta'}}{\overline{u'w'}\,\partial\overline{u}/\partial z}, \tag{1.1}$$

where g is the gravitational acceleration, β is the coefficient of thermal expansion, $\overline{w'\theta'}$ is the vertical turbulent heat-flux, and $\overline{u'w'}\,\partial\overline{u}/\partial z$ is the shear-production term (in the TKE budget equation this term contains a minus sign, see Eq. 4.10 in Sect. 4.4.4). If heat transfer is upward ($\overline{w'\theta'} > 0$), $\mathrm{Ri_f}$ is negative, because $\overline{u'w'}\,\partial\overline{u}/\partial z < 0$, in general. For these conditions the flow is called *unstable*, or *convective*, because the

enhanced vertical motions increase the level of turbulence. If there is no heat transfer ($\overline{w'\theta'} = 0$), $\mathrm{Ri_f}$ is zero, which is called *neutral*, or *neutrally buoyant*. For these conditions the flow is completely dominated by shear production. Finally, when the heat transfer is downward ($\overline{w'\theta'} < 0$), $\mathrm{Ri_f}$ is positive, which is called *stable*. For these conditions the downward heat flux tends to decrease vertical motions and consequently turbulence is destroyed. As a result, stable flows show a more 'layered' flow structure, such that these conditions are often called *stratified*. Observations show that when $\mathrm{Ri_f} \gtrsim 0.2$ turbulence cannot be sustained. In view of pollutant dispersion, one can understand that for unstable conditions concentrations decay fast with increasing distance from the emission source, because turbulent mixing is strong. On the other hand, for stable conditions concentrations can remain high for longer distance, because turbulent mixing is weaker. For this reason, pollutant releases during stable conditions pose the largest risk to public health. Therefore, in this study stable conditions are compared to neutral conditions, i.e. cases where $\mathrm{Ri_f} \geqslant 0$ are considered.

Obstacles tend to increase the turbulence production in the boundary layer, because they induce strong velocity gradients. Consequently, stable boundary layers become less stratified when surface roughness is increased. For this reason, in practice the UBL is often assumed to be purely dominated by shear production, hence they are considered neutral. It is unclear what the conditions are for this assumption to be correct. Moreover, when the surface characteristics change from e.g. a rural to an urban environment, the boundary layer needs to adapt to this new surface roughness. It is not known how much distance is needed for stable flow to adapt to this change in roughness and how pollutant dispersion is affected by this transition. Therefore, the following objectives are formulated:

- Determine the flow field, surface forces, and internal boundary layer growth for rural-to-urban transitions in neutral and stable conditions.
- Assess to what extent stratification effects are diminished by the added turbulence due to urban roughness elements.
- Identify the dominating mechanisms of pollutant dispersion near roughness transitions in both neutral and stable conditions.
- Develop a method to simulate these cases realistically and accurately.

1.3 STRUCTURE OF THE THESIS

The thesis is based on three journal papers, which are presented (in a slightly adapted form) in Chapters 3, 4, and 5. As such, these chapters are self-contained and therefore some redundancy in the thesis as a whole is inevitable.

The numerical method is decribed in Chapter 2. First of all, the governing equations for the LES are derived from the conservation equations for mass, momentum, and energy. Furthermore, the details of the numerical model are described, such as the spatial and temporal discretization, the pressure-correction method, the immersed boundary method, and the generation of inflow turbulent boundary layers.

In Chapter 3 the effects of a two-dimensional fence on the development of a smooth-wall turbulent boundary layer are studied for both neutral and stably stratified conditions. In addition, the influence on pollutant dispersion of both the obstacle and the applied level of stratification are investigated.

In Chapter 4 the investigation is extended to regions with multiple obstacles, i.e. regions where the surface roughness changes from rural to urban characteristics. The main interest is to investigate the influence of stable stratification on the flow and on pollutant dispersion. The urban region is made up of an array of cubical obstacles. First, the model is validated for this type of roughness by applying it to a UBL test case described in the literature and comparing the results with experimental data. Thereafter, roughness transition simulations are done, for which the surface forces are investigated and the budgets of resolved turbulence kinetic energy are given. A comparison is made with fully-developed flow over the same geometry. Finally, the effects on pollutant dispersion are studied by considering the pollutant flux out of each street.

Chapter 5 also considers the transition from rural-to-urban roughness, but here the focus of interest is the influence of the geometry of the obstacles that make up the urban environment. The same configuration as in Chapter 4 is considered, except that the spanwise aspect ratio of the obstacle is varied. Neutrally buoyant conditions are applied in all cases. Moreover, for three cases a comparison is made with experimental data from water-tunnel experiments. The velocity and concentration statistics are investigated, and the flow structure that is responsible for the ventilation of street canyons is identified and compared for several values of obstacle aspect ratios.

Finally, in Chapter 6 the conclusions drawn from the research as a whole are presented. Furthermore, recommendations are given for further research.

2

NUMERICAL METHOD

In this chapter the equations for the large-eddy simulations (LES) are derived from the governing equations. Furthermore, the details of the numerical model are described. The model is based on DALES 3.2 (Heus et al., 2010), but it has been modified in multiple areas. Differences include the applied subgrid model, the use of 'inflow-outflow' boundary conditions, and the implementation of an immersed boundary method. These topics are discussed in the second part of this chapter.

2.1 GOVERNING EQUATIONS

The equations that describe the motions of a fluid are based on conservation of mass, momentum, and energy. The first, also called the continuity equation, reads

$$\frac{\partial \rho}{\partial t} + \frac{\partial \rho u_i}{\partial x_i} = 0, \tag{2.1}$$

where ρ is the fluid density, $u_i = (u, v, w)$ are the velocity components, and the index i (and further on also indices j and k) represents the three cartesian coordinates x, y, and z. Furthermore, the Einstein summation convention is used, i.e. repeated indices imply a summation. When the fluid can be considered incompressible Eq. 2.1 reduces to

$$\frac{\partial u_i}{\partial x_i} = 0, \tag{2.2}$$

which is a good approximation as long as the velocity components u_i are much smaller than the speed of sound propagation in the fluid. In addition, it requires that the vertical motions should be small compared to the scale over which the fluid density changes due to gravity.

The conservation of momentum is described by the Navier-Stokes equations:

$$\rho \frac{\partial u_i}{\partial t} + \rho u_j \frac{\partial u_i}{\partial x_j} = \rho g_i - \frac{\partial p}{\partial x_i} + \mu \frac{\partial^2 u_i}{\partial x_j^2}, \tag{2.3}$$

where the z coordinate represents the upward direction such that $g_i = (0, 0, -g)$ is the vector describing the gravitational acceleration, p is the pressure, and μ is the fluid dynamic viscosity, which is assumed to be constant. The equations, one for

each dimension, describe the change of motion of an infinitely small fluid element based on the forces acting on it. The left-hand side of Eq. 2.3 contains the material derivative of the fluid element, while the right-hand side contains the gravitational forces, pressure forces and viscous forces acting on it per unit volume.

The density ρ is a function of the temperature θ. Based on conservation of energy the transport equation for θ is

$$\frac{\partial \theta}{\partial t} + u_j \frac{\partial \theta}{\partial x_j} = \alpha_\theta \frac{\partial^2 \theta}{\partial x_j^2}, \tag{2.4}$$

where α_θ is the diffusion coefficient of heat in the fluid. The transport of pollutants is described by a similar equation by considering the pollutant concentration c^*

$$\frac{\partial c^*}{\partial t} + u_j \frac{\partial c^*}{\partial x_j} = \alpha_{c^*} \frac{\partial^2 c^*}{\partial x_j^2}, \tag{2.5}$$

where α_{c^*} is the diffusion coefficient of the pollutant in the fluid. In addition, it is assumed that the pollutant is transported passively with the flow, that there is no deposition, and that there are no chemical reactions.

We simplify the equations by approximating the influence of density variations on the flow. A detailed derivation can be found in standard works on stratified turbulent flow, e.g. Turner (1973) and Tennekes and Lumley (1972). Here a concise derivation is given. First, let us assume the considered flow can be described by fluctuations around the reference state of a fluid in rest: $p_0 + p'$, $\rho_0 + \rho'$, and $\theta_0 + \theta'$, where p', ρ', and θ' are small fluctuations around the reference state $\theta_0 =$ constant, and $\partial p_0 / \partial z = -\rho_0 g$, which is the hydrostatic law. Substitution in Eq. 2.3 and dividing by $1/\rho_0$ gives

$$\frac{\partial u_i}{\partial t} + u_j \frac{\partial u_i}{\partial x_j} = \frac{\rho'}{\rho_0} g_i - \frac{1}{\rho_0} \frac{\partial p'}{\partial x_i} + \nu \frac{\partial^2 u_i}{\partial x_j^2}, \tag{2.6}$$

where $\nu = \mu / \rho_0$ is the fluid kinematic viscosity. Furthermore, because $\rho' / \rho_0 \ll 1$ all terms containing ρ' / ρ_0 are neglected, except the gravitational force term $(\rho' / \rho_0)\, g_i$. The reason is that the fluctuations in buoyancy are large compared to the fluctuations in inertia, and can therefore not be neglected. Finally, we use the linearized equation of state to link ρ to θ (Eq. 2.4):

$$\rho = \rho_0 - \beta \rho_0 \left(\theta - \theta_0 \right), \tag{2.7}$$

where β is the coefficient of thermal expansion, which is $1/\theta_0$ for an ideal gas, as is taken here. Therefore, Eq. 2.6 becomes:

$$\frac{\partial u_i}{\partial t} + u_j \frac{\partial u_i}{\partial x_j} = -\frac{\theta}{\theta_0} g_i - \frac{1}{\rho_0} \frac{\partial p}{\partial x_i} + \nu \frac{\partial^2 u_i}{\partial x_j^2} \tag{2.8}$$

Equations 2.2, 2.4, and 2.8 are called the Boussinesq equations, named after Boussinesq, who introduced this approximation of the effects of variable density (Boussinesq,

1903). The equations are also valid for the flow of a gas when the compressibility of the gas is taken into account. This is achieved if θ is interpreted as the potential temperature, which is defined as the temperature a fluid parcel would acquire if adiabatically brought to a reference temperature.

2.2 LARGE-EDDY SIMULATION

Equations 2.2, 2.4, and 2.8 contain five unknowns; u_i, p, and θ. Therefore, in theory the discretized form of these five equations can be solved after applying boundary conditions and initial conditions. However, such direct numerical simulation (DNS) is not feasible for atmospheric flows. The reason is that atmospheric flows, just as most turbulent flows in reality, are characterized by a large Reynolds number, i.e. the turbulent motions occur at a large range of scales. To properly capture the dynamics of these turbulent motions the resolution of the computational grid should allow all motions to be resolved. However, their length scales range from the largest turbulent structures in the boundary layer down to the scales where turbulence kinetic energy is dissipated into heat due to the viscosity of the fluid. This occurs at the Kolmogorov scale η (Kolmogorov, 1991). In atmospheric boundary layers the largest turbulent motions can be in the order of 10^3 m, while η for these flows is around 10^{-3} m. DNS at such a large scale is not possible with current computational capabilities and it is expected that this will not change in the near future. For this reason, the method of large-eddy simulation (LES) is used in this thesis. LES involves solving the equations of motion on a computational grid that resolves the energetically dominant part of the range of turbulent motions, i.e. the large eddies, while the small-scale motions are parameterized. Even then, the range of scales is too large to solve computationally. Therefore, a common approach in atmospheric LES studies is to use 'wall functions'; to model the flow near the ground where most resolution is required to capture the strong gradients in velocity. However, since this research focusses on the near-wall region that contains the urban geometry, wall-functions are not used, and the flow is resolved up to the ground. To make the simulations feasible, the considered Reynolds number is approximately three orders of magnitude smaller than in reality. Nonetheless, the Reynolds number of the approaching flow is still in the range of laboratory-scale experiments: $\mathrm{Re}_\tau = u_\tau \delta / \nu = 2 \times 10^3$, where $u_\tau = \sqrt{\nu \partial u / \partial z}$ is the friction velocity and δ is the boundary-layer depth. In addition, experimental investigations have shown that Reynolds number effects are marginal for cases similar to those considered in this thesis (Huppertz and Fernholz, 2002; Castro, 1979; Cheng and Castro, 2002b).

The method of LES was first introduced by Smagorinsky (1963) and Lilly (1962), while the first three-dimensional LES explorations for atmospheric flows were done by Deardorff (1970). Further influential research on LES includes the work of Schumann (1975) and Mason and Callen (1986) on the modelling of the unresolved scales of turbulence in LES. For a detailed description of LES modelling the reader is referred to textbooks on turbulence and LES, e.g. Pope (2000). Here, the LES model developed and used in this study is discussed.

The LES approach implies that the variables that describe the flow are spatially filtered, either explicitly by a prescribed filter, or implicitly by the chosen grid size, as is done in the currently employed method. The underlying assumption is that the modelled part of the turbulence is isotropic. Hence, the prognostic variables become $u_i = \widetilde{u}_i + u_i''$, $p = \widetilde{p} + p''$ and $\theta = \widetilde{\theta} + \theta''$, where $\widetilde{(..)}$ denotes the filtered part and $(..)''$ denotes the unresolved part contained in the subgrid-scale (SGS). Substitution in the Boussinesq equations (Eqs. 2.2, 2.4, 2.8) and neglecting terms containing single occurrences of u_i'', p'' and θ'', results in

$$\frac{\partial \widetilde{u}_i}{\partial x_i} = 0, \tag{2.9}$$

$$\frac{\partial \widetilde{u}_i}{\partial t} = -\frac{\partial}{\partial x_j}\left(\widetilde{u}_i \widetilde{u}_j\right) - \frac{1}{\rho_0}\frac{\partial \widetilde{p}}{\partial x_i} + \frac{g}{\theta_0}\widetilde{\theta}\delta_{i3} + \nu\frac{\partial^2 \widetilde{u}_i}{\partial x_j^2} - \frac{1}{\rho_0}\frac{\partial \tau_{ij}}{\partial x_j}, \tag{2.10}$$

$$\frac{\partial \widetilde{\phi}}{\partial t} = -\frac{\partial}{\partial x_j}\left(\widetilde{\phi}\widetilde{u}_j\right) + \alpha_\phi\frac{\partial^2 \widetilde{\phi}}{\partial x_j^2} - \frac{\partial q_j}{\partial x_j} + \mathcal{S}, \tag{2.11}$$

where the advective terms in Eq. 2.10 and Eq. 2.11 are written in conservative form using continuity (Eq. 2.9) and δ_{i3} is the Kronecker delta. In addition, Eq. 2.11 describes the filtered transport equation for the scalars ϕ, which are the temperature θ and the pollutant concentration c^*. Furthermore, $\mathcal{S}$ represents a volumetric heat source in the transport equation for θ (used in streamwise periodic simulations as discussed in Sect. 4.2.4.2), while it is a concentration source in the transport equation for c^*. Effectively, the filtering operation results in the unknown SGS stress tensor $\tau_{ij} = \rho_0\left(\widetilde{u_i u_j} - \widetilde{u}_i\widetilde{u}_j\right)$ in Eq. 2.10 and the unknown SGS scalar flux vector $q_i = \widetilde{\phi u_i} - \widetilde{\phi}\widetilde{u}_i$ in Eq. 2.11. Closure of the momentum equations is achieved by relating the SGS stresses to the resolved velocity components by means of the Boussinesq hypothesis (Boussinesq, 1877), such that the SGS stresses are treated in a similar way to the viscous stresses;

$$\frac{\tau_{ij}}{\rho_0} = -2\nu_{sgs}\widetilde{S}_{ij} + \frac{\tau_{kk}\delta_{ij}}{3\rho_0}, \tag{2.12}$$

which is called the 'eddy-viscosity' SGS model, where ν_{sgs} is the SGS viscosity (or eddy viscosity), $\widetilde{S}_{ij} = \frac{1}{2}\left(\partial\widetilde{u}_i/\partial x_j + \partial\widetilde{u}_j/\partial x_i\right)$ is the rate of strain tensor based on the filtered velocity components, and τ_{kk} is the trace of the SGS stress tensor. The SGS normal stresses require no modelling as they are lumped into $\widetilde{p}/\rho_0$. However, the deviatoric part of τ_{ij} requires a model to predict ν_{sgs}. In all simulations discussed in this thesis the eddy-viscosity SGS model of Vreman (2004) is used, which has the advantage over the standard Smagorinsky-Lilly model (Smagorinsky, 1963; Lilly, 1962) that no wall-damping is required to reduce the SGS energy near walls. In addition, while the Smagorinsky-Lilly model tends to damp turbulence in transitional flows,

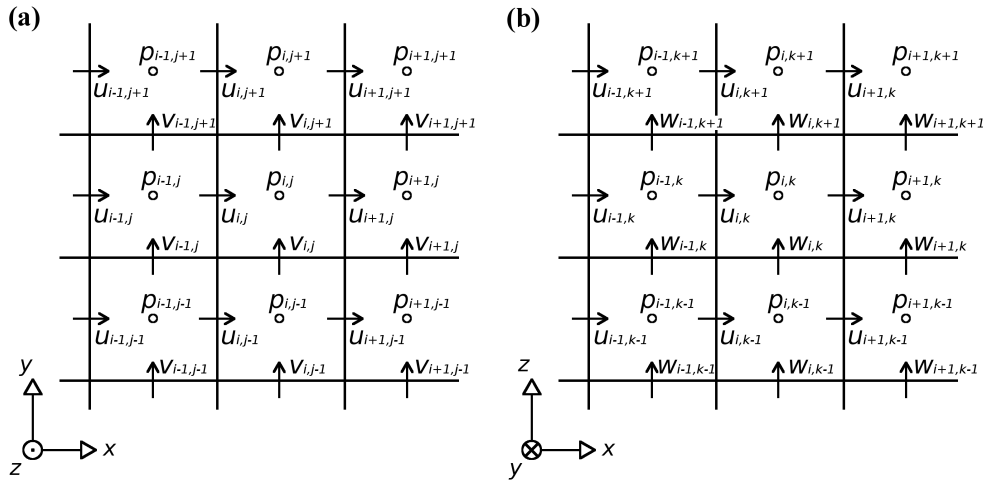

Figure 2.1: Structured 'staggered' grid with u, v, and w evaluated at the cell faces, while all scalars (here p is shown) are evaluated at the cell centers indicated by the circles. The relative position of the cells is indicated by the indices i, j, and k. A part of the grid is shown in the $x-y$ plane (a) and in the x-z plane (b).

the Vreman model does not. This makes it more suitable for simulating flows in which laminar-to-turbulence transitions can occur.

Furthermore, the SGS scalar flux vector q_i is modelled as

$$q_i = -\alpha_{sgs} \frac{\partial \widetilde{\phi}}{\partial x_i}, \tag{2.13}$$

where the SGS diffusivity α_{sgs} is related to the SGS viscosity ν_{sgs} by the SGS Prandtl number $\mathrm{Pr}_{sgs} = \nu_{sgs}/\alpha_{sgs}$. In all simulations in this thesis Pr_{sgs} was set to 0.9, equal to the turbulent Prandtl number found in the major part of the turbulent boundary layer in DNS studies by Jonker et al. (2013). In addition, $\mathrm{Pr} = \nu/\alpha_\theta = 0.71$ was used, corresponding to air. Note that for c^* the same diffusivity is used as for θ, which means the Schmidt number $\mathrm{Sc} = \nu/\alpha_{c^*}$ is assumed equal to Pr.

In the rest of this thesis the $\widetilde{(..)}$ symbol is omitted for clarity; the $\overline{(..)}$ symbol represents temporal averaging and $\langle .. \rangle$ denotes spatial averaging. If a spatial averaged quantity is given it is indicated over which dimension(s) this spatial average is taken.

2.3 NUMERICAL MODEL

2.3.1 *Spatial Discretization*

The numerical method involves finding solutions of Eqs. 2.9, 2.10, and 2.11 at a finite number of locations in space and time. Firstly, the equations are discretized in

space by using second-order central-differencing for all spatial derivatives. The only exception is the discretization of the advective terms in the transport equation of c^*, for which the second-order κ scheme (Hundsdorfer et al., 1995) is used to ensure positivity. The discretization is done such that conservation of mass, momentum, and energy is satisfied. In Fig. 2.1 it is shown that a structured 'staggered' grid is employed in order to avoid odd-even decoupling between pressure and velocity, i.e. u_i is evaluated on the cell faces, while p, θ, and c^* are evaluated at each cell center. Furthermore, the model allows grid stretching in the streamwise (x) and vertical (z) directions, which means the grid can be locally refined in those directions.

2.3.2 *Time Integration and Pressure-Correction Method*

Subsequent solutions of the discretized form of Eqs. 2.9, 2.10, and 2.11 are found by integrating each solution in time for a timestep Δt. This is achieved by means of an explicit third-order Runge-Kutta time integration scheme (Wicker and Skamarock, 2002). If ψ represents the prognostic variables u_i, θ, and c^*, this scheme reads

$$\psi^{n+1} = \psi^n + \sum_{s=1}^{3} \Delta t_s \left(\frac{\partial \psi}{\partial t} \right)_s, \tag{2.14}$$

where index n indicates steps in physical time and index s denotes evaluations at the intermediate steps $t_n + \Delta t_s$, where $\Delta t_1 = \Delta t/3$, $\Delta t_2 = \Delta t/2$, and $\Delta t_3 = \Delta t$. After spatial discretization of Eq. 2.11 the time derivatives of scalars ϕ are expressed in terms of known quantities such that a new solution can be found with Eq. 2.14. Finding $(\partial u_i/\partial t)_{s+1}$ requires some additional steps, because the updated velocity field needs to satisfy Eq. 2.9 and Eq. 2.10 simultaneously. For this reason the method of 'pressure-correction' is employed. Firstly, $(\partial u_i/\partial t)_{s+1}$ is predicted using the known velocity and pressure field (at step s). Secondly, a correction is applied to the pressure-gradient term to satisfy mass conservation (Eq. 2.9) for the new velocity field, such that the final expression becomes

$$\left(\frac{\partial u_i}{\partial t} \right)_{s+1} \approx \frac{u_i^{s+1} - u_i^n}{\Delta t_{s+1}} = -\frac{\partial \Pi^s}{\partial x_i} - \frac{\partial \Pi^*}{\partial x_i} + B_s + A_s + D_s, \tag{2.15}$$

where $\Pi = \left(p + \tau_{kk}\delta_{ij}/3\right)/\rho_0$ and $\partial \Pi^*/\partial x_i$ represents the correction term. Furthermore, B_s, A_s, and D_s represent the buoyancy, advection, and diffusion terms for step s, respectively. Equation 2.15 is solved by splitting the equation into a part with terms on step s, i.e. the prediction, and a part containing the unknown pressure correction:

$$\frac{u_i^* - u_i^n}{\Delta t_{s+1}} = -\frac{\partial \Pi^s}{\partial x_i} + B_s + A_s + D_s, \tag{2.16}$$

$$\frac{u_i^{s+1} - u_i^*}{\Delta t_{s+1}} = -\frac{\partial \Pi^*}{\partial x_i}, \tag{2.17}$$

Equation 2.16 is used to express the prediction velocity u_i^* in known terms, which can then be substituted in Eq. 2.17. Subsequently, Eq. 2.17 is solved by taking the divergence of the equation and substituting the continuity equation (Eq. 2.9), which eliminates the term containing u_i^{s+1}, and reduces the equation to a Poisson equation for Π:

$$\frac{\partial}{\partial x_i}\left(\frac{u_i^*}{\Delta t_{s+1}}\right) = \frac{\partial^2 \Pi^*}{\partial x_i^2}, \tag{2.18}$$

which is solved for Π^* using a direct Poisson equation solver (contained in the 'FISHPACK' library) based on discrete Fourier transforms in the spanwise direction (Bailey, 1993) and cyclic reduction in the remaining directions (Sweet, 1974). As a result, all terms in Eq. 2.15 are known and the velocity field can be integrated in time using Eq. 2.14. In addition, Π is updated by $\Pi^{s+1} = \Pi^s + \Pi^*$.

2.3.3 *Stability*

The explicit time integration scheme in Eq. 2.14 results in a solution that is stable in time when two stability criteria are met. Firstly, the Courant-Friedrichs-Lewy (CFL) criterion should be satisfied;

$$\Delta t\left(\frac{u}{\Delta x} + \frac{v}{\Delta y} + \frac{w}{\Delta z}\right) \leqslant C_{\max}, \tag{2.19}$$

where $C_{\max}$ is the maximum Courant number, which is 1.5 for the second-order central differencing discretization scheme and 1.1 for the κ scheme. In addition, the diffusion number

$$\frac{\left(\alpha + \alpha_{sgs}\right)\Delta t}{\left(\Delta x^2 + \Delta y^2 + \Delta z^2\right)} \tag{2.20}$$

should be below a critical value, which was estimated to be 0.4. Note that this criterion also holds for the diffusion of momentum, $\nu + \nu_{sgs}$. Concluding, the maximum timestep used for the simulations is derived from these two criteria.

2.4 BOUNDARY CONDITIONS

2.4.1 *Domain Boundary Conditions*

The equations can be solved if proper boundary conditions are applied. For each simulation presented in this thesis the boundary conditions are given in the concerned chapter. In general, for all variables periodic boundary conditions are used in the spanwise direction (y coordinate). In case of 'double-periodic' simulations periodicity is also assumed in the streamwise direction (x coordinate) and the flow is driven by a constant pressure gradient that is applied to all grid cells. In case of

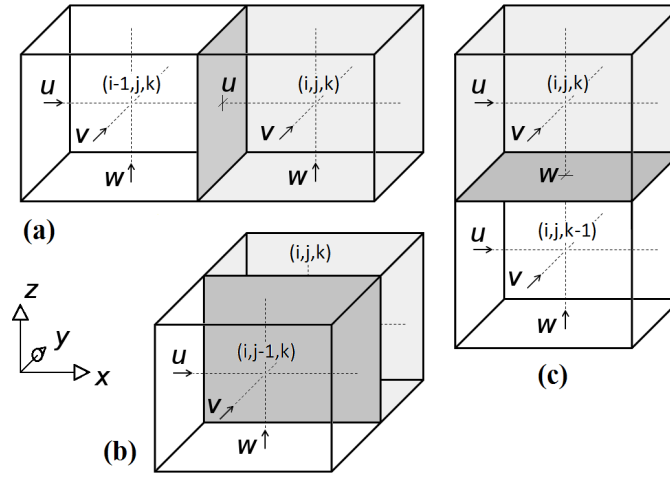

Figure 2.2: Three types of walls (indicated by dark grey planes) shown for cell (i, j, k) (indicated in light grey); a wall in the y-z plane (a), a wall in the x-z plane (b), and a wall in the x-y plane (c).

'inflow-outflow' simulations, a convective outflow boundary condition is used at the outlet plane;

$$\frac{\partial \psi}{\partial t} + U\frac{\partial \psi}{\partial x} = 0, \tag{2.21}$$

where U is the bulk velocity. In addition, at the inlet plane a turbulent boundary layer is imposed, which is generated in a separate simulation. Effectively, the flow is driven by a constant mass flux. The method to generate this inflow boundary layer is discussed in Sect. 2.4.3. Furthermore, at all walls no-slip boundary conditions are used, and for c^* zero-flux boundary conditions are applied. For θ either zero-flux or isothermal boundary conditions are used, which is discussed for each case separately.

2.4.2 *Immersed Boundary Method*

The model uses an immersed boundary method (IBM) in order to place obstacles in the rectangular domain. The IBM employed here is the method by Pourquie et al. (2009), such that the obstacle walls coincide with cell faces. This implies that only rectangular obstacles can be considered. However, the advantage of this method is that boundary conditions can be imposed exactly, which makes the method very suitable when accurate solutions are required for flow over rectangular obstacles.

Figure 2.2 shows the three types of walls that can be present in a grid cell. The IBM involves locally adding an extra force term to the momentum or transport equations such that the boundary condition is satisfied at that location. For example, if $w = 0$ is required at a cell face where w is evaluated, the force term is chosen such that the

prediction velocity w^* in Eq. 2.16 becomes zero. Additionally, velocity components adjacent and parallel to the wall should experience the wall shear stress. This is achieved by replacing the shear stress computed without the wall present with the appropriate shear stress associated with a wall. For example, the diffusion part in the equation for conservation of momentum in the x-direction (D_s term in Eq. 2.16) contains the term

$$\frac{\partial}{\partial z}\left[\left(\nu+\nu_{sgs}\right)\left(\frac{\partial u}{\partial z}+\frac{\partial w}{\partial x}\right)\right] \tag{2.22}$$

When evaluated around $u^{i,j,k}$, where the superscript indicates the cell indices, the discretized form becomes:

$$\begin{aligned}\frac{1}{\Delta z}\Bigg[&\left(\nu+\nu_{sgs}^{k+}\right)\left(\frac{u^{i,j,k+1}-u^{i,j,k}}{\Delta z}+\frac{w^{i,j,k+1}-w^{i-1,j,k+1}}{\Delta x}\right)\\&-\left(\nu+\nu_{sgs}^{k-}\right)\left(\frac{u^{i,j,k}-u^{i,j,k-1}}{\Delta z}+\frac{w^{i,j,k}-w^{i-1,j,k}}{\Delta x}\right)\Bigg],\end{aligned} \tag{2.23}$$

where an equidistant grid with cell sizes Δx and Δz is assumed for simplicity and the superscripts $k+$ and $k-$ indicate that the subgrid viscosity is interpolated to the upper and lower side of the cell around $u^{i,j,k}$, respectively. In case a wall is present in the x-y plane, as shown in Fig. 2.2c, the IBM replaces the stress the on $k-$ side of the cell (computed in Eq. 2.23);

$$\left(\nu+\nu_{sgs}^{k-}\right)\left(\frac{u^{i,j,k}-u^{i,j,k-1}}{\Delta z}+\frac{w^{i,j,k}-w^{i-1,j,k}}{\Delta x}\right), \tag{2.24}$$

with the local wall shear stress

$$\nu\left.\frac{\partial u}{\partial z}\right|_{\text{wall}}\approx 2\nu\frac{u^{i,j,k}}{\Delta z}, \tag{2.25}$$

where in both cases the stress is divided by ρ because the momentum conservation equation (Eq. 2.10) has been divided by ρ.

Similar steps are taken to apply the boundary conditions for θ and c^*. Note that the pressure correction can cause $u_i \neq 0$ at the immersed boundaries. However, such 'penetration velocities' are negligible as long as the pressure correction only involves the subtraction of $\partial\Pi^*/\partial x_i$ and not the full pressure-gradient term $\partial\Pi^{s+1}/\partial x_i$. In the simulations discussed in this thesis the maximum penetration velocities were in the order of $10^{-4}U$. More details about the IBM can be found in Pourquie et al. (2009).

2.4.3 *Generation of Turbulent Inflow Boundary Layers*

For the inflow-outflow simulations the instantaneous velocity at the inlet plane is generated in a separate 'driver' simulation by employing the method proposed by

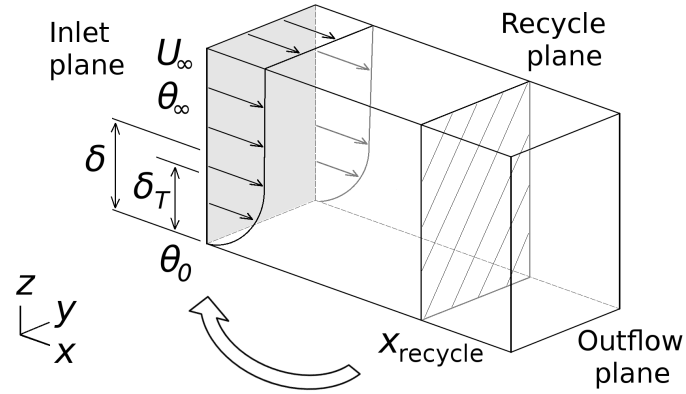

Figure 2.3: Recycling method used to generate inflow turbulent boundary layers. The mean velocity field and the velocity fluctuations at the recycle plane are rescaled using a method similar to Lund et al. (1998). The mean temperature and the temperature fluctuations at the recycle plane are rescaled using a method similar to Kong et al. (2000).

Lund et al. (1998). Both the mean velocity and the velocity fluctuations at a recycle plane are used to generate the velocity field at the inlet plane. The procedure is schematically visualized in Fig. 2.3. The underlying assumption of this method is that the flow is self-preserving, such that these the inlet plane and the recycle plane can be related to each other by using the *law of the wall* for the inner region and the *velocity-defect law* for the outer region;

$$u^{\text{inner}} = u_\tau\,(x)\, f_1\left(z^+\right) \qquad \text{'law of the wall',} \tag{2.26}$$

$$U_\infty - u^{\text{outer}} = u_\tau\,(x)\, f_2\,(z/\delta) \qquad \text{'velocity-defect law',} \tag{2.27}$$

where $z^+ = zu_\tau/\nu$ is the vertical coordinate scaled with viscous units, U_∞ is the freestream velocity, δ is the boundary layer height, and f_1 and f_2 are universal functions. The rescaling of the velocity components from the recycle plane to the inlet plane is done separately for both regions. In addition, the inlet velocity profile is created by forming a weighted average of both results of which the contributions are equal at $z = 0.2\delta$. This type of simulation can be regarded as semi-periodic, because the regular convective outflow boundary condition (Eq. 2.21) is used at the outflow plane, while there is a one-way coupling between the recycle plane and the inlet plane. The method allows the user to define two input parameters, U_∞ and δ. After taking the necessary steps to let the flow develop into a steady state, a plane perpendicular to the flow can be saved in time and subsequently used as turbulent inflow in another simulation.

The implementation in the current LES model differs from the original method by Lund et al. (1998) on two counts. Firstly, to avoid instabilities, above 1.2δ the fluctu-

ations are damped using the smooth Heaviside function as described by Bohr (2005), which results in zero rescaling of the fluctuations above 1.3δ. Secondly, a mass-flux correction is applied because the rescaling procedure and the associated interpolation can cause the mass flux at the inlet to slightly change between time steps. This results in pressure pulses through the domain (Sillero et al., 2013). Although preliminary simulations showed that the mass-flux variations were very small (with the maximum of order 0.01%), they did affect pressure statistics. Therefore, when the mean variables are fully converged, this very small mass-flux correction is applied at each time step.

The inlet temperature field is generated in a similar vein as the velocity field by using the method developed by Kong et al. (2000). However, in contrast to their simulations the buoyancy force is taken into account in the driver simulations in order to generate stably stratified turbulent boundary layers. The level of thermal stratification is set by fixing the ground temperature, θ_0, the free stream temperature, θ_∞, and the thermal boundary layer height, δ_T. For stable boundary layers this is a delicate procedure because re-laminarization can occur while the mean variables have not yet converged, which causes instabilities. The stable boundary layers discussed in this thesis were generated by first assuming the temperature to be passive until the mean variables were converged. Next, the buoyancy force was taken into account, while the level of stratification was increased slowly. Finally, to prevent the development of a strong inversion the local gradient Richardson number,

$$\mathrm{Ri}_{\mathrm{grad}} = \frac{g}{\theta_0}\frac{\partial\overline{\theta}}{\partial z}\Bigg/ 2S_{ij}S_{ij}\,, \tag{2.28}$$

is kept below the critical value ($\mathrm{Ri}_{\mathrm{grad}}^{\mathrm{crit}} \approx 0.25$) inside the boundary layer. This is achieved by setting δ_T slightly smaller than δ at the inlet: δ_T was fixed at 0.95δ at the inlet.

The universal functions f_1 and f_2 that describe the mean velocity profile in Eq. 2.26 and Eq. 2.27 are functions of z^+ and z/δ, respectively. However, for non-neutral conditions they are also a function of z/L, where $L = -u_\tau^3\theta_0/(\kappa g\overline{w'\theta'})$ is the Obukhov length scale (Obukhov, 1971). In this expression $\overline{w'\theta'}$ is assumed to be constant with height in the surface layer. It follows from the so-called 'Monin-Obukhov similarity theory' that scaling the vertical coordinate with L results in similar dimensionless velocity profiles in the surface layer (Monin and Obukhov, 1954). In the recycling method by Lund et al. (1998) the functions f_1 and f_2 are not prescribed, but it is merely assumed that they hold at both the inlet and the recycle station. The rescaling procedure requires the vertical coordinate to be scaled in either inner or outer coordinates. However, for stable conditions at a certain height, L becomes the relevant length scale, such that a scaling with L might be more suitable. Nevertheless, in the stable boundary layers considered in this thesis L was in the order of δ, so that the use of Eq. 2.26 and Eq. 2.27 was sufficient to generate boundary layers that approximate Monin-Obukhov scaling, as will be shown in Chapter 3.

3

THE EFFECTS OF A FENCE ON A RURAL BOUNDARY LAYER[1]

3.1 INTRODUCTION

Predicting the pollutant dispersion behaviour in urban areas requires a good representation of the flow in these regions. However, modelling the local flow field in urban areas is a challenging task because there are several factors that control it, e.g. the obstacle geometry, the character of the approaching turbulent boundary layer (TBL), as well as temperature differences. The review article by Barlow (2014) gives a clear overview of our current understanding of the urban boundary layer (UBL) showing that buoyancy effects in the roughness sub-layer are still poorly understood. Tominaga and Stathopoulos (2013) review the current modelling techniques for pollutant dispersion in the UBL; most pollutant dispersion studies do take into account obstacle geometry, but the correct treatment of inflow turbulence and thermal stratification is just as important for reliable results. Still, in order to simplify such flow and pollutant dispersion problems two practical approaches seem natural:

1. Neglect the presence of obstacles.
2. Neglect the effect of thermal stratification.

The first approach is plausible when the location of interest is at a large distance from obstacles. The latter approach can be justified by assuming that the flow becomes neutrally buoyant due to enhanced mixing by turbulence induced by the obstacle geometry. The objective of the current study is to investigate if and when these simplifications can be be made. Use is made of large-eddy simulations (LES) to simulate the flow and dispersion around a single prismatic obstacle. Realistic turbulent equilibrium inflow TBLs at friction Reynolds number, $\mathrm{Re}_\tau = u_\tau \delta / \nu$, of 1950 are generated to investigate how these TBLs respond to the perturbation by the obstacle.

3.1.1 *Case of Interest*

The obstacle studied here is a two-dimensional fence characterized by a small b / h ratio and an infinite l / h ratio, where b is the obstacle width, h the obstacle height,

1 This chapter is slightly adapted from Tomas, J. M., Pourquie, M. J. B. M., and Jonker, H. J. J. (2015c). The influence of an obstacle on flow and pollutant dispersion in neutral and stable boundary layers. *Atmos. Environ.*, 113:236–246

and l the obstacle length. Spanwise line sources of passive tracers are located in its vicinity. This set-up resembles in idealized form the case of an undisturbed (low roughness) TBL approaching a noise barrier located next to a highway. The simple geometry of a noise barrier is of interest because it is the first obstacle that will influence the dispersion of pollutant emitted by traffic along a highway. Besides that, it is one of the most elementary ways to perturb a boundary layer, which could give insight in how perturbations of the TBL develop. Due to its two-dimensional geometry the flow is statistically homogeneous in the spanwise direction, which allows for periodic boundary conditions to be used.

Several wind-tunnel studies have been reported on neutral turbulent flow over two-dimensional obstacles. Counihan et al. (1974) measured the flow behind a riblet in a TBL that was six times higher than the obstacle. They considered the difference with the undisturbed flow: $\Delta\overline{u} = \overline{u}_{\text{obstacle}} - \overline{u}_{\text{flat}}$, which can be negative (deficit) or positive (excess). In addition, they proposed a model for the velocity and turbulence deficit based on self-similarity of the wake. Castro (1979) compared this model to his experimental results, which showed reasonable agreement for the velocity and turbulence deficit up to 30 obstacle heights downstream. However, the model is incapable of predicting the flow further downstream. Schofield and Logan (1990) collected data from multiple experiments on high Reynolds number shear flows distorted by an obstacle smaller than the TBL height. They confirm the conclusion of Castro (1979) that the inner region adjusts quicker to the distortion by the obstacle than the outer region.

Experimental data on flow over surface-mounted obstacles in stably stratified flows are sparse. Kothari et al. (1986) performed wind-tunnel measurements on three-dimensional surface obstacles in a TBL with weak thermal stratification. Their results show a temperature excess up to $60h$ downstream of the obstacle, while the velocity deficit disappears after $7.5h - 10h$. In addition, they developed a model for the temperature wake behind three-dimensional obstacles in weakly stratified TBLs. Ogawa and Diosey (1980) did wind-tunnel experiments on a two-dimensional fence in stable and convective TBLs. The measurements were only done up to $13.5h$ downstream of the fence, because the interest was in the recirculation length.

Several numerical simulations of flow past a two-dimensional obstacle under neutral conditions have been reported. Orellano and Wengle (2000) performed LES and direct numerical simulation (DNS) of a fence in perpendicular approaching flow. Kaltenbach and Janke (2000) and di Mare and Jones (2003) investigated the fence geometry for several wind angles with LES. Abdalla et al. (2009) compared the flow over a riblet ($b/h = 1$) and the flow over a forward-facing step by means of LES. All of these numerical investigations considered approaching boundary layers with a height smaller than the obstacle, which does not resemble atmospheric conditions. Furthermore, the effects of thermal stratification are not accounted for. Only Trifonopoulos and Bergeles (1992) reported results for a two-dimensional obstacle under stable conditions using a model based on the Reynolds-averaged Navier-Stokes (RANS) equations. They showed reasonable agreement with experimental results from Ogawa and Diosey (1980). However, results were only given up to $10h$ downstream of the obstacle.

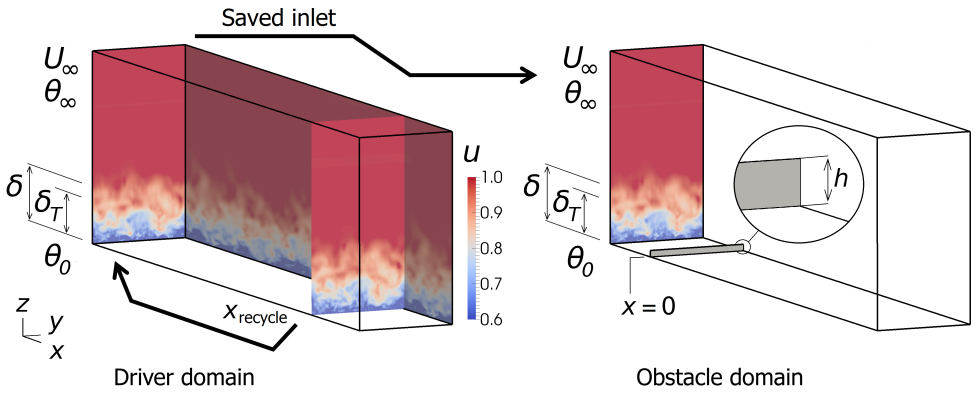

Figure 3.1: Domains of driver simulations and obstacle simulations. Freestream and ground values are fixed as well as velocity- and thermal boundary-layer height. Inlet data from driver simulations are used in all simulations.

Taking into account this paucity in available data the scope of the current study is:

1. A single two-dimensional fence subject to an approaching equilibrium TBL much larger than the fence.
2. A domain that extends up to $100h$ downstream of the fence to investigate both the near wake and the wake development inside the TBL.
3. Three levels of stable stratification together with the neutral case.
4. Spanwise line sources of passive tracers in the vicinity of the fence.

The paper is set up as follows: In Sect. 3.2 the numerical method is explained, after which in Sect. 3.3 the details on the flow configuration, computational mesh, and boundary conditions are given. The results for the inflow TBLs are discussed in Sect. 3.4. Subsequently, the results for the obstacle and flat cases are discussed in Sect. 3.5. Finally, conclusions are given in Sect. 3.6.

3.2 NUMERICAL METHOD

The cases were simulated by means of LES. Firstly, TBLs were generated in separate 'driver' simulations using a recycling method. The inlet plane was saved for each time step and subsequently used as inlet condition in the corresponding pollutant line source simulations with and without the obstacle present. We will refer to those simulations by 'obstacle' and 'flat', respectively. Fig. 3.1 visualizes the procedure.

3.2.1 *Governing Equations and Numerical Method*

The filtered Navier-Stokes equations in the Boussinesq approximation are:

$$\frac{\partial \widetilde{u}_i}{\partial x_i} = 0, \tag{3.1}$$

$$\frac{\partial \widetilde{u}_i}{\partial t} = -\frac{\partial}{\partial x_j}\left(\widetilde{u}_i \widetilde{u}_j\right) - \frac{\partial}{\partial x_i}\left(\frac{\widetilde{p} + \tau_{kk}/3}{\rho_0}\right) + \frac{g}{\theta_0}\widetilde{\theta}\delta_{i3} + \nu\frac{\partial^2 \widetilde{u}_i}{\partial x_j^2} + \frac{\partial}{\partial x_j}\left(2\nu_{sgs}\widetilde{S}_{ij}\right), \tag{3.2}$$

$$\frac{\partial \widetilde{\phi}}{\partial t} = -\frac{\partial}{\partial x_j}\left(\widetilde{\phi}\widetilde{u}_j\right) + \frac{\nu}{\mathrm{Pr}}\frac{\partial^2 \widetilde{\phi}}{\partial x_j^2} + \frac{\partial}{\partial x_j}\left(\frac{\nu_{sgs}}{\mathrm{Pr}_{sgs}}\frac{\partial \widetilde{\phi}}{\partial x_j}\right) + \mathcal{S}, \tag{3.3}$$

where $\widetilde{(..)}$ denotes filtered quantities, $\left(\widetilde{p} + \tau_{kk}/3\right)/\rho_0$ is the modified pressure, τ_{kk} is the trace of subgrid-scale stress tensor, g is the gravitational acceleration, ν is the fluid kinematic viscosity, ν_{sgs} is the subgrid-scale viscosity, Pr is the Prandtl number, Pr_{sgs} is the subgrid-scale Prandtl number, $\widetilde{S}_{ij} = \frac{1}{2}\left(\partial\widetilde{u}_i/\partial x_j + \partial\widetilde{u}_j/\partial x_i\right)$ is the rate of strain tensor and $\mathcal{S}$ is a source term. Equation 3.3 describes the transport equation for all scalar quantities ϕ, which are the temperature θ and pollutant concentration C. From here on the $\widetilde{(..)}$ symbol will be omitted for clarity. Furthermore, the $\overline{(..)}$ symbol resembles time- and spanwise averaging.

The code developed for this study is based on DALES (Heus et al., 2010). DALES has been validated and used extensively for atmospheric research in the Netherlands. It has been part of several intercomparison studies (Heus et al. (2010) and references therein). The main modifications are the addition of an immersed boundary method (Pourquie et al., 2009), the implementation of inflow/outflow boundary conditions and the application of the eddy-viscosity subgrid model of Vreman (2004). This model has the advantage over the standard Smagorinsky-Lilly model (Smagorinsky, 1963; Lilly, 1962) that no wall-damping is required to reduce the subgrid-scale energy near walls. The equations of motion are solved using second-order central differencing for the spatial derivatives and an explicit third-order Runge-Kutta method for time integration. For the scalar concentration field the second-order central κ scheme is used to ensure positivity. The simulations are wall-resolved, so no use is made of wall-functions. Pr_{sgs} was set to 0.9, equal to the turbulent Prandtl number found in the major part of the TBL in DNS studies by Jonker et al. (2013). The subgrid-scale Schmidt number was set to 0.9 as well. The code has been applied before to simulate turbulent flow over a surface-mounted fence, showing excellent agreement with experimental data (Tomas et al., 2015a).

3.2.2 *Generation of Turbulent Inflow*

The instantaneous velocity at the inlet plane of the driver simulations is generated using a recycling method similar to the method proposed by Lund et al. (1998). Both

the mean velocity profile and the velocity fluctuations at a recycle plane (8.24δ distant from the inlet) are rescaled according to the law of the wall for the inner region and the velocity defect law for the outer region. The input parameters of the method are the freestream velocity, U_∞, and the inlet TBL height, δ. There are two differences compared to the original method by Lund et al. (1998). Firstly, to avoid instabilities, above 1.2δ the fluctuations are damped using the smooth Heaviside function as described by Bohr (2005), which results in zero rescaling of the fluctuations above 1.3δ. Secondly, a mass-flux correction is applied because the rescaling procedure and the associated interpolation can cause the mass flux at the inlet to slightly change between time steps. This results in pressure pulses through the domain Sillero et al. (2013). Although the mass-flux variations in our simulations were very small (maximum of order 0.01%), we did see effects in the pressure statistics. Therefore, when the mean variables were fully converged this very small mass-flux correction was applied each time step.

The inlet temperature field is generated in a similar vein as the velocity field by using the method developed by Kong et al. (2000). However, in contrast to their simulations the buoyancy force was taken into account in the driver simulations in order to generate stably stratified TBLs. The level of thermal stratification is set by fixing the ground temperature, θ_0, the freestream temperature, θ_∞, and the thermal boundary-layer height, δ_T. For stable TBLs this is a delicate procedure because relaminarization can occur while the mean variables have not yet converged, which causes instabilities. Our results were generated by first assuming the temperature to be passive until the mean variables were converged. Next, the buoyancy force was taken into account while the level of stratification was increased slowly. Finally, to prevent the development of a strong inversion the local gradient Richardson number,

$$\mathrm{Ri}_{\mathrm{grad}} = \frac{g}{\theta_0}\frac{\partial\overline{\theta}}{\partial z}\Bigg/ 2S_{ij}S_{ij}\,, \tag{3.4}$$

is kept below the critical value ($\mathrm{Ri}_{\mathrm{grad}}^{\mathrm{crit}} \approx 0.25$) inside the boundary layer. This is achieved by setting δ_T slightly smaller than δ at the inlet: δ_T was fixed at 0.95δ at the inlet.

3.3 FLOW CONFIGURATION, MESH, AND BOUNDARY CONDITIONS

3.3.1 *Characteristics of the Flow*

To approximate the flow over an obstacle in the atmosphere the following criteria were used to specify the properties of the flow:

- **The Reynolds number:** Experimental studies have shown that the flow over a fence becomes independent of the Reynolds number if $\mathrm{Re} = U_\infty h/\nu$ is above 4000 to 5000. (Huppertz and Fernholz, 2002; Castro, 1979). The results presented here are based on a minimum Reynolds number of 5000.

Table 3.1: Domain dimensions and grid for simulated cases; Δx^+, Δy^+, and Δz^+ are based on u_τ at the inlet.

Simulation	Dim.	L_i	N_i	max. Δx_i^+	min. Δx_i^+	max. expans. ratio
Driver	x	10δ	256	77	77	-
	y	1.57δ	160	19	19	-
	z	3δ	80	196	3.9	1.07
Flat	x	$112.5h$ (11.25δ)	288	77	77	-
	y	$15.7h$ (1.57δ)	160	19	19	-
	z	$30h$ (3δ)	80	196	3.9	1.07
Obstacle	x	$113h$ (11.3δ)	656	90	6.2	1.05
	y	$15.7h$ (1.57δ)	160	19	19	-
	z	$30h$ (3δ)	128	196	3.2	1.07

- **Obstacle height in inner scaling:** Because the Reynolds number is finite a viscous sublayer forms near walls for which the characteristic velocity scale is $u_\tau = (\nu \partial \overline{u}/\partial z)^{1/2}_{\text{wall}}$ and the characteristic length scale is ν/u_τ (for smooth walls). The thickness of the viscous sublayer was approximately kept constant for all levels of stability. In addition, the top of the obstacle was in the logarithmic region of the velocity profile in case of neutral stratification.
- **Obstacle height in outer scaling:** The atmospheric boundary-layer height is in the order of one kilometer in neutral conditions. For stably stratified cases it can be in the order of 100 meters. However, in the current study we are only interested in the development in the region close to the ground. Therefore, the TBL height at the inlet of the simulations was kept constant at $10h$, which, as will be shown in Sect. 3.5, proved to be high enough for the wake not to reach the top of the boundary layer at $100h$ downstream.

After exploration of boundary-layer data we found that these criteria are met when $\mathrm{Re}_\tau = u_\tau \delta/\nu \gtrsim 1900$ at the location of the fence. Therefore, at the inlet of all simulations Re_τ was kept constant at approximately 1950. In addition to the neutral case three stably stratified TBLs were considered, for which the bulk Richardson number,

$$\mathrm{Ri} = \frac{(g/\theta_0)\,(\theta_\infty - \theta_0)\,\delta}{U_\infty^2}, \tag{3.5}$$

was 0.049, 0.098 and 0.147, respectively.

3.3.2 *Domain and Grid*

The domains for all simulations are $1.57\delta = 15.7h$ wide and 3δ high in order to capture also the largest eddies in the TBL. The length of the domain is 10δ, 11.25δ, or 11.3δ for the driver, flat, and obstacle simulations, respectively. The flow is well resolved, since the average subgrid stress, $\overline{-2\nu_{sgs}S_{13}}$, did not exceed 6% of the total Reynolds stress. Table 3.1 summarizes the domains and the number of grid points that were used for each case, including the local mesh size and maximum expansion ratio of the grid.

3.3.3 *Pollutant Line Sources*

Five independent constant-flux line sources of passive scalar, indicated by concentrations C_1, C_2, C_3, C_4, and C_5, are located at locations $x_s = -5h$, $-1h$, $1h$, $10h$, and $20h$. All sources are located at $z = 0.2h$. The source terms are distributed over the surrounding cells using a Gaussian distribution with a standard deviation of $0.25h$.

3.3.4 *Boundary Conditions*

In spanwise direction periodicity was assumed for all variables. Velocity and temperature data were imposed at the inlet as described in Sect. 3.2.2. At the outlet a convective outflow boundary condition was applied for all variables. Furthermore, on the ground and fence walls no slip conditions were applied, while at the top boundary a free-slip condition was used with a constant outflow velocity of $w = U_\infty \overline{\mathrm{d}\delta_1/\mathrm{d}x}$, where $\overline{\mathrm{d}\delta_1/\mathrm{d}x}$ is the mean streamwise growth of the displacement thickness. This was done to establish a zero pressure gradient in the driver simulations. In the flat and obstacle simulations the same outflow velocity was applied as in the driver simulations. For the scalars θ and C zero-flux boundaries were assumed, except for θ at the ground, for which isothermal conditions were applied. Applying isoflux thermal conditions would be another possibility. For TBLs nearly identical results are reported for $z^+ > 20$ (Kong et al., 2000). If this also holds for the flow behind an obstacle is a question requiring future investigation.

3.3.5 *Statistics*

After the driver simulations reached a steady state the results were averaged over $1000T$, where $T = \delta/U_\infty$. For the driver and flat simulations sampling was done at intervals of $0.2T$, while a constant time step of $0.02T$ was used. The obstacle simulations used a time step of $0.0032T$ and a sampling interval of $0.032T$. The duration of these simulations was $150T$ of which the first $50T$ was not used for averaging to make sure that start-up effects were gone.

Table 3.2: Properties of the inlet TBLs created in the driver simulations; thermal BL height δ_T, displacement thickness δ_1, momentum thickness δ_2, shape factor H, and Obukhov length L.

Simulation	Case	Re_τ	Ri	δ_T/δ	δ_1/δ	δ_2/δ	H	L/δ
Driver	BL0	1916	0	-	0.163	0.120	1.36	-
	BL1	1952	0.049	0.95	0.208	0.140	1.49	1.11
	BL2	1952	0.098	0.95	0.254	0.155	1.64	0.47
	BL3	1908	0.147	0.95	0.290	0.160	1.82	0.20

3.4 DISCUSSION OF THE INFLOW BOUNDARY LAYERS

Four TBLs were generated; one neutral case and three stably stratified cases. In Table 3.2 the properties of each TBL are given for the inflow of the domain, because this is the plane that was saved in time and used as inlet for the flat and obstacle simulations. δ_1 is the displacement thickness, δ_2 is the momentum thickness, and H is the shape factor.

In Appendix A it is shown that the horizontal domain size is adequate: at $z/\delta_0 = 0.15$ at least 18 spanwise integral length scales fit the domain width and the streamwise two-point velocity correlations have decreased to zero before half of the domain length is reached. The spanwise energy spectra decrease five orders of magnitude, which indicates that a large part of the turbulence is resolved.

The mean profiles of BL0 are in good agreement with the results from DNS of a zero pressure gradient TBL at $\mathrm{Re}_\tau = 1990$ by Sillero et al. (2013), as can be seen in Fig. 3.2, where the mean velocity profiles at the inlet are shown in both outer and inner scaling. Figure 3.3 shows the root mean square (RMS) of the velocity fluctuations for BL0 also in outer and inner scaling. u_{rms} shows a slight underprediction in the outer region. In addition, near the ground u_{rms} is slightly overpredicted, while v_{rms} and w_{rms} are slightly underpredicted; a symptom of coarseness of the mesh. The mean velocity profiles for the stable TBLs show good agreement with the log-linear velocity profiles following from Monin-Obukhov similarity theory (Monin and Obukhov, 1954):

$$\frac{\overline{u}}{u_\tau} = \frac{1}{\kappa}\left[\ln z^+ + c_0\frac{z}{L}\right] + 5.0, \tag{3.6}$$

where κ is the Von Kármán constant, $L = -u_\tau^3\theta_0/(\kappa g\overline{w'\theta'})$ is the Obukhov length, and c_0 is a constant approximately equal to 5. In Fig. 3.2b it can be seen that the temperature gradient has the largest effect in the outer region of the boundary layer, because in non-neutral cases the large eddies scale with L instead of δ. The inner region appears to be unaffected by the stratification; for $z^+ < 20$ no effect is visible in the mean velocity profile. The most stable case ($\mathrm{Ri} = 0.147$) shows the largest

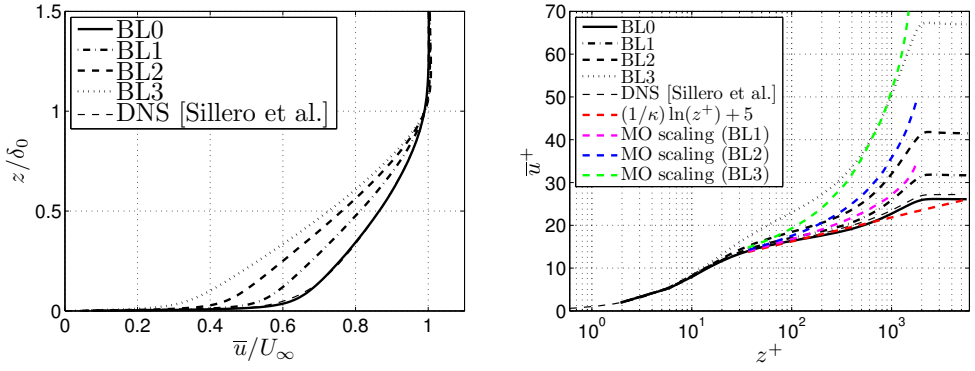

(a) (b)

Figure 3.2: Mean streamwise velocity for BL0, BL1, BL2, and BL3. For reference results from DNS at $\mathrm{Re}_\tau = 1990$ (neutral) from Sillero et al. (2013) are shown. (BL0 almost collapses with DNS data). (a) Outer scaling. (b) Inner scaling; coloured lines correspond to Monin-Obukhov theory.

deviation from the Monin-Obukhov similarity profile; the flow starts to accelerate above $z^+ = 10$. Figure 3.4 shows the mean temperature profiles at the inlet of the driver simulations for the stable cases (BL1, BL2, and BL3) in both outer and inner scaling, while Fig. 3.5 shows the corresponding profiles for the RMS of the temperature fluctuations. The mean temperature profiles show the same behaviour as the mean velocity profiles; the logarithmic profile transforms into a nearly linear profile with increasing Richardson number. Furthermore, the temperature fluctuations in the logarithmic region increase compared to the peak value in the buffer layer (at $z^+ \approx 25$). In inner scaling the peak itself also increases slightly. Finally, Fig. 3.6 shows the gradient Richardson number, $\mathrm{Ri}_{\mathrm{grad}}$ (Eq. 3.4), for the stable TBLs. Near the ground $\mathrm{Ri}_{\mathrm{grad}}$ increases with height until it reaches an approximately constant value in the outer region. Near the top of the boundary layer $\mathrm{Ri}_{\mathrm{grad}}$ increases again until the top of the boundary layer is reached, where it is not defined. In all driver simulations $\mathrm{Ri}_{\mathrm{grad}}$ stayed below the critical gradient Richardson number, $\mathrm{Ri}_{\mathrm{grad}}^{\mathrm{crit}} \approx 0.25$, inside the boundary layer, except for BL3, which reached $\mathrm{Ri}_{\mathrm{grad}} = 0.25$ at $z/\delta = 0.95$. BL3 remained turbulent, but further increasing $\Delta\theta$ did result in intermittent turbulent flow.

3.5 DISCUSSION OF THE FLAT AND OBSTACLE SIMULATIONS

Next, we considered the flow over a fence together with pollutant emissions from line sources by using the previously generated TBLs as inflow condition. The flat cases were simulated as well. Table 3.3 lists the characteristics of the flat and obstacle simulations and the corresponding inflow boundary layer that was used. Firstly, we will discuss the flow up to the recirculation zone, after which we will consider the flow

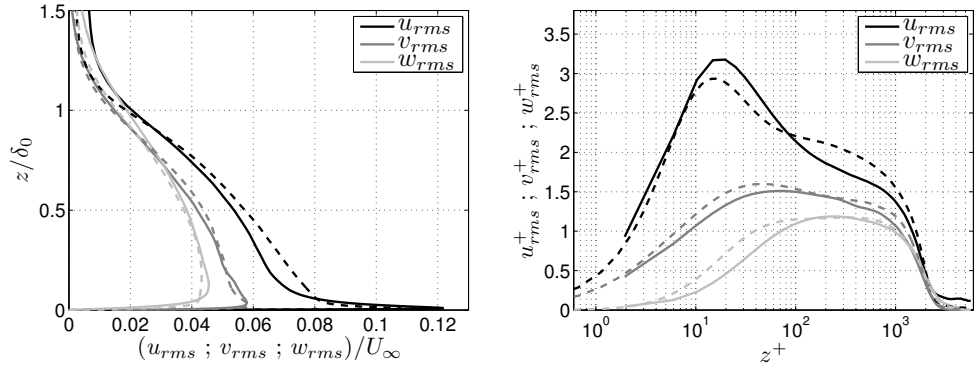

(a) (b)

Figure 3.3: RMS of the velocity fluctuations for BL0 (continuous lines). For reference results from DNS at $\mathrm{Re}_\tau = 1990$ (neutral) from Sillero et al. (2013) are shown (dashed lines). (a) Outer scaling. (b) Inner scaling.

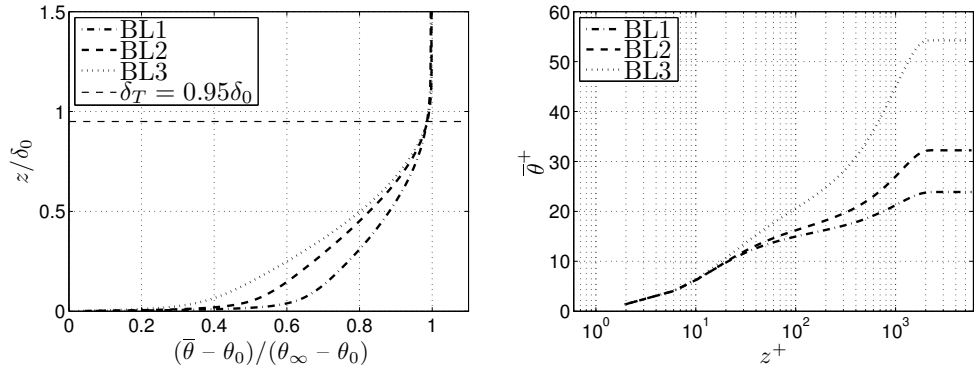

(a) (b)

Figure 3.4: Mean temperature for BL1, BL2, and BL3. (a) Outer scaling. (b) Inner scaling.

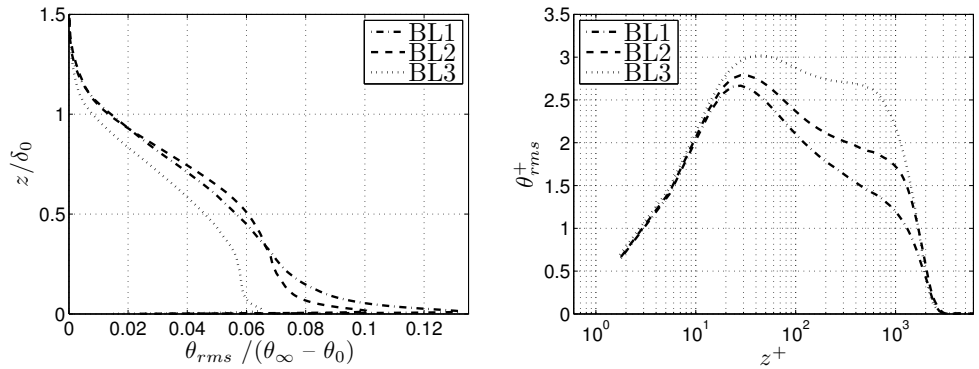

(a) (b)

Figure 3.5: RMS of the temperature fluctuations for BL1, BL2, and BL3. (a) Outer scaling. (b) Inner scaling.

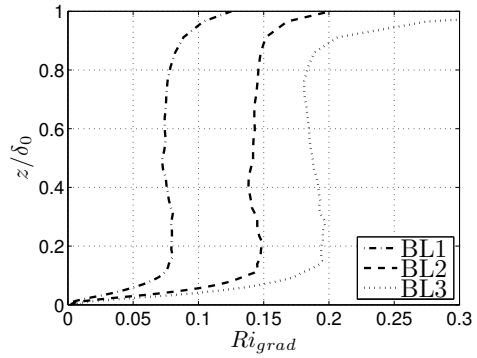

Figure 3.6: Gradient Richardson number, $\mathrm{Ri}_{\mathrm{grad}}$.

Table 3.3: A summary of the main simulations.

Simulation	Case	Inflow	Re_τ	Ri
Flat	LESN00	BL0	1916	0
	LESS00	BL1	1952	0.049
	LESS10	BL2	1952	0.098
	LESS20	BL3	1908	0.147
Obstacle	LESN01	BL0	1916	0
	LESS01	BL1	1952	0.049
	LESS11	BL2	1952	0.098
	LESS21	BL3	1908	0.147

development further downstream. Then, we try to answer the main research question by investigating the dispersion of pollutants. Finally, we will study the decay of maximum deficit/excess of velocity, temperature, Reynolds stress, and concentration to quantify up to what distance the obstacle is of influence.

3.5.1 *Near Wake*

Figure 3.7 shows the mean flow patterns in the vicinity of the fence for Ri $= 0.000$ and Ri $= 0.147$. There is an upstream recirculation zone with length of h that reaches up to $2/3$ of the fence height. The reattachment length of the downstream recirculation zone, L_R, depends only slightly on Ri. For Ri $= 0.000$, Ri $= 0.047$, Ri $= 0.098$, and Ri $= 0.147$ L_R is $10.6h$, $10.6h$, $10.4h$, and $10.1h$, respectively. It is mainly the height of the recirculation zone that is affected by stratification. The maximum height of separating streamline is $1.70h$, $1.65h$, $1.60h$, and $1.45h$, respectively.

3.5.2 *Wake Development*

Figure 3.8 shows the development of $\overline{u}$, $\overline{\theta}$, and $\mathrm{Ri}_{\mathrm{grad}}$ for the cases with and without the fence present. The results are given at downstream locations of $10h$, $30h$, $50h$, and $100h$ downstream of the fence. The variables are presented in outer scaling using the TBL height at the inlet to scale the vertical dimension.

At $x/h = 10$ the profiles of $\overline{u}$ for the obstacle cases show a region of reduced velocity (a deficit) near the ground and a region of increased velocity (an excess) above $z = 0.2\delta_0 = 2h$ compared to the flat cases. Going downstream both the deficit region and the excess region move upwards, while their maximum value decreases. Furthermore, for the stable cases the flow downstream of the fence starts to develop a velocity excess near the ground. This velocity excess is larger for higher levels of

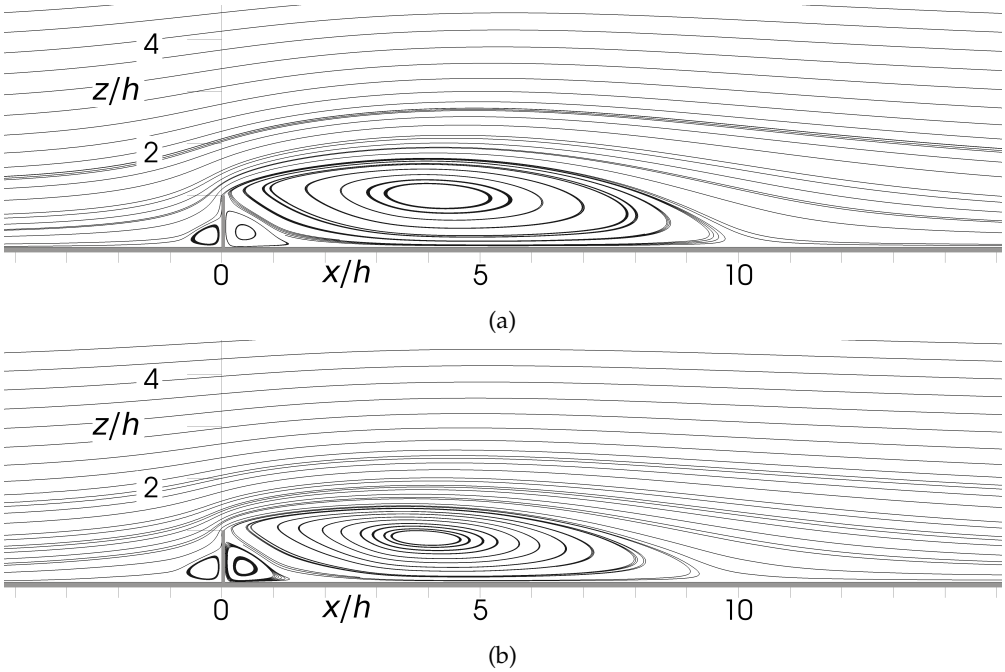

Figure 3.7: Mean streamlines for (a) LESN01 (Ri = 0) and (b) LESS21 (Ri = 0.147). The fence is located at $x = 0$.

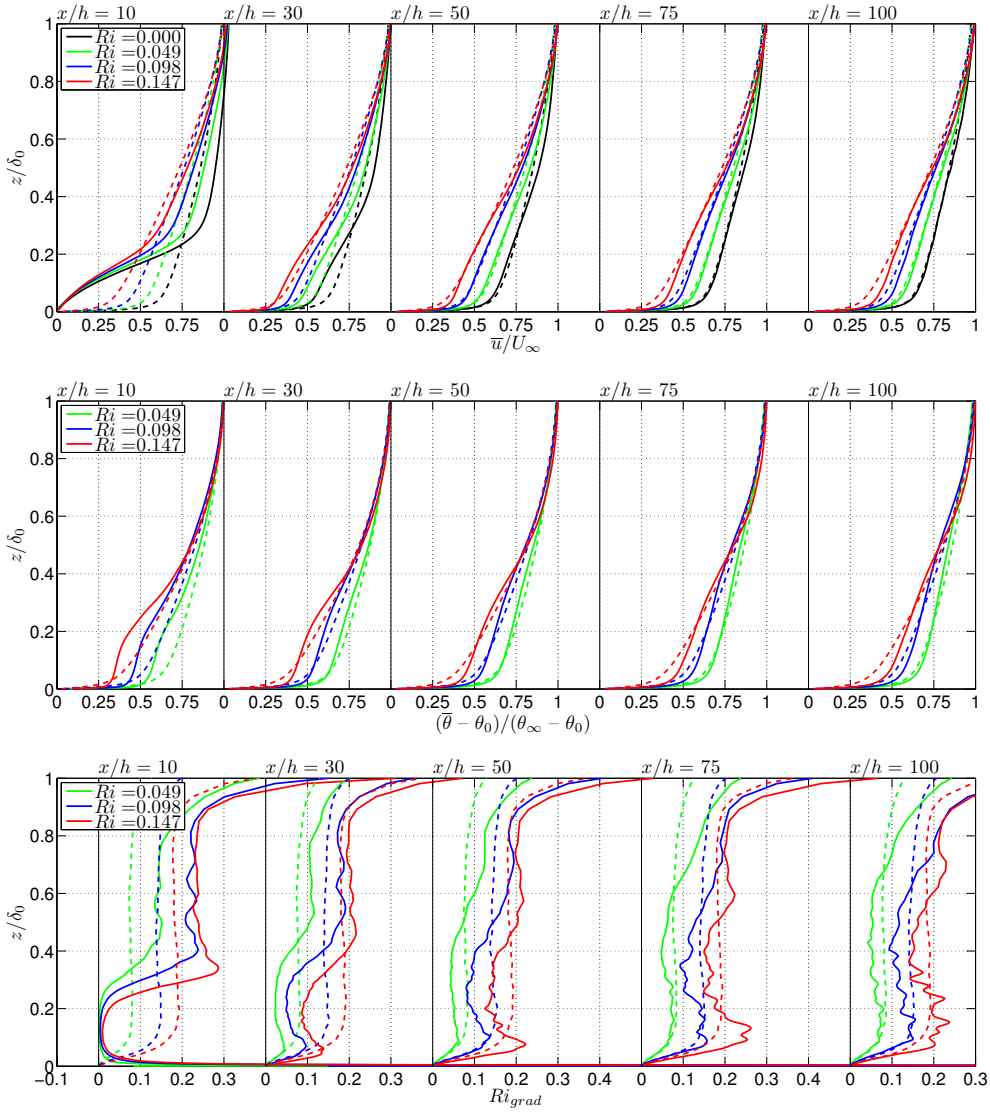

Figure 3.8: Average downstream development of $\overline{u}$ (top), $\overline{\theta}$ (middle), and $\mathrm{Ri}_{\mathrm{grad}}$ (bottom). Continuous lines: Obstacle cases. Dashed lines: Flat cases.

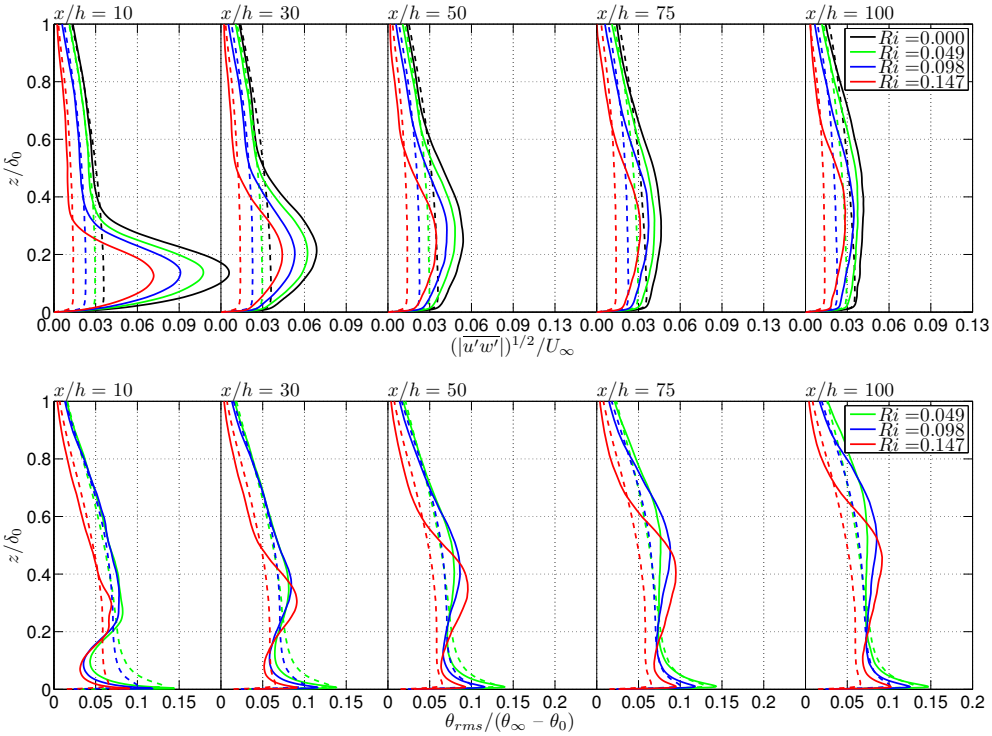

Figure 3.9: Average development of $|\overline{u'w'}|^{1/2}$ (top), and θ_{rms} (bottom). Continuous lines: Obstacle cases. Dashed lines: Flat cases.

stratification. We attribute the near-ground excess in $\overline{u}$ to enhanced mixing due to turbulence added by the presence of the fence, which results in a momentum flux from the outer flow to the flow near the ground. For the stable cases the effect becomes more apparent because in those cases there is still an excess in Reynolds stress (see Fig. 3.9) at the point where the mean velocity has recovered to its undisturbed value.

Just downstream of the fence the profiles for $\overline{\theta}$ are almost uniform up to $z = 0.2\delta_0$, because the near wake has fully mixed the flow. Further downstream the profiles become similar to the $\overline{u}$ profiles with a temperature deficit in the outer region and a temperature excess developing near the ground, which is larger for higher levels of stratification. This temperature excess is caused by the same effect that causes the near-ground acceleration.

Although the profiles of $\mathrm{Ri}_{\mathrm{grad}}$ for the obstacle simulations are rather distorted (due to limited averaging time) the effects of both the presence of the obstacle and stratification are visible. Because at $x = 10h$ up to $z = 0.2\delta_0$ the flow is fully mixed $\mathrm{Ri}_{\mathrm{grad}} = 0$. However, above that region $\mathrm{Ri}_{\mathrm{grad}}$ has increased almost by a factor two with respect to the flat case due to the increased vertical gradient in $\overline{\theta}$ between $z = 0.2\delta_0$ and $z = 0.4\delta_0$. Going downstream the deficit in $\mathrm{Ri}_{\mathrm{grad}}$ moves upwards during which it spreads and decreases in magnitude. Increasing the stratification causes the deficit in $\mathrm{Ri}_{\mathrm{grad}}$ to move upwards slower and spread slower.

Figure 3.9 shows the profiles of $|\overline{u'w'}|^{1/2}$ and θ_{rms}. For the fence cases at $x = 10h$ the root mean square (RMS). of the three velocity components (not shown) as well as $|\overline{u'w'}|^{1/2}$ have their maximum around $z = 0.15\delta_0$, while the flat cases are nearly constant. Going downstream the excess moves upwards into the outer flow. Higher levels of stratification show slower spreading in vertical direction in accordance with a slower decay of the maximum. The development of θ_{rms} shows a different behaviour. Very close to the ground there is an increase in θ_{rms}, while there is a decrease from there up to $z = 0.2\delta_0$ because the near wake is fully mixed. Above $z = 0.2\delta_0$ θ_{rms} has increased again. Further downstream the excess in the outer flow moves upwards, while the excess region near the ground remains equal in magnitude and location. Going downstream the deficit region around $z = 0.1\delta_0$ changes into an excess for the most stable case.

3.5.3 *Pollutant Dispersion*

Next, we consider the effect of both the presence of the obstacle and thermal stratification on the dispersion of pollutants. This will answer the question if and when these two factors can be neglected in order to use simplified models to predict air quality. The five independent spanwise line sources of passive scalar, indicated by concentrations C_1, C_2, C_3, C_4, and C_5, are located at locations $x_s = -5h$, $-1h$, $1h$, $10h$, and $20h$, respectively. All sources are located at $z = 0.2h$ to mimic the exhaust gases from traffic. We will diagnose the concentration at ground level because that is approximately what the population is exposed to. Moreover, for the cases stud-

ied here the ground concentrations are the maximum concentrations for the region downstream of reattachment.

Figure 3.10 shows the influence of Ri on the measured concentration at ground level at locations $10h$, $30h$, $50h$, and $75h$ downstream of each source location, x_s. Results are given for obstacle cases as well as the flat cases. The concentration has been scaled with the concentration measured in the neutral case. As expected, the concentration profiles for the flat cases collapse. For the fence simulations the profiles are also in good agreement with each other even though the source location relative to the position of the fence differs per source. Overall, ground concentrations increase with higher levels of stratification. The effect is less for the obstacle simulations because of enhanced mixing due to increased turbulence. Still, for the case at $\mathrm{Ri} = 0.147$ concentrations are 2.5 times higher than the neutral case at $75h$ downstream of the emission source, which indicates that stratification effects cannot be neglected.

The effect of the obstacle on the ground concentration is shown in Fig. 3.11, where the ratio of ground level concentration for the obstacle case over the flat case, $(\overline{C}^{\mathrm{obs.}} / \overline{C}^{\mathrm{flat}})_{\mathrm{ground}}$, is given along the downstream direction for source 1 (located at $x/h = -5$) and source 4 (located at $x/h = 10$). The result for source 2 is similar to Fig. 3.11a while sources 3 and 5 give results similar to Fig. 3.11b. In all cases the presence of the fence causes ground concentrations initially to decrease compared to the flat situation. The influence of the fence is largest for the most stratified case, for which $\overline{C}_1^{\mathrm{obs.}}$ has decreased to 28% of the flat case in the region downstream of reattachment. For the neutral case this is 50%. At $x/h = 100$ this ratio has increased to 35% (stable) and 65% (neutral). The largest reduction in ground concentration is measured for source 4. This can be explained by the fact that source 4 is located just before the point of reattachment. At this location the shear layer emanating from the top of the fence impinges on the surface which has a strong mixing effect. The least reduction is measured for sources 1 and 5, which are located at the largest distance from the recirculation zone of the fence.

3.5.4 *Decay of Maximum Deficits*

According to Schofield and Logan (1990) in the outer flow the decay of maximum deficit in mean velocity relative to its value at the reattachment location should scale with the length scales $x - x_R$ and δ, where $x - x_R$ is the distance from the reattachment location, x_R. Using data from several experiments they showed that the decay has a logarithmic dependence on the recovery distance, $x - x_R$, of the form:

$$\frac{\Delta\overline{u}}{\Delta\overline{u}_R} = -0.50 \log_{10} \frac{x - x_R}{\delta} + 0.49, \tag{3.7}$$

where $\Delta\overline{u}$ is the maximum velocity deficit and subscript R indicates the value at the reattachment location. If we determine $\Delta\overline{u}$ at each downstream location and scale our results accordingly the data does not match the profile of Eq. 3.7. However, as mentioned in Sect. 3.5.2, there is a velocity excess just above the obstacle, which is

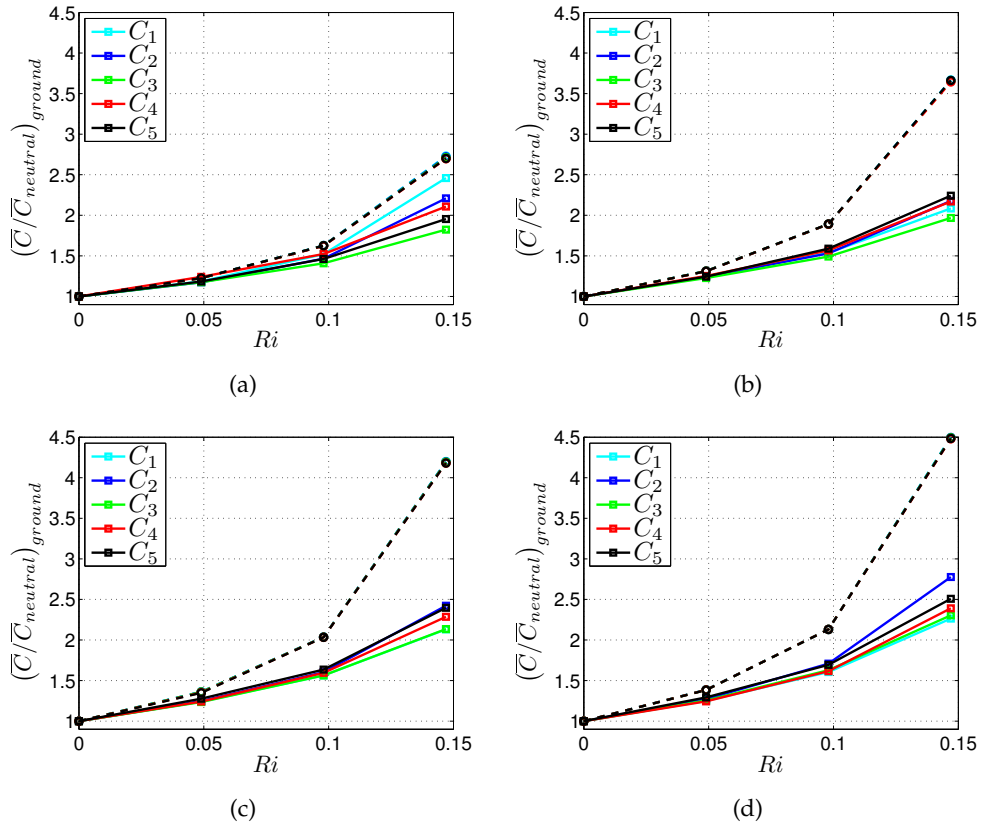

Figure 3.10: Effect of stratification on ground concentrations. (a) $(x - x_s)/h = 10$. (b) $(x - x_s)/h = 30$. (c) $(x - x_s)/h = 50$. (d) $(x - x_s)/h = 75$. Continuous lines: Obstacle cases. Dashed lines: Flat cases.

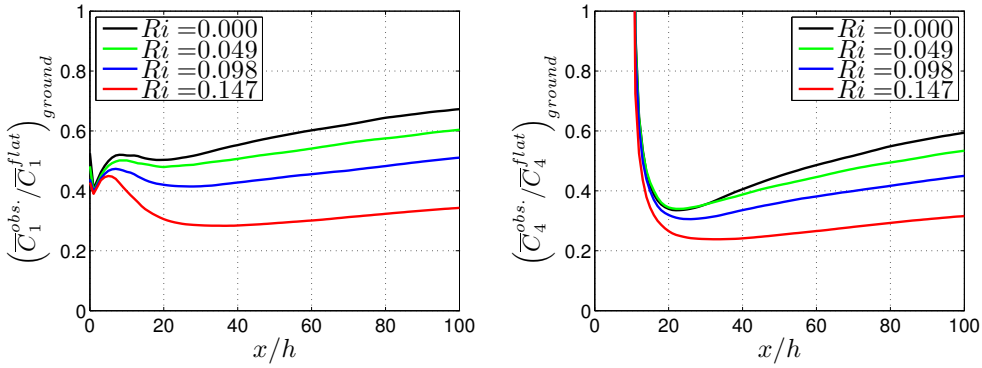

(a) (b)

Figure 3.11: Effect of obstacle on ground concentrations downstream. (a) Source 1. (b) Source 4.

not present in the experimental results on which the empirical fit of Eq. 3.7 is based. If we consider the mean velocity deficit relative to the velocity excess at the fence location, the data does collapse, as can be seen in Fig. 3.12a. The experimental results from four experiments by Counihan et al. (1974) and Castro (1979) are plotted as well. All the experimental results are based on a two-dimensional square obstacle in a rough-wall TBL where h/δ ranged from 5.9 to 14.5. Remarkably, the decay appears to be independent of the stratification.

In Figure 3.12b it is shown that the decay of the maximum deficit in mean temperature, $\Delta\overline{\theta}$, shows reasonable agreement with the profile of Eq. 3.7 (for $\Delta\overline{u}$); $\Delta\overline{\theta}$ decays similarly as $\Delta\overline{u}$ even though the profiles at the reattachment location are different as explained in Sect. 3.5.2. Just as for $\Delta\overline{u}$, stratification does not have an effect on the decay of $\Delta\overline{\theta}$. This cannot be said for the decay of maximum excess in mean Reynolds stress, $\Delta\overline{u'w'}$, which is shown in Fig. 3.13a. From about 1δ ($\approx L_R$) downstream of the reattachment point the decay shows $((x - x_R)/\delta)^{-1}$ dependence for the neutral case. For the most stable case this has changed to an exponent of $-1/2$. Similar effects are visible for the decay of maximum excess in mean contration, $\Delta\overline{C}$, shown in Fig. 3.13b, where results are given for source 3. The same conclusion can be drawn for the other line sources. This Ri dependence is in accordance with the observation that in the stratified cases the reduction in ground concentrations lasts farther downstream than in the neutral case (Figure 3.11).

3.6 CONCLUSIONS

We have shown that by using a recycling method accurate turbulent inflow TBLs for stable stratification up to $\mathrm{Ri}_{\mathrm{grad}} = 0.2$ can be generated. This enabled a detailed investigation of the response of neutral and stably stratified flows to the presence of an obstacle. The validity of two simplifications has been studied; either neglect the

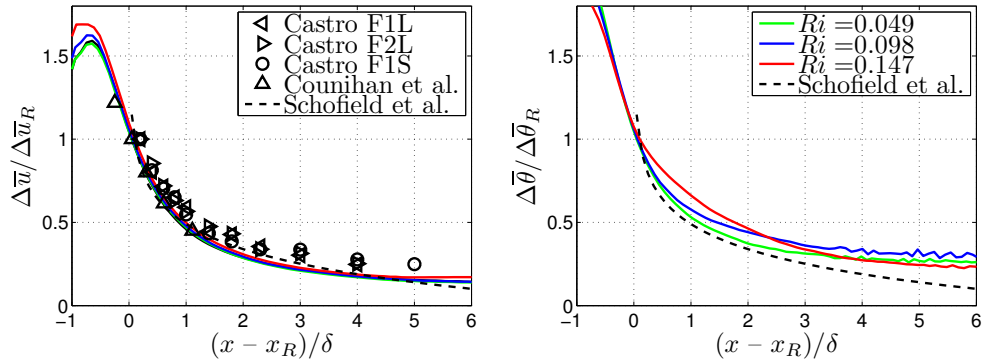

(a) (b)

Figure 3.12: Decay of maximum deficit in (a) mean velocity and (b) mean temperature downstream of reattachment. $\Delta\overline{u}$ is corrected with maximum $\Delta\overline{u}$ at fence location. Experimental data from Counihan et al. (1974) and Castro (1979) are shown.

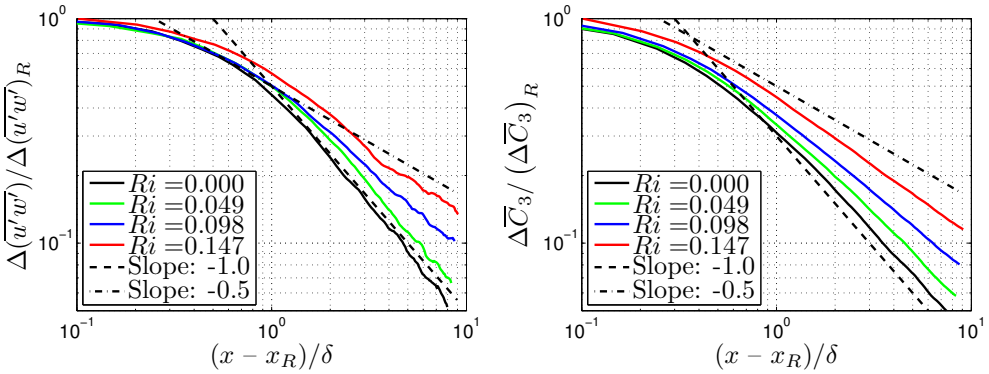

(a) (b)

Figure 3.13: Decay of (a) maximum deficit in mean Reynolds stress and (b) maximum excess in mean concentration (Source 3).

presence of the obstacle, or neglect thermal stratification effects. We conclude that for neutral cases the effect of a two-dimensional obstacle can be neglected after approximately $75h$ if $\overline{u}$ is considered. However, for stable cases the $\overline{u}$ and $\overline{\theta}$ profiles have not recovered to their undisturbed shape, even after $100h$; $\overline{u}$ and $\overline{\theta}$ are increased near the ground proportional to the level of stratification. Moreover, for all Richardson numbers turbulence levels are significantly increased for longer distances, which results in lower ground concentration due to increased pollutant dispersion.

Regarding the second simplification, i.e. to neglect thermal stratification, we can conclude that stratification is indeed reduced locally due to enhanced mixing by the obstacle. However, making the assumption that the flow in the wake of the obstacle is neutrally buoyant results in an underestimation of concentrations by a factor 2.5 at $75h$ downstream of the emission source for the case at $\mathrm{Ri} = 0.147$. We therefore conclude that both suggested simplifications are unjustified when considering a single obstacle in an undisturbed flow. Whether the same conclusion holds for multiple obstacles requires further investigation.

Furthermore, we have shown that the maximum deficit in mean velocity relative to the maximum deficit at the point of reattachment shows the same decay for all levels of stratification. If scaled with the development length $(x - x_R)/\delta$ the results collapse with data from several experiments under neutral conditions, showing a logarithmic dependence. The decay of maximum deficit in mean temperature shows similar behaviour. However, the decay of the maximum deficit in mean Reynolds stress does show a dependence on the stratification. For neutral conditions, after one TBL height behind the reattachment location the decay starts to show a -1 power-law dependence on $(x - x_R)/\delta$, while for the most stratified case the exponent reduces to $-1/2$. This means that in stratified cases the presence of an obstacle can be visible up to much larger distances than in the neutral case. If we extrapolate the measured decay of Reynolds stress excess the neutral case will reach 1% of the value at the reattachment location at $(x - x_R)/\delta \approx 47$. This is $(x - x_R)/\delta \approx 1850$ for the case at $\mathrm{Ri} = 0.147$. Moreover, the decay of maximum excess in mean concentration shows a similar dependency on Ri as the turbulent stresses. For three-dimensional obstacles qualitatively similar behaviour can be expected, but the obstacle effect will dissappear more rapidly with decreasing l/h ratio. The effect of multiple obstacles will be subject of future investigations.

Modelling pollutant dispersion near obstacles with a Gaussian plume-like model most likely fails. Computational fluid dynamics (CFD) models based on RANS equations predict complex flow fields reasonably for neutral conditions. However, around complex geometries buoyancy can have a large influence on both the flow field and the surface energy balance (Schrijvers et al., 2015). Unfortunately, RANS models handle buoyancy effects poorly. Therefore, results from such simplified models should be compared with experimental data and/or LES/DNS results in order to assess their validity.

3.7 ACKNOWLEDGEMENTS

This study was done within the STW project DisTUrbE (project no. 11989) using the computational resources of SURFsara with the funding of the Netherlands Organisation for Scientific Research (NWO), project no. SG-015.

4

RURAL-TO-URBAN TRANSITIONS: STABILITY EFFECTS[1]

4.1 INTRODUCTION

In view of the global trend of urbanization there is an increasing demand for accurate predictions of urban air quality. Therefore, predicting the dispersion behaviour of pollutants within the urban canopy is of great interest. The modelling and simulation of the urban boundary layer is usually achieved by assuming that the turbulent boundary layer has fully developed over a large urban area with uniform properties (e.g. Coceal et al. (2006); Michioka et al. (2014); Boppana et al. (2014)). However, in reality the overall character of the surface roughness changes from rural to suburban to urban regions, implying that the boundary layer has to adapt to the changing surface roughness. There are several studies that investigate such a roughness transition (Garratt, 1990). In the past these were mostly based on analytical derivations (e.g. Townsend (1966); Macdonald (2000)), but also simplified numerical models were derived (e.g. Belcher et al. (2003)). Only a few numerical studies are reported that simulate flow for an explicitly resolved roughness transition (Lee et al., 2011; Cheng and Porté-Agel, 2015).

Moreover, often the urban boundary layer is considered only for near-neutral conditions by assuming that the turbulence due to the presence of the obstacle results in a well-mixed flow with nearly uniform temperature. In the boundary layer pollutant concentrations increase significantly with increasing stability because the spreading downwind of the emission source is reduced due to lower turbulence levels. In urban environments the stable boundary layer occurs less often than does the unstable boundary layer (Wood et al., 2010). However, because of potentially decreased air quality in stable conditions it is important to determine when the 'neutral urban boundary-layer assumption' is valid. Tomas et al. (2015c) show that the turbulence added by the presence of a single two-dimensional obstacle is not enough to diminish buoyancy effects. Whether the transition of stable flow over a rural environment to a generic urban roughness consisting of multiple cubes does result in near-neutral flow is the subject of the present study. The objective is to answer the following questions:

1. How do stably stratified turbulent boundary layers respond to a rural-to-urban roughness transition?

1 This chapter is slightly adapted from Tomas, J. M., Pourquie, M. J. B. M., and Jonker, H. J. J. (2016b). Stable Stratification Effects on Flow and Pollutant Dispersion in Boundary Layers Entering a Generic Urban Environment. *Boundary-Layer Meteorol.*, 159(2):221–239

2. Are stratification effects diminished by the added turbulence due to the roughness?

3. How do the roughness transition and the stable stratification affect pollutant dispersion?

Use is made of large-eddy simulation (LES) to investigate a smooth-wall turbulent boundary layer exposed to a roughness transition consisting of an array of cubes in an in-line arrangement. Line sources of pollutant emission are located at two different vertical positions in front of the array. The case is studied for both neutral and stable conditions. The roughness Reynolds number, $h^+ = u_\tau h/\nu$, based on the friction velocity u_τ and the obstacle height h, was between 195 at the inlet and 353 (455 in stable conditions) at the end of the domain. This is in the fully rough regime (Raupach et al., 1991), and in addition, Cheng and Castro (2002b) showed that for flow over a similar array of sharp-edged obstacles the Reynolds number dependency is small.

In Sect. 4.2 the governing equations, numerical method, and the considered cases are described. In Sect. 4.3 results for a fully-developed urban boundary-layer test case are compared with experimental data to validate the LES model. Section 4.4 treats the results for flow entering a generic urban canopy, focussing on the velocity fields, turbulence kinetic energy budget, and concentration fields. Finally, in Sect. 4.5 conclusions are given.

4.2 SET-UP OF LARGE-EDDY SIMULATIONS

4.2.1 *Governing Equations and Numerical Method*

The filtered Navier-Stokes equations in the Boussinesq approximation are

$$\frac{\partial \widetilde{u}_i}{\partial x_i} = 0, \tag{4.1}$$

$$\frac{\partial \widetilde{u}_i}{\partial t} = -\frac{\partial}{\partial x_j}\left(\widetilde{u}_i\widetilde{u}_j\right) - \frac{\partial}{\partial x_i}\left(\frac{\widetilde{p} + \tau_{kk}/3}{\rho_0}\right) + \frac{g}{\theta_0}\widetilde{\theta}\delta_{i3} + \nu\frac{\partial^2 \widetilde{u}_i}{\partial x_j^2} + \frac{\partial}{\partial x_j}\left(2\nu_{sgs}\widetilde{S}_{ij}\right), \tag{4.2}$$

$$\frac{\partial \widetilde{\phi}}{\partial t} = -\frac{\partial}{\partial x_j}\left(\widetilde{\phi}\widetilde{u}_j\right) + \frac{\nu}{\mathrm{Pr}}\frac{\partial^2 \widetilde{\phi}}{\partial x_j^2} + \frac{\partial}{\partial x_j}\left(\frac{\nu_{sgs}}{\mathrm{Pr}_{sgs}}\frac{\partial \widetilde{\phi}}{\partial x_j}\right) + \mathcal{S}, \tag{4.3}$$

where $\widetilde{(..)}$ denotes filtered quantities, $\left(\widetilde{p} + \tau_{kk}/3\right)/\rho_0$ is the modified pressure, τ_{kk} is the trace of the subgrid-scale (SGS) stress tensor, g is the acceleration due to gravity, ν is the fluid kinematic viscosity, ν_{sgs} is the SGS viscosity, Pr is the Prandtl number, Pr_{sgs} is the SGS Prandtl number, $\widetilde{S}_{ij} = \frac{1}{2}\left(\partial\widetilde{u}_i/\partial x_j + \partial\widetilde{u}_j/\partial x_i\right)$ is the rate of strain tensor, and $\mathcal{S}$ is a source term. The eddy-viscosity SGS model, $\tau_{ij}/\rho_0 = \left(\widetilde{u_i u_j} - \widetilde{u}_i\widetilde{u}_j\right) =$

$-2\nu_{sgs}\widetilde{S}_{ij}$, where τ_{ij} is the SGS stress tensor, is already incorporated in Eqs. 4.2 and 4.3. Equation 4.3 describes the transport equation for all scalar quantities ϕ, which are the temperature θ and the pollutant concentration c^*. Hereafter, the $\widetilde{(..)}$ symbol is omitted for clarity; the $\overline{(..)}$ symbol represents temporal averaging.

The code developed for this study is based on the Dutch Atmospheric Large-Eddy Simulation (DALES) code (Heus et al., 2010), where the main modifications are the addition of an immersed boundary method (Pourquie et al., 2009), the implementation of inflow/outflow boundary conditions, and the application of the eddy-viscosity SGS model of Vreman (2004). This model has the advantage over the standard Smagorinsky-Lilly model (Smagorinsky, 1963; Lilly, 1962) that no wall-damping is required to reduce the SGS energy near walls. The equations of motion are solved using second-order central differencing for the spatial derivatives and an explicit third-order Runge-Kutta method for time integration. For the scalar concentration field the second-order central κ scheme is used to ensure positivity. The simulations are wall-resolved, so no use is made of wall functions. Pr was 0.71 and Pr_{sgs} was set to 0.9, equal to the turbulent Prandtl number found in the major part of the turbulent boundary layer in direct numerical simulation (DNS) studies by Jonker et al. (2013). The SGS Schmidt number was set to 0.9 as well. The code has been used previously to simulate turbulent flow over a surface-mounted fence, showing excellent agreement with experimental data (Tomas et al., 2015a,c).

4.2.2 *Cases Studied*

Here a summary is given of the simulation cases. Four types of simulations were performed:

Roughness transition (RT) simulations: In these simulations the roughness transition was simulated by considering a smooth-wall turbulent boundary layer of depth $\delta = 10h$ that approaches an array of cubes with dimensions $h \times h \times h$ in an in-line arrangement equally spaced with a pitch of $2h$, as is shown in Fig. 4.1. Emissions from two line sources of pollutant were simulated; one located at $z/h = 3$ and one located at $z/h = 0.2$. Both sources are located at $2h$ in front of the first row of cubes. The case was simulated for neutral as well as stable conditions.

Driver (D) simulations: These simulations generated the smooth-wall inflow turbulent boundary layers of $10h$ depth for the RT simulations. Inflow and outflow conditions were used in the streamwise direction. The instantaneous inlet values were generated by a recycling method described in the next section. Both neutral and stable conditions were considered, and the roughness Reynolds number, $h^+ = u_\tau h/\nu$, was 195.

Periodic roughness (PR) simulations: These simulations used the classical approach of applying periodic boundary conditions in the horizontal directions to simulate fully-developed flow. The same roughness geometry as in the RT simulations was considered on a smaller domain.

Table 4.1: Domain dimensions and grid sizes.

Sim.	L_x	L_y	L_z	N_x	N_y	N_z	$\Delta x_{\min}$	Δy	$\Delta z_{\min}$
RT	$61.47h$	$18h$	$30h$	1080	360	180	$0.050h$	$0.050h$	$0.010h$
D	$200h$	$18h$	$30h$	768	320	128	$0.260h$	$0.056h$	$0.010h$
PR	$8h$	$8h$	$10h$	160	160	144	$0.050h$	$0.050h$	$0.010h$
V	$4h$	$4h$	$10h$	64	80	112	$0.063h$	$0.050h$	$0.050h$

Validation (V) simulation: The results of this simulation are compared with the experimental results of Castro et al. (2006) considering fully-developed flow over an array of cubes. Figure 4.2 shows the geometry of the experiment. It is similar to the RT and PR simulations except that the cube arrangement is staggered. As in the PR simulation periodic boundary conditions were used in the horizontal directions. The roughness Reynolds number was 371.

4.2.3 *Domain Size and Grid*

Table 4.1 summarizes the domain size and number of grid points used in each type of simulation. The boundary layers were generated using a horizontal domain size of $L_x \times L_y = 20\delta \times 1.8\delta$, which is sufficiently large; in Tomas et al. (2015c) it was shown that a smaller horizontal domain size of $L_x \times L_y = 10\delta \times 1.57\delta$ was adequate to capture the largest flow structures in the boundary layer. The PR and V simulations used a smaller domain size than the RT simulations; decreasing the domain width did not result in differences in mean statistics.

For all simulations the grid is stretched in the vertical direction. The minimal vertical grid resolution in the V simulation was $0.05h$ at the top of the cubes and the grid expansion ratio never exceeded 1.07. All other simulations used a minimal vertical grid spacing of $0.01h$ at the top of the obstacles and the expansion ratio did not exceed 1.06 inside the boundary layer. In the horizontal directions a uniform grid is used, except for the inflow region of the RT simulations, where the grid is stretched with an expansion ratio of 1.02 to match the grid of the D simulation. For the PR and RT simulations the number of grid points covering each cube was $n_x \times n_y \times n_z = 20 \times 20 \times 48$; for the V simulation this was $n_x \times n_y \times n_z = 16 \times 20 \times 28$. Similar LES studies on cubical roughness reported good agreement with experimental data using lower resolutions; e.g. Kanda et al. (2004) used 10 cells in each cube dimension and Cheng and Porté-Agel (2015) used $n_x \times n_y \times n_z = 10 \times 10 \times 15$, which indicates that the grid used in the current study is adequate.

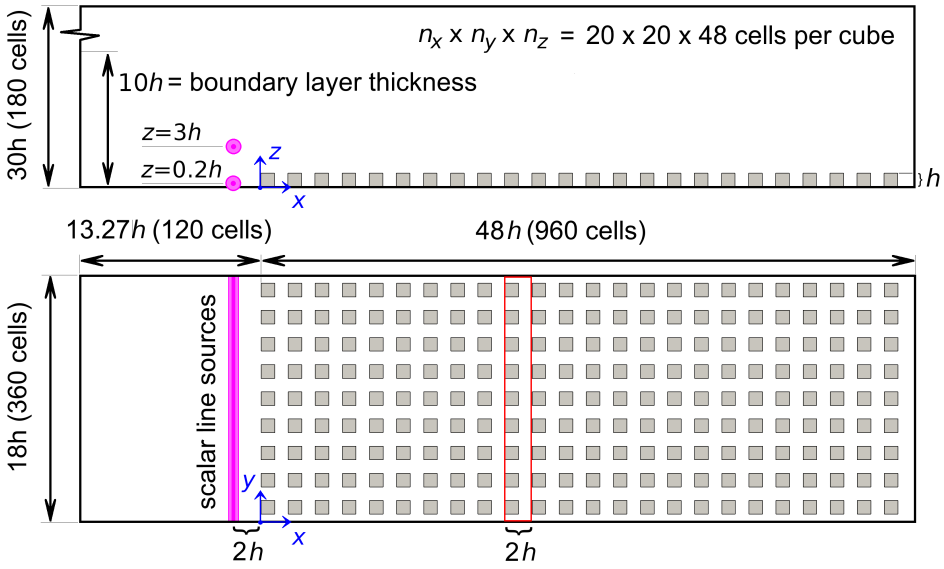

Figure 4.1: Domain for the RT simulations. The red rectangle represent the area over which the results for each row of cubes are averaged.

4.2.4 *Boundary Conditions*

For all cases periodicity in the spanwise direction was assumed for all variables. On the ground and obstacle walls no-slip conditions were applied, while at the top boundary a free-slip condition for the horizontal velocity components was used. For the scalars θ and c^* zero-flux boundaries were assumed, except for θ at the ground and the top of the obstacles, for which isothermal conditions ($\theta = \theta_0$) were applied. In this way the total area on which $\theta = \theta_0$ is imposed is equal to the smooth wall case, such that the average temperature boundary conditions in the canopy are similar to those for the approaching smooth-wall turbulent boundary layer. In addition, building rooftops experience a radiative cooling similar to the ground, but larger than the building side-walls. This suggests use of the same boundary conditions for the top of the cubes as are used for the ground surface.

4.2.4.1 *Driver and Roughness Transition Simulations.*

The inflow velocity and temperature fields were generated in separate D simulations; the instantaneous velocity field and temperature field at the inlet plane was saved in time and subsequently used as inflow data for the RT simulations. To assure statistically steady boundary-layer characteristics the D simulations used the recycling method proposed by Lund et al. (1998) for the velocity and a similar method for the temperature (Kong et al., 2000). The only differences are that the buoyancy force was taken into account in the simulations and a mass-flux correction was applied such

that the resulting inflow satisfied a constant mass flux. This procedure has been applied successfully before when considering a smooth-wall turbulent boundary layer approaching a single fence (Tomas et al., 2015c). At the outlet a convective outflow boundary condition was applied for all variables. At the top boundary a constant outflow velocity of $w = U_\infty \overline{\mathrm{d}\delta_1/\mathrm{d}x}$ was used, where $\overline{\mathrm{d}\delta_1/\mathrm{d}x}$ is the mean streamwise growth of the displacement thickness. This was done to establish a zero pressure gradient in the D simulations. The RT simulations used the same outflow velocity as in the D simulations.

4.2.4.2 *Periodic Roughness and Validation Simulations.*

At the top boundary zero vertical velocity was imposed. Periodicity was assumed in both horizontal directions and the flow was driven by a constant streamwise pressure gradient, $\partial\Pi/\partial x = u_\tau^2/L_z$, with $\Pi = \left(\widetilde{p} + \tau_{kk}/3\right)/\rho_0$. Analogously, in order to achieve a statistically steady state for the temperature field in the stable PR simulation a constant volumetric temperature source, $\mathcal{S}_\theta$, was applied in all cells to balance the loss of heat at the bottom of the domain,

$$\mathcal{S}_\theta = \frac{\nu}{\mathrm{Pr}\, L_z}\left(\frac{\partial\overline{\theta}}{\partial z}\right)_0, \tag{4.4}$$

where $(\partial\overline{\theta}/\partial z)_0$ is the mean temperature gradient at the ground. A similar approach is used in Boppana et al. (2014). One may question the appropriateness of such a volumetric heat source term, but it is a remedy to an inherent characteristic of the periodic boundary conditions that are, strictly speaking, not entirely valid in the first place. Alternatively, one could prescribe a balancing heat flux at the top of the domain, but such an approach is less suitable in this case, because it tends to create a thermal boundary layer at the top wall.

4.2.5 *Statistics*

A constant timestep of $0.01T$ was used in the neutral simulations and $0.02T$ in the stable simulations. In all simulations statistics were computed after a steady state was reached; for the PR simulations this was after 10×10^3 time scales, $T = h/U_\infty$. The D simulations required $20 \times 10^3 T$, starting from a coarse mesh simulation, while the RT simulations started from a steady-state solution generated with a steady mean inflow profile. They ran for a duration of $1300T$ of which the last $800T$ were used for computing statistics using an interval of $0.2T$. The total averaging interval of $800T$ resulted in statistically steady results. Coceal et al. (2006) describe the statistical convergence in terms of the eddy turnover time of the largest eddies shed by the obstacles, $T_\mathrm{e} = h/u_\tau$. They find a remaining circulation in the outer region when an averaging interval of $50T_\mathrm{e}$ is used, which no longer exists when the interval is increased to $400T_\mathrm{e}$. The averaging interval used for the RT simulations corresponds to about $56T_\mathrm{e}$. However, there was no remaining circulation found in the mean flow

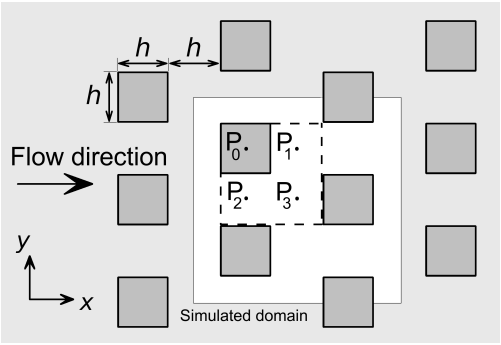

Figure 4.2: Experiment of Castro et al. (2006) with measurement locations Po–P3. The white area represents the V simulation domain. The dashed rectangle shows the repeating element.

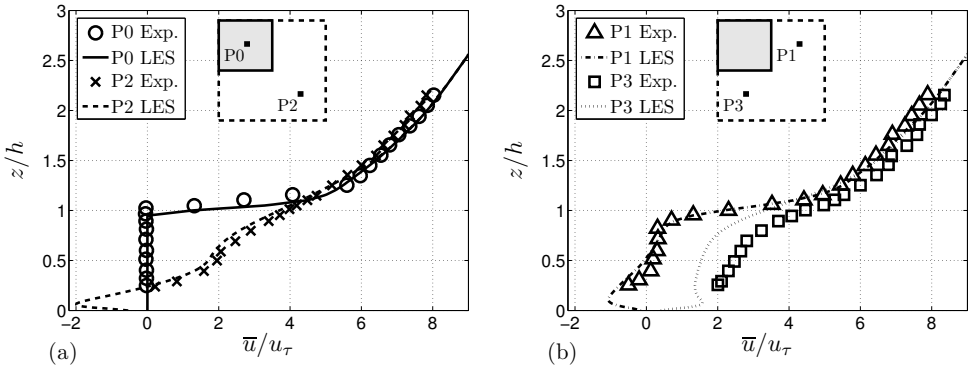

Figure 4.3: Mean streamwise velocity component at stations Po and P2 (a), and P1 and P3 (b). Experimental data from Castro et al. (2006).

field, most likely due to the inflow-outflow set-up in contrast to the double-periodic boundary conditions used in Coceal et al. (2006). Nevertheless, because the current results were averaged in the spanwise direction any remaining circulation is averaged out.

4.3 LES VALIDATION

The V simulation was performed to validate the model with data from wind-tunnel experiments (Castro et al., 2006). The experiments governed the flow over a staggered cube array for neutrally buoyant conditions. The geometry of the experiments is shown in Fig. 4.2. Measurements were done by means of hot-wire anemometry (HWA) outside the urban canopy and laser Doppler anemometry (LDA) within the urban canopy. The experimental set-up was similar to Cheng and Castro (2002b), in which more information is given on the experimental techniques. They obtained

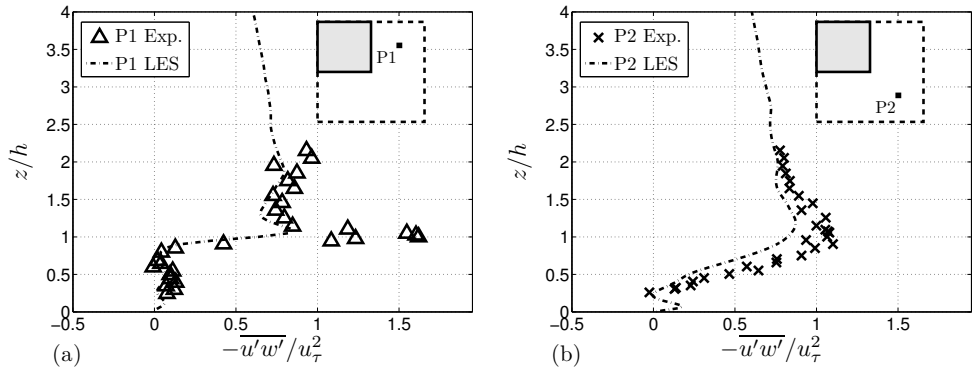

Figure 4.4: Mean Reynolds stress at stations P1 and P2. Experimental data from Castro et al. (2006).

vertical profiles of velocity statistics at four locations (P0-3). The roughness Reynolds number was 937, but similar results were found in Cheng and Castro (2002b) at $h^+ = 371$, which is the roughness Reynolds number used in the V simulation.

Figure 4.3 shows the vertical profile of the mean streamwise velocity component at four locations indicated in the figure. The agreement is quite satisfactory. However, the simulation overpredicts the length of the wake of the upstream cube, which causes the streamwise velocity component to be smaller than the experimental results at location P3.

Figure 4.4 shows the mean resolved Reynolds stress, $-\overline{u'w'}$, at locations P1 and P2. Unfortunately, experimental data are not available at location P3. The agreement between the model and experimental results is good, although the vertical resolution was too low to resolve the peak caused by the shear layer emanating from the top of the cube. This most likely also affected the aforementioned wake length. The vertical cell size at the top of the cubes was $0.05h$. In the RT and PR simulations this was decreased to $0.01h$ in order to capture the shear layer at the canopy height. In addition, the streamwise resolution was increased from 16 to 20 cells per cube.

For neutral stratification the mean wind profile is described by the logarithmic law,

$$\overline{u} = \frac{u_\tau}{\kappa} \ln\left(\frac{z-d}{z_0}\right), \tag{4.5}$$

where κ is the von Kármán constant ($= 0.4$), z_0 is the roughness length, and d is the displacement height, the height at which the total drag force acts (Jackson, 1981). It is computed by dividing the total moment of the drag forces by the total drag force. For the V simulation d was found to be $0.63h$, and by means of Eq. 4.5 z_0 was estimated to be $0.06h$. Using the same method of estimating these parameters Cheng and Castro (2002b) report $d = 0.61h$ and $z_0 = 0.075h$ for their experimental results. However, they also address the difficulty in determining these parameters due to the dependency on the applied method.

4.4 RESULTS OF LES OF FLOW ENTERING A GENERIC URBAN CANOPY

To investigate the effect of stable stratification on flow and dispersion for a rural-to-urban roughness transition two RT simulations were done; one for neutral conditions and one for stable conditions. Two corresponding D simulations were performed to generate the turbulent inflow. In addition, two (neutral and stable) PR simulations were done using conventional periodic boundary conditions in the horizontal directions. For the neutral (stable) case a value of 4.127×10^{-4} (7.650×10^{-5}) was found for the constant streamwise pressure gradient, $\left(h/U_\infty^2\right) \partial\Pi/\partial x$, in order that the velocity at the top of the domain was U_∞. For the stable case a value of 7.560×10^{-5} was found for the constant volumetric temperature source, $h\mathcal{S}_\theta / \left(\left[\theta_\infty - \theta_0\right] U_\infty\right)$, in order that the temperature at the top of the domain was θ_∞.

The applied level of stratification in the stable cases is described by the bulk Richardson number

$$\mathrm{Ri} = \frac{\left(g/\theta_0\right)\left(\theta_\infty - \theta_0\right)\delta}{U_\infty^2}, \tag{4.6}$$

which was 0.147 at the inlet of the stable D, RT, and PR simulations. Local effects of stratification are described by the gradient Richardson number

$$\mathrm{Ri}_{\mathrm{grad}} = \frac{g}{\theta_0}\frac{\partial\overline{\theta}}{\partial z} \Bigg/ \left(2\overline{S}_{ij}\overline{S}_{ij}\right), \tag{4.7}$$

which was 0.2 throughout most of the boundary layer in the D simulation. Increasing the stratification even more resulted in intermittent turbulence.

4.4.1 *Instantaneous Velocity Fields*

Figure 4.5 shows the contours of instantaneous velocity magnitude normalized with U_∞ for the neutral (top) and the stable case (bottom). At the inlet the flow is already turbulent (generated in the D simulations). Low speed streaks are visible in the horizontal plane at $z = 0.1h$. In the midplane both the neutral and the stable case show small scale turbulence generated by the roughness elements. However, in the stable case the exchange of momentum in the outer region is reduced as can be seen by the more layered velocity contours.

4.4.2 *Mean Velocity Field*

The mean flow is statistically homogeneous in the (periodic) spanwise direction only, because the flow is developing in the streamwise direction. Assuming the mean streamwise development occurs at a larger scale than a single pitch of $2h$ (i.e. a 'street') the mean flow can be averaged over each street area, as is shown in Fig. 4.1. This averaging operation is indicated by $\langle .. \rangle$. Figure 4.6 shows the spatially-averaged

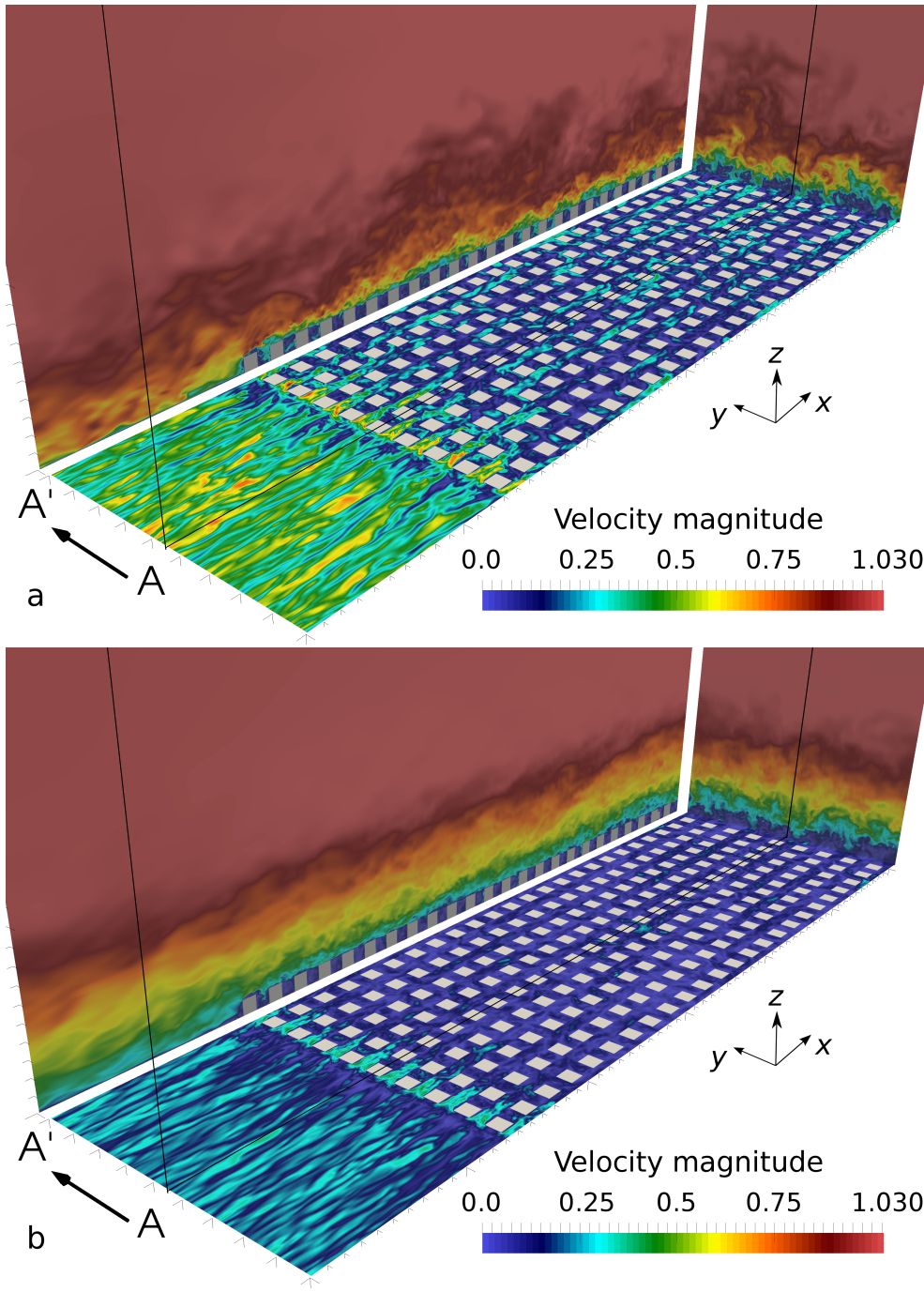

Figure 4.5: Contours of instantaneous velocity magnitude for the RT simulations; (a) neutral conditions; (b) stable conditions. The velocity magnitude is normalized with U_∞. Plane **A′** is a projection of midplane **A**. The x-y plane is located at $z/h = 0.1$ and cuts through the cubes.

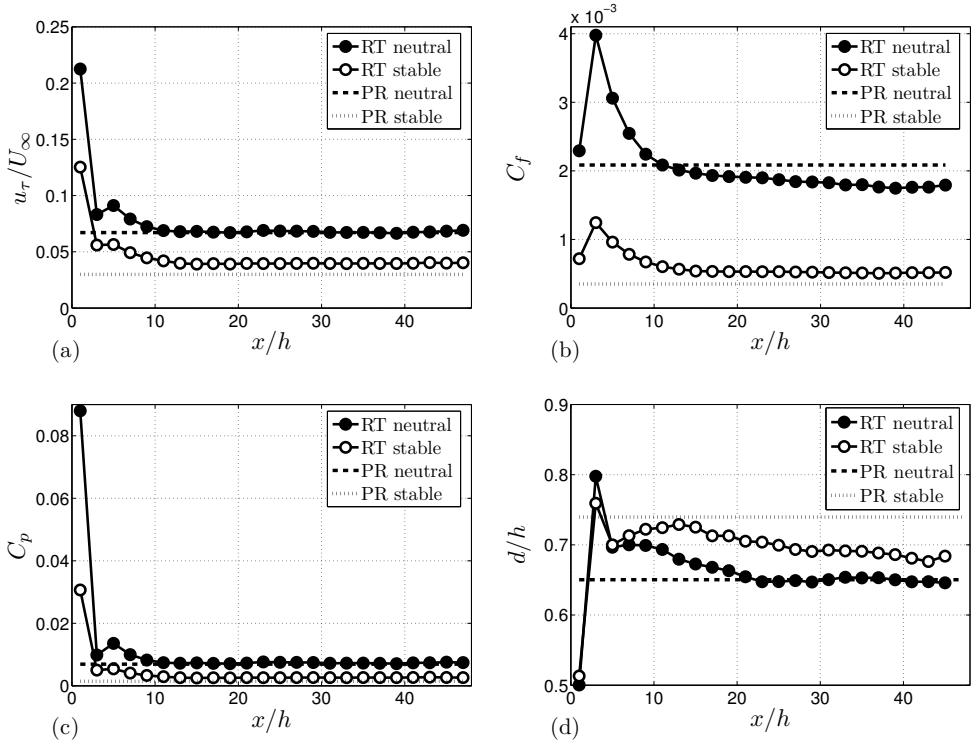

Figure 4.6: Mean street-averaged forces. (a) Friction velocity u_τ, (b) Skin friction coeffient C_f, (c) Form drag coefficient C_p, (d) Displacement height d. The dashed lines corresponds to the PR simulation results.

mean forces for both the neutral case and the stable case. The results of the PR simulations are also shown. The friction velocity u_τ (Fig. 4.6a) is computed from the total drag that consists of skin frictional drag, D_τ, and form drag, D_p. The drag forces are averaged over the area of each street;

$$D_\tau = \frac{1}{2hL_y} \int_{A_s} \overline{\tau}\, dA, \tag{4.8}$$

$$D_p = \frac{1}{2hL_y} \int_{A_f} \Delta\overline{p}\, dA, \tag{4.9}$$

where $\overline{\tau} = \rho_0 \nu \left(\partial\overline{u}/\partial n\right)_0$ is the mean wall shear stress, A_s is the total area of all surfaces in each street (i.e. the top and side faces of the cubes as well as the ground surface), $\Delta\overline{p}$ is the mean pressure difference between upwind and downwind faces of the cubes and A_f is the frontal area of the cubes in each street. When u_τ reaches a constant value this is an indication of fully-developed flow at the obstacle height. For both the neutral and the stable cases this occurs after approximately seven streets ($= 14h$). At the inlet u_τ is $0.0377U_\infty$ for the neutral case and $0.0172U_\infty$ for the stable case. In the canopy the neutral case converges to a friction velocity 1.84 times larger than at the inlet. The stable flow experiences a higher drag increase by the canopy because at the end of the domain u_τ/U_∞ is 2.35 times the inlet value. The skin friction coefficient, $C_f = D_\tau / \left(\frac{1}{2}\rho U_\infty^2\right)$, and the form drag coefficient, $C_p = D_p / \left(\frac{1}{2}\rho U_\infty^2\right)$, are shown as well (Fig. 4.6b and Fig. 4.6c, respectively). In the developed region form drag constitutes 76% (81%) of the total drag in the neutral (stable) case. This is 70% (76%) in the PR simulations. Finally, Fig. 4.6d shows the displacement height d (as defined in Sect. 4.3) for the four cases. Although the force coefficients seem to converge to the values found in the corresponding PR simulation, the displacement height for the RT simulation in stable conditions is significantly lower than found in the PR simulation; at the end of the domain d is $0.68h$ (RT) instead of $0.74h$ (PR). This result suggests that in stable conditions the flow at the end of the RT domain differs from the fully-developed case (PR simulation).

To investigate the streamwise development of the boundary layer Fig. 4.7 shows the vertical profiles of $\langle\overline{u}\rangle$ at streets 1, 4, 8, 12, 16, 20, and 24 for both neutral conditions (Fig. 4.7a) and stable conditions (Fig. 4.7b). The continuous black lines represent the RT results. To compare with flow over a smooth wall, i.e. without the roughness transition, the results from the D simulations are shown as the blue dashed lines. Clearly, the roughness transition introduces a large velocity defect that results in an internal boundary layer, whose depth is indicated as δ_i. In the next section it will be explained how it is determined.

The PR simulations are presented by a single temporally- and spatially-averaged profile of the streamwise velocity component; it is shown at each downstream location (red dash-dotted lines in Fig. 4.7) in order to investigate to what extent the flow in the RT simulations has adapted to the increased roughness and when it can be considered fully developed. For neutral conditions at the 24th street the velocity defect

has smoothly blended with the outer flow velocity profile such that the full velocity profile is nearly indistinguishable from the PR results. This suggests the mean flow has practically adapted to the surface roughness. However, for stable conditions the velocity profile of the RT simulation at the 24th street does not (yet) agree with the velocity profile of the PR simulation. Near the canopy there is a layer with increased shear compared to the smooth-wall flow that reaches up to the internal boundary-layer height. Above that region the velocity profile follows the smooth-wall profile. In contrast, the velocity profile of the PR simulation does not show these two regions, but a single smooth profile instead.

In Fig. 4.8a the corresponding temperature profiles are plotted showing that inside the canopy in the RT and PR simulations $\partial\langle\overline{\theta}\rangle/\partial z$ is decreased compared to the D simulation. In addition, in the internal boundary layer in the RT simulation $\langle\overline{\theta}\rangle$ is smaller than in the D simulation, while above the internal boundary layer $\langle\overline{\theta}\rangle$ is similar to the values found in the D simulation. As a consequence of these velocity and temperature profiles in the RT simulation the gradient Richardson number, $\mathrm{Ri}_{\mathrm{grad}}$ (Eq. 4.7), is decreased in the internal boundary layer compared to the D simulation, as shown in Fig. 4.8b. The D results show a nearly constant $\langle\mathrm{Ri}_{\mathrm{grad}}\rangle$ of about 0.2 from $z = h = 0.1\delta$ up to $z = 6h = 0.6\delta$, above which $\langle\mathrm{Ri}_{\mathrm{grad}}\rangle$ increases to 0.26. In the results for the PR simulation $\langle\mathrm{Ri}_{\mathrm{grad}}\rangle$ increases approximately linearly from 0.05 at $z = 1.3h = 0.13\delta$ to 0.24 at the top of the boundary layer ($= 10h$). The fact that there are two regions in the RT results — the aforementioned region of low $\langle\mathrm{Ri}_{\mathrm{grad}}\rangle$ in the internal boundary layer and a region above the internal boundary layer with values of $\langle\mathrm{Ri}_{\mathrm{grad}}\rangle$ that correspond to the inflow boundary layer — indicates that for stable conditions the flow field has not yet adapted to the increased surface roughness. Moreover, the streamwise velocity component in the PR simulation for stable conditions differs from the neutral case indicating that also for fully-developed conditions at this bulk Richardson number buoyancy effects are still important.

4.4.3 *Internal Boundary-Layer Growth*

There exist several definitions of the internal boundary-layer depth, δ_i, (Garratt, 1990). In a study on flow over cubical roughness arrays (Cheng and Porté-Agel, 2015) δ_i is defined as the height at which $\overline{u}$ reaches 99% of the upstream velocity. However, because the simulated domain has a finite height ($L_z = 3\delta$ in the current study and $L_z = 1.08\delta$ in Cheng and Porté-Agel (2015)) the flow accelerates due to the blockage by the canopy. Therefore, with their definition, δ_i depends on the domain height that is used, which is undesirable. In the present study δ_i is found by subtracting the mean streamwise velocity component found in the D simulations (smooth wall) from the mean streamwise velocity component found in the RT simulations: $\Delta\langle\overline{u}\rangle = \langle\overline{u}\rangle_{RT} - \langle\overline{u}\rangle_D$, and δ_i is defined as the height at which the vertical gradient of $\Delta\langle\overline{u}\rangle$ reaches zero. This approach — and probably any method using the gradient of $\overline{u}$ instead of $\overline{u}$ (see also the review by Garratt (1990)) — eliminates the difficulty of discerning δ_i when the flow accelerates above the canopy due to a finite domain height.

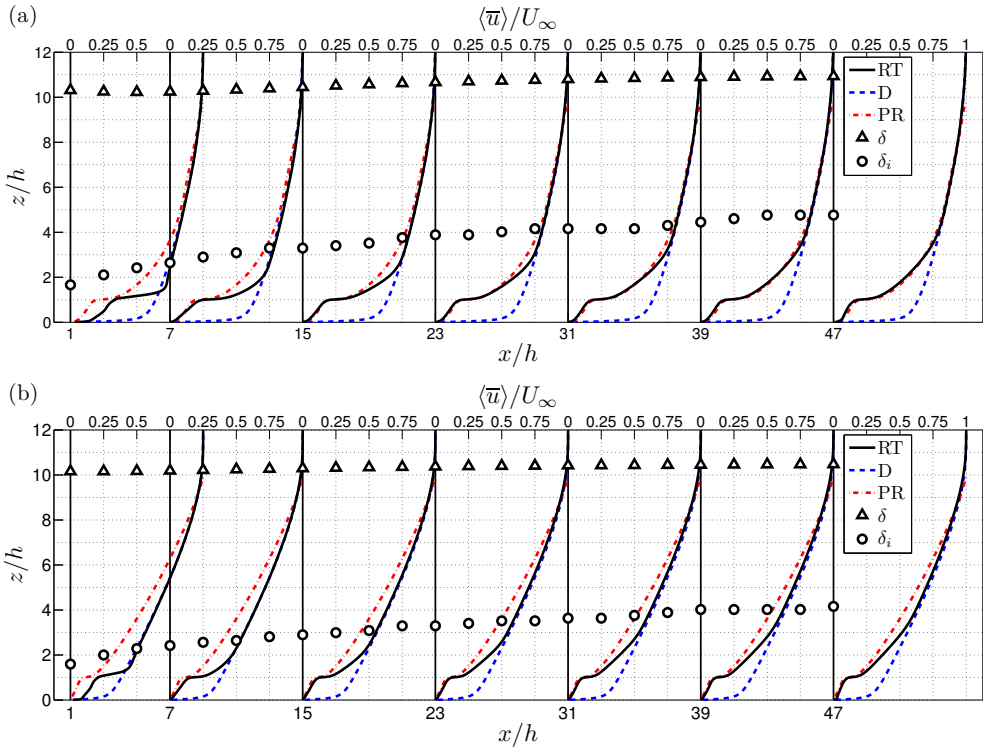

Figure 4.7: Streamwise development of $\langle\overline{u}\rangle$ for, (a) neutral conditions, and (b) stable conditions.

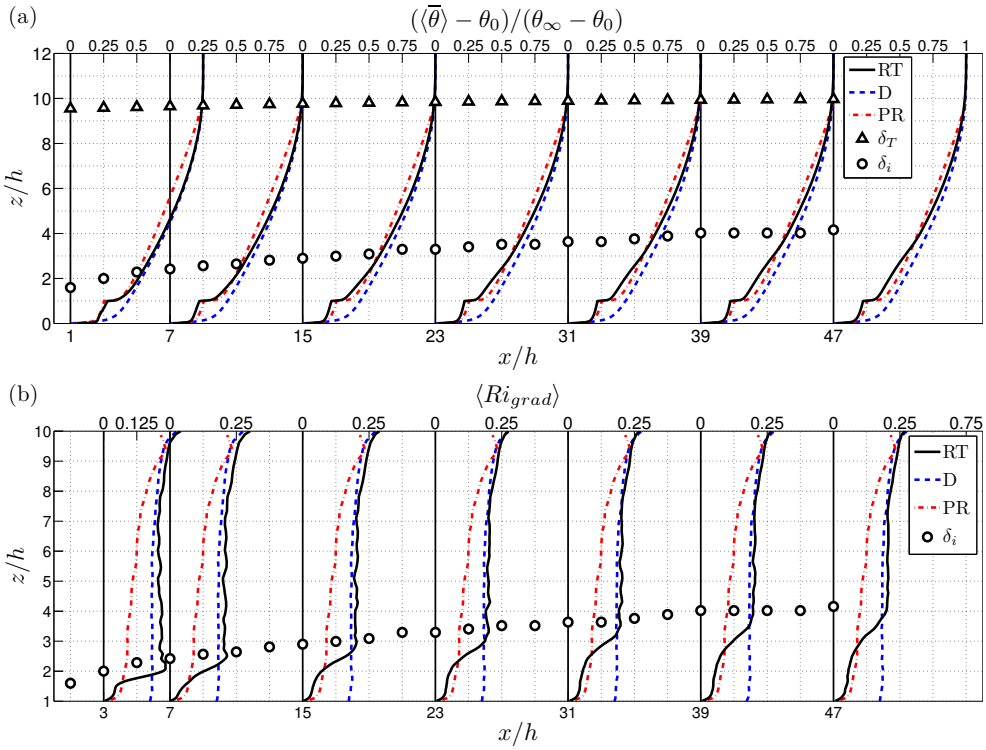

Figure 4.8: Streamwise development of, (a) $\langle\overline{\theta}\rangle$, and (b) $\langle \mathrm{Ri}_{\mathrm{grad}}\rangle$ for stable conditions.

The resulting δ_i is shown in Fig. 4.7 and Fig. 4.8 by circles. For stable conditions δ_i grows more slowly than for neutral conditions: δ_i is 14% smaller at the end of domain. In Cheng and Porté-Agel (2015) nearly the same configuration is considered for neutral conditions only. As expected, δ_i found in that study is smaller due to the different definition of δ_i. They find δ_i to be approximately $2.5h - 3.0h$ at street 15 compared to $4.2h$ at the same location in the current results. However, using their definition of δ_i a value of $3.1h$ is found at street 15 in the current results. The slight difference that remains could be explained by the smaller domain height used in Cheng and Porté-Agel (2015), making it more prone to acceleration due to blockage by the canopy. However, there are probably also differences due to the wall modelling they apply and the larger Reynolds number they consider (Re_h based on h and the upstream velocity at $z = h$ is 3×10^4 in Cheng and Porté-Agel (2015) compared to 3.2×10^3 (neutral) and 4.3×10^3 (stable) in the current results).

Furthermore, the full boundary-layer depth, δ, is also shown in Fig. 4.7. The results for stable conditions show that at the 24th street δ is 4% smaller than for neutral conditions, while for the imposed flow at the inlet δ is the same for both cases.

4.4.4 *Turbulence Kinetic Energy Budget*

To investigate further the effects of stratification on flow over a roughness transition all terms in the mean resolved turbulence kinetic energy (TKE) budget are considered for the D, RT, and PR simulations. The equation governing the mean resolved TKE can be found by multiplying the Navier-Stokes equations by u_i, applying temporal averaging, and subtracting the kinetic energy of the mean flow. The result of these operations is the equation for $\frac{1}{2}\overline{u_i' u_i'}$,

$$\overbrace{\overline{u}_j \frac{\partial \frac{1}{2}\overline{u_i' u_i'}}{\partial x_j}}^{A} = \overbrace{-\overline{u_j' \frac{\partial \Pi'}{\partial x_j}}}^{T_p} \overbrace{- \frac{\partial}{\partial x_j}\left(\frac{1}{2}\overline{u_i' u_i' u_j'}\right)}^{T_t} \overbrace{+ \frac{\partial}{\partial x_j}\left(2\nu \overline{u_i' S_{ij}'}\right)}^{T_v} \overbrace{- \frac{\partial}{\partial x_j}\left(\overline{u_i' \tau_{ij}'}\right)}^{T_{sgs}} \underbrace{+ \frac{g}{\theta_0}\overline{u_i' \theta'}\delta_{i3}}_{P_b} \underbrace{- \overline{u_i' u_j'}\,\overline{S}_{ij}}_{P_t} \underbrace{- 2\nu \overline{S_{ij}' S_{ij}'}}_{D_v} \underbrace{+ \overline{\tau_{ij}' S_{ij}'}}_{D_{sgs}}, \tag{4.10}$$

where A represents advection by the mean flow, T_p is the transport by pressure fluctuations, T_t is the transport by turbulent velocity fluctuations, T_v is the transport by viscous stresses, T_{sgs} is the transport by SGS stresses, P_b is the production/destruction by buoyancy fluctuations, P_t is the production by shear, D_v is the resolved viscous dissipation, and D_{sgs} is the SGS dissipation, which represents the transfer of energy from resolved scales to subgrid scales. Figure 4.9 shows the vertical profiles of these terms for the D, RT, and PR simulations, where at each vertical position the data are scaled with the total production. The graphs in Fig. 4.9a,c,e are for neutral conditions and the graphs in Fig. 4.9b,d,f are for stable conditions. Figure 4.9a,b contain the D results, Fig. 4.9c,d contain the RT results at street 23, and Fig. 4.9e,f show the PR results. Note that T_{sgs} has been added to T_t and D_{sgs} has been added

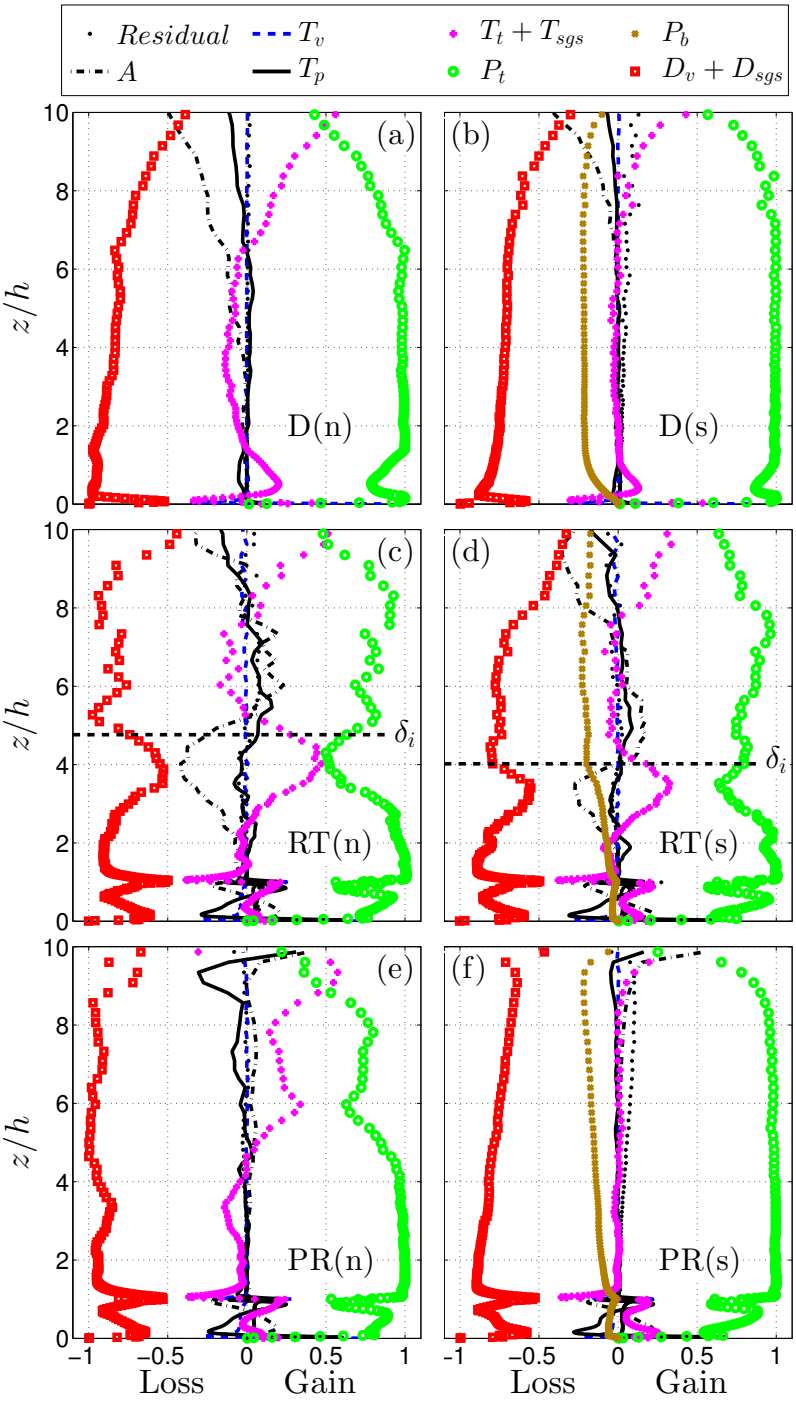

Figure 4.9: Vertical profiles of resolved TKE budget terms scaled with total production at each height. (a), (c), and (e): Neutral conditions (indicated by (n)). (b), (d), and (f): Stable conditions (indicated by (s)). (a) and (b): D simulations. (c) and (d): RT simulations, street 23 ($x = 47h$). (e) and (f): PR simulations. The horizontal dashed line represents δ_i.

to D_v. T_{sgs} is found to be negligible throughout the flow field except in the first cells near to the walls, where it is the same order of magnitude as T_t. Up to $z = 0.7\delta$ D_{sgs} is around 40% of the total dissipation, which implies that still 60% of the TKE dissipation is resolved. For $z > 0.7\delta$ the resolved part increases to 100%.

The results for the D simulations show that the main difference between neutral and stable conditions is that for $z > h$ the buoyancy destruction term, P_b, is over 21% of the total destruction of TKE for the stable case. Below $z = h$ P_b decreases to zero. In addition, in stable conditions advection by the mean flow and transport due to turbulent velocity fluctuations are reduced. In the region $z = 1h - 6h$ the TKE budget can be approximated by considering the production, dissipation, and buoyancy destruction terms only.

The RT results at street 23 show that above the internal boundary layer the results are similar to the results from the D simulations. This shows that above $z = \delta_i$ the roughness transition is not (yet) felt. The profiles just below $z = \delta_i$ bear a strong resemblance to the upper regions ($z > 6h$) of the D and RT cases, which confirms the existence of an internal boundary layer. For stable conditions the P_b term shows a clear change at $z = \delta_i$, below which it decreases to almost zero at the canopy height. The fact that this change occurs exactly at $z = \delta_i$ gives confidence that the applied criterion to find δ_i, as described in Sect. 4.4.3, is appropriate. Furthermore, it is concluded that in the canopy the profiles for the stable case are almost the same as for the neutral case and the P_b term is reduced to below 4% of the total TKE destruction. In addition, just as for the D simulations advection by the mean flow and transport due to turbulent velocity fluctuations are lower in stable conditions. This explains the slower development of the flow in terms of surface forces (Fig. 4.6) and internal boundary-layer depth (Sect. 4.4.3).

Finally, it is concluded that the PR results for stable conditions show no discontinuity in P_b, because there is no internal boundary layer. However, the magnitude of P_b increases linearly with height up to the top of the boundary layer in contrast to the D simulation where P_b is approximately constant. The same behaviour is visible for $\langle \mathrm{Ri}_{\mathrm{grad}} \rangle$ (Fig. 4.8b).

4.4.5 *Pollutant Dispersion*

Emissions from two line sources of passive scalar were considered to investigate the effect of stratification on pollutant dispersion. Source 1 was located above the canopy at $z/h = 3$ and Source 2 was located below the canopy top at $z/h = 0.2$. Both sources were placed $2h$ in front of the first row of cubes. Figure 4.10 shows the resulting instantaneous concentration fields in the x-z plane in the middle of the domain for Source 1 for neutral (Fig. 4.10a) and stable conditions (Fig. 4.10b). The concentration c^* is normalized by U_∞, h, L_y, and the emission mass flow rate Q: $c = c^* U_\infty h L_y / Q$. The difference in vertical mixing between the two cases is clearly visible since the neutral case shows a meandering plume while in the stable case the plume axis remains at approximately the same vertical position. As a result the concentrations stay high over a larger distance in the stable case. Moreover, because the internal

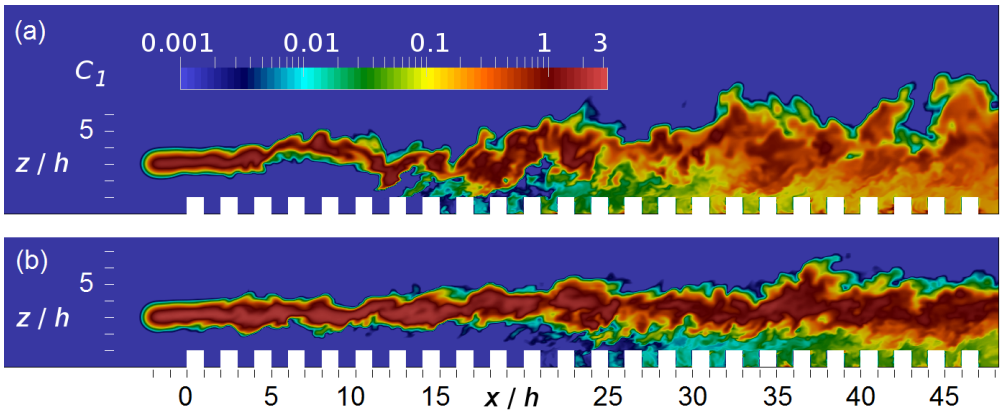

Figure 4.10: Instantaneous concentration released from Source 1 in the x-z plane at $y/h = 9$; (a) neutral conditions; (b) stable conditions. Logarithmic colour scaling

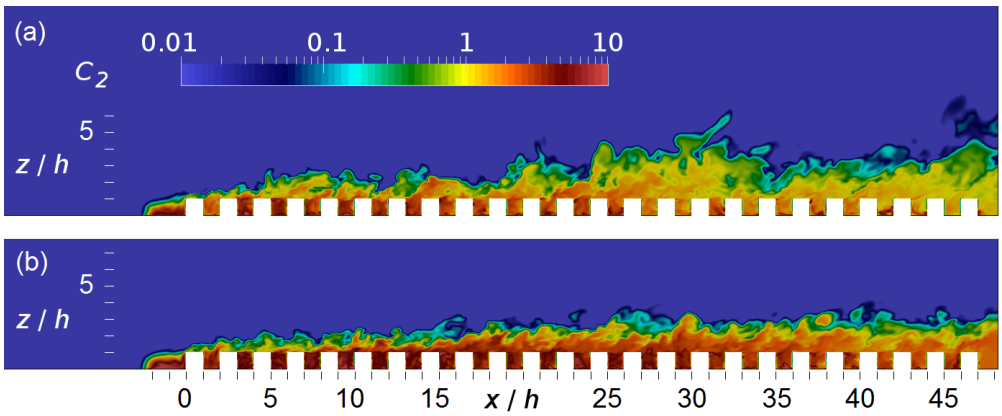

Figure 4.11: Instantaneous concentration released from Source 2 in the x-z plane at $y/h = 9$; (a) neutral conditions; (b) stable conditions. Logarithmic colour scaling

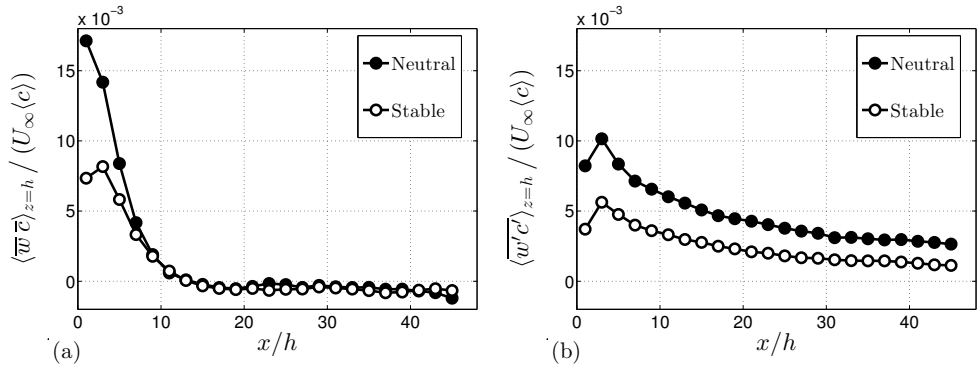

Figure 4.12: Streamwise development of the mean street-average vertical pollutant flux $\langle \overline{w}\overline{c} \rangle_{z=h}$ for Source 2, scaled with the freestream velocity and mean street-average concentration; (a) advective pollutant flux; (b) turbulent pollutant flux. The SGS flux is included.

boundary layer grows more slowly in stable conditions entrainment into the urban environment occurs farther downstream; for the domain considered here the average concentration within the volume of each street is higher for the neutral case.

Figure 4.11 shows the instantaneous concentration fields in the x-z plane in the middle of the domain for Source 2 for neutral (Fig. 4.11a) and stable conditions (Fig. 4.11b). Throughout the canopy the average concentration within the volume of each street is in the stable case approximately 85% higher than the neutral case. The lower streamwise advection velocity component $\overline{u}$ (see Fig. 4.7) is the main cause of the difference. However, if c^* is scaled with the mean streamwise velocity component at the canopy height concentrations are still 17% larger than the neutral case. This corresponds exactly to the difference in δ_i between neutral and stable conditions. In other words, when the emission source is below the canopy top, there are two reasons why stably stratified conditions produce higher canopy concentrations: (1) The streamwise advection is decreased, and (2) pollutants are trapped in the internal boundary layer, which grows more slowly than in neutral conditions.

Finally, we consider the vertical flux of pollutant out of the canopy. For each street the total average vertical pollutant flux can be defined as

$$\frac{1}{2hL_y}\int_0^{2h}\int_0^{L_y} \overline{wc}|_{z=h}\, dy\, dx = \overbrace{\langle \overline{wc} \rangle_{z=h}}^{\text{total}} = \overbrace{\langle \overline{w}\,\overline{c} \rangle_{z=h}}^{\text{advection}} + \overbrace{\langle \overline{w'c'} \rangle_{z=h}}^{\text{turbulence}} \tag{4.11}$$

To obtain insight into the mechanisms that contribute to the vertical street emission the total pollutant flux is split up into a contribution due to mean advection, $\overline{w}\,\overline{c}$, and a contribution due to turbulent motions, $\overline{w'c'}$. Figure 4.12 shows the streamwise development of both contributions, with the SGS contribution to the turbulent pollutant flux included in the results. Its magnitude did not exceed 10% of the total vertical turbulent pollutant flux. After approximately seven streets the mean vertical advect-

ive flux (Fig. 4.12a) is slightly negative and negligible compared to the mean vertical turbulent flux (Fig. 4.12b) in agreement with the results for fully-developed flow reported by Michioka et al. (2014). However, the mechanism of pollutant removal from the canopy in the first seven streets is different because of the increased vertical velocity component, which results in significant advective pollutant flux. Moreover, the results show that stratification does not influence this behaviour, but does cause the vertical turbulent pollutant flux to decrease.

4.5 CONCLUSIONS

Large-eddy simulations (LES) were used to investigate the effect of stable stratification on flow and pollutant dispersion in a turbulent boundary layer entering a generic urban environment. The applied LES method was validated in Tomas et al. (2015a,c) by comparing with experimental data for flow over a surface-mounted fence and is further validated here for flow over cubical roughness by comparing with experimental results of Castro et al. (2006). At all examined locations the vertical profiles for the mean streamwise velocity component, as well as the mean Reynolds stress, show good agreement and minor discrepancies can be explained.

Subsequently, LES for both neutrally buoyant and stably stratified boundary layers entering a generic urban roughness are performed. The inflow turbulent boundary layers were generated in separate driver (D) simulations. To compare with fully-developed flow two additional simulations (PR) were done using periodic boundary conditions in the horizontal directions.

Regarding the question about how a stratified boundary layer responds to a roughness transition, it is concluded that the surface forces in both neutral and stable conditions become approximately constant after seven streets ($= 14h$) downstream from the start of the canopy and that for stable conditions the flow experiences a larger increase in u_τ than for neutral conditions. Moreover, it is found that for neutral conditions after 24 streets ($= 48h$) the mean streamwise velocity component is almost indistinguishable from the results of the PR simulation (fully-developed flow). However, this does not hold for the stably stratified boundary layer that develops more slowly. Investigation of the terms in the TKE budget equation shows that at the end of the simulated domain both the neutral and the stable boundary layer are still adapting to the increased roughness: a clear internal boundary layer is visible in the RT results, above which there are strong similarities with the D simulations.

Furthermore, it is found that in stable conditions at the 24th street the internal boundary-layer depth, δ_i, is 14% shallower compared to neutral conditions. For neutral conditions δ_i is compared with LES results from Cheng and Porté-Agel (2015) showing a discrepancy that is related to the criterion used to find δ_i. It is argued that δ_i based on the gradient of the velocity defect (caused by the urban canopy) is preferable, because it does not depend on the domain height of the LES.

Regarding the issue as to whether or not stratification effects are diminished due to the turbulence generated by the roughness elements, it is concluded that the buoyancy destruction of TKE is indeed reduced in the internal boundary layer (from 21%

of the total loss of TKE above the internal boundary layer to zero at the top of the obstacles). However, the buoyancy destruction term does increase with height inside the internal boundary layer up to the value found in smooth-wall flow. Moreover, at the considered bulk Richardson number also for fully-developed flow buoyancy effects are still important, because the profile of the streamwise velocity component of the PR simulation for stable conditions still differs from the neutral results.

Regarding the effects of the roughness transition and stratification on pollutant dispersion it is concluded that in stable conditions pollutants emitted from a line source at $z = 3h$ enter the urban canopy at a location farther downstream than for neutral conditions. This is due to decreased vertical mixing that causes pollutants to be advected farther downsteam before entering the urban canopy. As a consequence average street concentrations for the considered domain are lower for stable conditions.

For pollutants emitted from a line source in front of the canopy close to the ground it is concluded that average street concentrations are 85% higher for stable conditions. Basically, there are two causes for the increased concentration: (1) The streamwise advection is decreased, and (2) pollutants are trapped in the internal boundary layer, which grows more slowly than in neutral conditions. The first can be accounted for if the concentration is normalized by the streamwise velocity component at the top of the canopy, which still results in 17% higher concentrations than for neutral conditions. This corresponds exactly to the ratio of δ_i for stable and neutral conditions. This result suggests that average canopy concentrations could be predicted when the average advection velocity and average internal boundary-layer depth are known.

Furthermore, the average vertical emission of pollutant out of each street is considered and it is found that the contribution of the advective pollutant flux is significant for the first seven streets after which the vertical pollutant emission is only governed by the turbulent flux similar to the fully-developed case.

Studies on flow over roughness (transitions) and internal boundary-layer development mostly investigate the effect of various roughness properties such as geometry and obstacle density. For example, Cheng and Porté-Agel (2015) show there is no significant difference in internal boundary-layer development for different cube configurations and densities. (This assumes that their aformentioned criterion used to define δ_i has no influence on this conclusion). The results presented here indicate that stable stratification, and probably the characteristics of the upstream flow in general, influences internal boundary-layer development over large distances. Therefore, it is recommended that the scope of future investigations should be expanded to include approaching flow properties.

4.6 ACKNOWLEDGEMENTS

This study was done within the STW project DisTUrbE (project no. 11989) using the computational resources of SURFsara with the funding of the Netherlands Organisation for Scientific Research (NWO), project no. SG-015. Furthermore, the authors thank Jerke Eisma for fruitful discussions.

5

RURAL-TO-URBAN TRANSITIONS: THE INFLUENCE OF ROUGHNESS GEOMETRY[1]

5.1 INTRODUCTION

Because there is a worldwide increase of urban areas, more pollutant emission sources, such as from power generation, households, and traffic, are present near populated areas. As a consequence, the demand for accurate urban air quality predictions is rising, which requires proper understanding of the dispersion of pollutants in urban environments. Investigations of the urban boundary layer are often done for fully-developed flow over areas with uniform properties, e.g. Cheng and Castro (2002b) did experiments on turbulent boundary layers where the complete bottom wall of the wind tunnel was covered with cubical roughness elements, that would represent the flow over an urban area. In multiple simulation studies the fully-developed character of the flow is implicitly assumed by employing periodic boundary conditions in the horizontal directions (e.g. Coceal et al. (2006); Michioka et al. (2014); Boppana et al. (2014)). However, in reality the surface roughness changes, e.g. from rural to urban regions, which means the boundary layer has to adapt to this roughness transition. There are only a few recent numerical studies on turbulent flow over an explicitly resolved roughness transition (Lee et al., 2011; Cheng and Porté-Agel, 2015), where mostly cubical roughness elements or riblets are considered. In addition, experimental investigations with results up to the roughness elements are scarce, and if a roughness transition is considered it is often done to find out when the boundary layer retains an equilibrium state, without investigating pollutant dispersion (Cheng and Castro, 2002a).

In order to obtain insight in pollutant dispersion mechanisms, Michioka et al. (2014) performed large-eddy simulations (LES) on fully-developed flow over an array of obstacles with various aspect ratios l / h, where l is the spanwise obstacle length and h is the obstacle height. They conclude that for fully-developed conditions the turbulent pollutant flux is the main contributor to street canyon ventilation, although the ratio of the turbulent to the advective pollutant flux does change slightly for different aspect ratios. Tomas et al. (2016b) show that up to $14h$ downstream of a

1 This chapter is under review for publication as a research article as: Tomas, J. M., Eisma, H. E., Pourquie, M. J. B. M., Elsinga, G. E., Jonker, H. J. J., and Westerweel, J. (2016a). Pollutant Dispersion in Boundary Layers Exposed to Rural-to-Urban Transitions: Varying the Spanwise Length Scale of the Roughness. *(under review)*

rural-to-urban roughness transition the advective pollutant flux remains significant. Furthermore, Michioka et al. (2011) and Michioka et al. (2014) conclude that street canyon ventilation mostly takes place when low momentum regions pass over the canyon, and they suggest that these regions are of small scale compared to the coherent structures in the outer region and are generated close to the top of the canopy.

Currently, there are only few experimental investigations on urban geometries in which concentration fields and velocity fields are measured simultaneously, such that these dispersion mechanisms can be investigated (Vinçont et al., 2000). To the authors knowledge there is no such experimental data available for regions containing multiple street canyons that allow a study on the streamwise development. Therefore, in the current study both LES and experimental measurements were performed to investigate pollutant dispersion mechanisms after a rural-to-urban roughness transition in neutrally buoyant conditions. The set-up is similar to Tomas et al. (2016b), where the urban canopy consists of cubical obstacles in an in-line arrangement. In addition, in the current study various urban canopies are considered by varying the spanwise aspect ratio of the obstacles. The experiments were done in the water tunnel at the Laboratory for Aero- and Hydrodynamics at the Delft University of Technology using simultaneous stereoscopic particle image velocimetry (PIV) and laser-induced fluorescence (LIF) techniques in order to investigate instantaneous pollutant dispersion mechanisms. The objectives of the study are (1) to set up a well-validated data-set for flow and pollutant dispersion and (2) to answer the following questions:

- What is the influence of the aspect ratio l/h on flow over a rural-to-urban transition, in terms of velocity statistics, internal boundary-layer depth, surface forces, and pollutant dispersion?
- What are the dominant mechanisms of pollutant removal from street canyons and how do these mechanisms change in the transition region?

In Sect. 5.2 the details of the considered cases are given, as well as information on the experimental set-up, measurement techniques, and the numerical method. Section 5.3 covers the comparison of the experimental and numerical turbulent inflow profiles, the presentation of the flow statistics, as well as the surface forces and internal boundary-layer growth. In Sect. 5.4 the experimental and numerical results on pollutant dispersion are presented and the pollutant dispersion mechanisms are investigated. Finally, in Sect. 5.5 the conclusions are given.

5.2 MATERIALS & METHODS

5.2.1 *Considered Cases*

In both the experiments and the simulations a smooth-wall turbulent boundary layer was generated that approached an urban roughness geometry consisting of an array of obstacles. The Reynolds number of the approaching flow, $\mathrm{Re}_\tau = u_\tau \delta_{99}/\nu$, based on the friction velocity $u_\tau = \sqrt{\nu \partial u/\partial z}$ and the boundary-layer depth δ_{99}, was 2.0×10^3 in

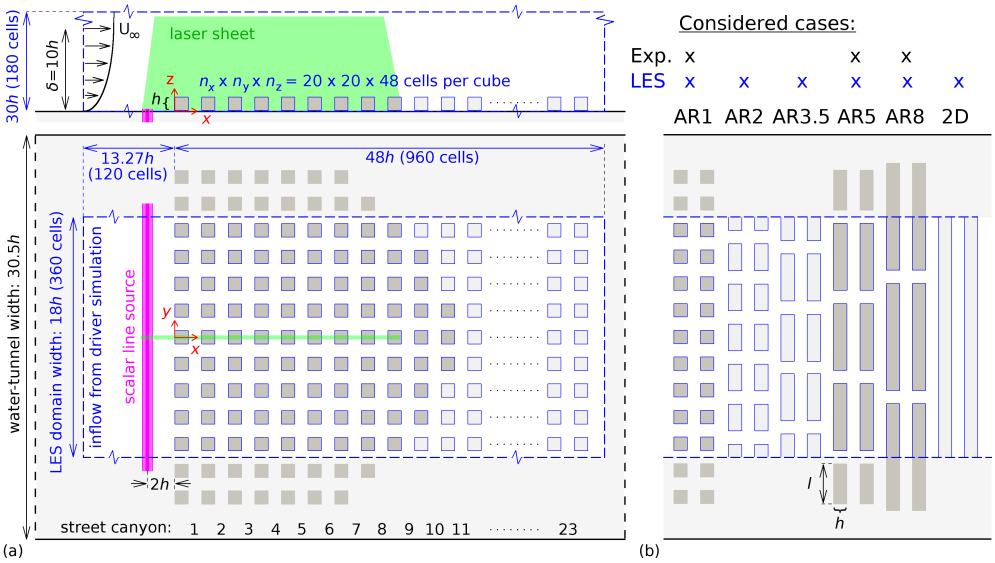

Figure 5.1: A schematic overview of the experimental and numerical set-up (a) and an overview of the cases that are considered in the experiments and in the simulations (b). The experimental set-up is shown by black lines and dark grey obstacles, while the numerical domain is shown by blue lines and light grey obstacles. The green line represents the laser sheet.

both cases. Figure 5.1a shows the top view and the side view of both the experimental set-up (black lines) and the domain used in the LES (blue lines). The location $x = 0$ corresponds to the upstream walls of the first row of obstacles, while the plane $y = 0$ lies in the middle of the domain at the symmetry plane of the obstacles. A uniform street layout of obstacles placed in an in-line arrangement was considered to capture the basic characteristics of urban areas. The parameter that was varied is the obstacle aspect ratio l/h; aspect ratios of 1, 2, 3.5, 5, 8, and ∞ were simulated by LES, while aspect ratios of 1, 5, and 8 were investigated in the experiments. Figure 5.1b shows the top view of the different cases, which are indicated by AR1, AR2, AR3.5, AR5, AR8, and 2D. For each case two 'streets' are shown that consist of an obstacle row and a 'street canyon'. In all cases the width of the obstacles as well as the width of all street canyons was equal to h. Consequently, the plan area density $\lambda_p = A_p/A_t$ was equal to the frontal area density $\lambda_f = A_f/A_t$, where A_t is the total area viewed from the top, A_p is the total area covered with obstacles, and A_f is the total frontal area of the obstacles. $\lambda = \lambda_f = \lambda_p$ was between 0.25 (AR1) and 0.5 (2D), and all cases were in the skimming flow regime (Oke, 1988). In addition, a line source of passive tracer was placed in front of the urban environment to simulate an emission from a highway as is often found near urban regions. Its location was $2h$ upstream of the first row of obstacles. In the experiments the tracer was released from the ground surface, while in the simulations the source was located at $z/h = 0.2$. After these properties of the test cases were determined, the experiments and simulations were done independently.

5.2.2 *Experimental Set-up*

5.2.2.1 *Layout*

The transparent test section of the water-tunnel has a length of 5.0 m and a cross-section of 0.6×0.6 m^2, which enables good access for optical measurement techniques, like the currently employed PIV and LIF techniques.

A false bottom, with dimensions 4.5×0.6 m^2, was mounted 0.17 m above the bottom tunnel wall to limit the influence of remaining flow disturbances emanating from the contraction to the measurement section, as well as to allow the placement of the scalar line source. As shown by Irwin (1981), an artificially thickened boundary layer can be obtained by employing so-called spires. In the current experiment four of these Irwin-type spires were mounted 0.50 m downstream of the sharp leading edge, and spanwise homogeneity of the flow was optimized by their placement. A schematic drawing indicating the different components of the experimental set-up is given in Fig. 5.2. An additional fence with a height of 2.0 cm was placed 12 cm upstream of the spires in order to generate an additional momentum deficit at the start of the boundary-layer development, as in, for instance, Savory et al. (2013). As flat terrain is considered as the upstream fetch, no additional roughness elements were added downstream of the spires. The resulting boundary layer was first charac-

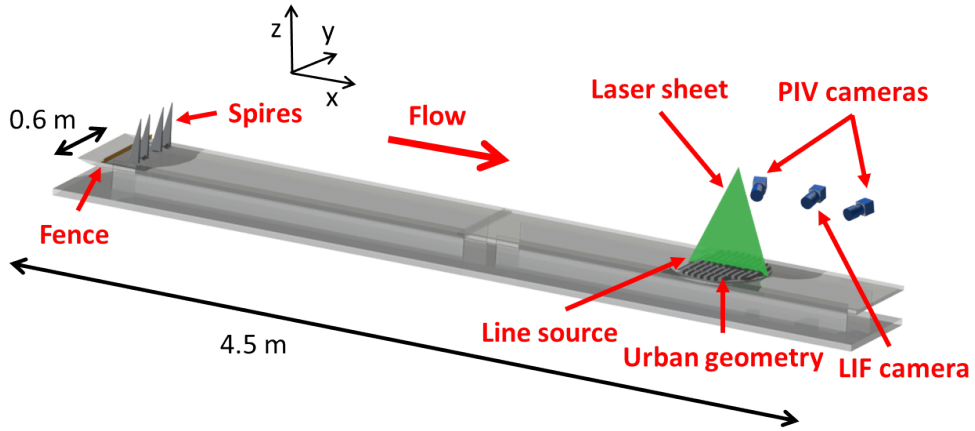

Figure 5.2: Schematic overview of the experimental set-up indicating the different components.

terized without the urban model by means of a planar PIV measurement in the $y = 0$ plane, which is the symmetry plane in the middle of the plate.

The urban model was placed approximately 3.9 m downstream of the spires. It was made from PMMA blocks with cross-sectional dimensions of 2.0×2.0 cm^2 and lengths of 2.0, 10.0, and 16.0 cm for cases AR1, AR5, and AR8, respectively. The model contained eight street canyons in streamwise direction. Based on initial results from LES simulations (Tomas et al., 2016b), this was deemed to be sufficient to capture the flow development up to the region where the flow in the street canyons becomes similar.

To perform simultaneous velocity and concentration measurements above and partly inside the canopy, a stereoscopic PIV set-up was combined with a planar LIF set-up, as shown in Fig. 5.2. For the stereoscopic PIV measurements, the flow was seeded with 10 μm diameter neutrally buoyant tracer particles (Sphericell). The $y = 0$ plane was illuminated with a twin-cavity double pulsed Nd:YAG laser (Spectra-Physics Quanta Ray), resulting in a field of view of approximately 430×250 mm^2 ($x \times z$). Dedicated optics were used to form a thin laser sheet with a thickness of approximately 1 mm in the measurement area. The particle images were recorded using two high resolution CCD cameras with a 4872×3248 pixel format (Image LX 16M, LaVision). Both PIV cameras were equipped with Micro-Nikkor F105mm objectives with an aperture number $f_\# = 8$. Additionally, both cameras were equipped with Scheimpflug adapters (Prasad and Jensen, 1995) to allow for large viewing angles while keeping the particle images in focus. The total separation angle between the PIV cameras was set to 56°. To enable measurements partly inside the canopy, both cameras had a small vertical inclination of about 10°. A third camera (Image LX 16M, LaVision) was added to perform the planar LIF measurements. This camera was also equipped with a Micro-Nikkor F105mm objective with an aperture set to $f_\# = 2.8$.

A lower aperture number was chosen to collect a larger amount of the fluorescent signal. To provide a better view into the canopy this camera had a slight vertical inclination of 10°, thereby eliminating the need for a Scheimpflug adapter. In order to separate the scattered light by the tracer particles (PIV) and the fluorescent signal (LIF), shortpass optical filters (PIV cameras) and a longpass optical filter (LIF camera) were employed (Westerweel et al., 2009).

5.2.2.2 *PIV Measurements*

Data acquisition, image calibration, and analysis of the PIV images was performed using the commercial software package Davis 8.3. A custom-made calibration target was used to digitally backproject the distorted PIV images to remove the perspective deformation in stereoscopic viewing. The PIV images were interrogated with a multi-pass interrogation technique, where the final interrogation windows had a size of 24×24 pixels, corresponding to a spatial resolution of $0.1h$, with 75% overlap between the neighbouring windows. The fraction of spurious vectors was found to be less than 2%. These could be reliably detected using a median test (Westerweel and Scarano, 2005) and replaced by linear interpolation. Each dataset consisted of at least 1,500 instantaneous velocity/concentration fields acquired at a temporal resolution of 1.44 Hz. This low acquisition frequency ensured that subsequent samples could be considered as statistically uncorrelated. As a result, reliable and accurate first- and second-order statistics could be obtained.

5.2.2.3 *LIF Measurements*

As the laser operated at a frequency-doubled wavelength of 532 nm, Rhodamine WT (Rh-WT) was selected as the fluorescent dye. This dye has spectral characteristics similar to the more commonly used Rhodamine B (Rh-B). However, it is much less toxic (Crimaldi, 2008). Although Rh-WT is a temperature sensitive fluorescent tracer (Smart and Laidlaw, 1977), the effect of temperature variations was negligible, because the water temperature varied by less than 1°C. The Schmidt number ($\mathrm{Sc} = \nu/D$, where ν is the kinematic viscosity and D is the mass diffusivity) of Rh-WT in the experiments was approximately 2.5×10^3. Furthermore, the effective resolution of the concentration fields was $0.004h$ in both directions. The dye was injected $2h$ upstream of the first row of obstacles as a uniform line source, that consisted of a porous metal plate with size 1.0×40.0 cm^2 ($l_x \times l_y$), which was mounted flush with the ground plate. A concentrated solution Rh-WT (10 mg/L) was injected at a constant flow rate of 3 ml/s by means of a syringe pump system, that resulted in an average vertical injection velocity of about 0.75 mm/s or $3 \times 10^{-3}\, U_\infty$, where U_∞ is the freestream velocity.

Calibration of the LIF images, i.e. the conversion of raw digital images to concentration fields, was done by placing in the measurement domain a small Plexiglas container, with a $45.0 \times 12.0 \times 4.0$ cm^3 size, with different known uniform concentrations. This yielded a calibration curve for measured pixel grey values to concentrations for each pixel in the measurement domain. Care was taken to perform all experiments

under so-called 'optically thin' conditions. Accordingly, the attenuation of the laser sheet due to the presence of Rh-WT was negligible, and the conversion of raw images to concentration fields simplified significantly (Crimaldi, 2008; Krug et al., 2014). The raw images were converted to a concentration field after subtraction of a background image based on linearly interpolating the background image that was taken before and after each measurement to account for the increase in background levels due to the dye introduced during each measurement. In addition, a rescaling procedure was applied to compensate for the pulse-to-pulse variations (with a standard deviation of about 3% of the mean intensity) that are inherently present in the laser beam of the Nd:YAG laser. Finally, the concentration fluxes are obtained by interpolating the velocity field onto the high resolution LIF grid by bicubic interpolation.

5.2.3 *Numerical Set-up*

The set-up of the LES is the same as in Tomas et al. (2016b) except that in the current study only neutrally buoyant conditions are considered and that several obstacle aspect ratios are studied. Here, the main characteristics of the simulations are given, while further details can be found in Tomas et al. (2016b).

5.2.3.1 *Governing Equations and Numerical Method*

The filtered continuity equation and the filtered Navier-Stokes equations for incompressible flow are

$$\frac{\partial \widetilde{u}_i}{\partial x_i} = 0, \tag{5.1}$$

$$\frac{\partial \widetilde{u}_i}{\partial t} = -\frac{\partial}{\partial x_j}\left(\widetilde{u}_i \widetilde{u}_j\right) - \frac{\partial}{\partial x_i}\left(\frac{\widetilde{p} + \tau_{kk}/3}{\rho}\right) + \nu \frac{\partial^2 \widetilde{u}_i}{\partial x_j^2} + \frac{\partial}{\partial x_j}\left(2\nu_{sgs}\widetilde{S}_{ij}\right), \tag{5.2}$$

$$\frac{\partial \widetilde{c^*}}{\partial t} = -\frac{\partial}{\partial x_j}\left(\widetilde{c^*}\widetilde{u}_j\right) + \frac{\nu}{\mathrm{Sc}}\frac{\partial^2 \widetilde{\varphi}}{\partial x_j^2} + \frac{\partial}{\partial x_j}\left(\frac{\nu_{sgs}}{\mathrm{Sc}_{sgs}}\frac{\partial \widetilde{c^*}}{\partial x_j}\right) + \mathcal{S}, \tag{5.3}$$

where $\widetilde{(..)}$ denotes filtered quantities, $\left(\widetilde{p} + \tau_{kk}/3\right)/\rho$ is the modified pressure, τ_{kk} is the trace of the subgrid-scale (SGS) stress tensor, ν is the fluid kinematic viscosity, ν_{sgs} is the SGS viscosity, Sc_{sgs} is the SGS Schmidt number, $\widetilde{S}_{ij} = \frac{1}{2}\left(\partial \widetilde{u}_i/\partial x_j + \partial \widetilde{u}_j/\partial x_i\right)$ is the rate of strain tensor, and $\mathcal{S}$ is a source term. The eddy-viscosity SGS model, $\tau_{ij}/\rho = \widetilde{u_i u_j} - \widetilde{u}_i\widetilde{u}_j = -2\nu_{sgs}\widetilde{S}_{ij}$, where τ is the SGS stress tensor, is already incorporated in Eqs. 5.2 and 5.3. In contrast to the LES in Tomas et al. (2016b) no buoyancy force is applied because neutrally buoyant conditions are considered. Equation 5.3 describes the transport equation for the pollutant concentration c^*. Hereafter the $\widetilde{(..)}$ symbol is omitted for clarity, while the $\overline{(..)}$ symbol represents temporal averaging, and the $\overline{\langle..\rangle}$ symbol represents spatial averaging.

The code developed for this study is based on the Dutch Atmospheric Large-Eddy Simulation (DALES) code (Heus et al., 2010), where the main modifications are the addition of an immersed boundary method (Pourquie et al., 2009), the implementation of inflow/outflow boundary conditions and the application of the eddy-viscosity SGS model of Vreman (2004). This model has the advantage over the standard Smagorinsky-Lilly model (Smagorinsky, 1963; Lilly, 1962) that no wall-damping is required to reduce the SGS energy near walls. The equations of motion are solved using second-order central differencing for the spatial derivatives and an explicit third-order Runge-Kutta method for time integration. For the scalar concentration field the second-order central κ scheme is used to ensure monotonicity (Hundsdorfer et al., 1995). The simulations are wall-resolved, so no use is made of wall functions. The Schmidt number Sc was 0.71, and Sc_{sgs} was set to 0.9, equal to the turbulent Prandtl number found in the major part of the turbulent boundary layer in direct numerical simulation (DNS) studies by Jonker et al. (2013). The code has been used previously to simulate turbulent flow over a surface-mounted fence, showing good agreement with experimental data (Tomas et al., 2015a,c).

5.2.3.2 *Domain and Boundary Conditions*

Figure 5.1 shows the LES domain in blue together with the applied number of grid cells in each direction. At the ground and the obstacle walls no-slip conditions were applied. The velocity and the concentration fields were assumed to be periodic in the spanwise direction. Furthermore, the smooth-wall turbulent boundary layer imposed at the inlet was generated in a separate 'driver' simulation using the rescaling method proposed by Lund et al. (1998). At the outlet a convective outflow boundary conditions was applied for both velocity and concentration. Furthermore, at the top wall free-slip conditions were assumed for the horizontal velocity components. In addition, a small vertical outflow velocity was applied that corresponds to the outflow velocity used in the driver simulation to achieve a zero pressure-gradient boundary layer. The computational grid, boundary conditions, as well as the inflow turbulent boundary layer are the same as for the neutrally buoyant case described by Tomas et al. (2016b), in which further details are given.

5.2.3.3 *Statistics*

The simulations with a turbulent inflow started from a statistically steady solution generated with a steady mean inflow profile. A constant timestep of $0.0156T$ was used, where $T = h/U_h$ and U_h is a velocity scale defined in the next section. The simulations ran for at least $780T$ before statistics were computed, which was long enough to assure a steady state. Statistics were computed for a duration of at least $780T$ with a sampling interval of $0.31T$ resulting in converged results. This duration corresponds to approximately 125 uncorrelated samples in the experiment. The simulations were well-resolved, such that the average subgrid stress $\overline{-2\nu_{sgs}S_{13}}$ did not exceed 6% of the total Reynolds stress, as shown by Tomas et al. (2016b). Therefore, only the resolved statistics are shown in the subsequent sections.

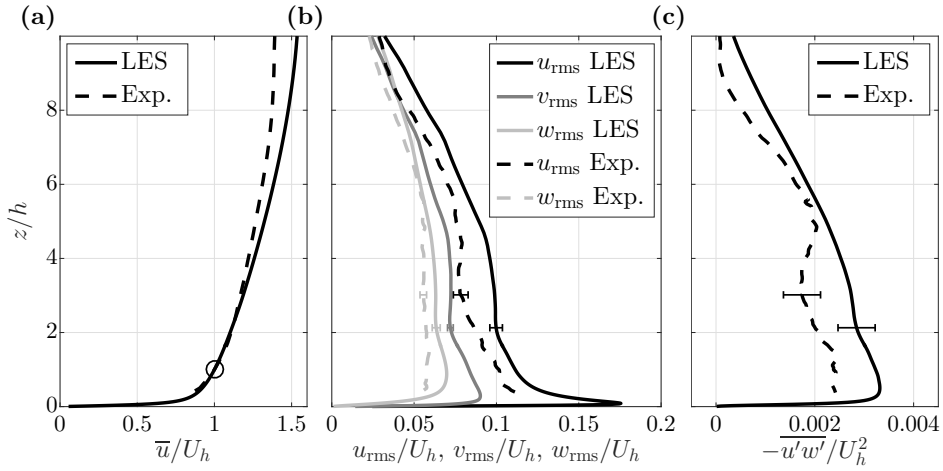

Figure 5.3: Properties of the approaching flow: Mean velocity $\overline{u}$ (a), RMS of the fluctuating velocity components (b), and Reynolds stress $-\overline{u'w'}$ (c). The circle indicates $U_h \equiv \overline{u}|_{z=h}$. The errorbars represent the statistical mean $\pm$ the standard error of the mean.

5.3 RESULTS — FLOW STATISTICS

5.3.1 *Approaching Flow Conditions*

The characteristics of the approaching flow boundary layer are of influence on the flow development over obstacles (Castro, 1979; Blackman et al., 2015). Therefore, in this section a comparison is given of the approaching flow boundary layer in the experiments and in the simulations. All profiles are normalized with the velocity at obstacle height, $U_h \equiv \overline{u}|_{z=h}$, which proved to be the best scaling for the rural-to-urban flows discussed in the subsequent sections.

Figure 5.3 depicts the velocity profile, the profiles of the root mean square (RMS) of the velocity fluctuations, and the mean Reynolds stress distribution in the vertical direction for the experiments and the LES. Despite the different ways of generating the approaching boundary layer there is a satisfactory agreement between the results of the two methods; a good match is found for the mean velocity profile in the range $0 \leq z/h \leq 3$ (Fig. 5.3a). In the LES a zero pressure-gradient boundary layer was generated, while in the experiment a slightly favourable pressure gradient was present due to the boundary-layer growth and the constant cross-sectional area of the tunnel. With the normalization with U_h this difference is reflected in a lower streamwise velocity in the outer region (above $z/h = 3$) of the experimental boundary layer. As observed in Fig. 5.3b the profiles of u_{rms} and w_{rms} are similar in shape when comparing the experimental data with the LES simulations. The magnitude of the velocity fluctuations is smaller in the experimental data set, which is in accordance with experimental results for boundary layers with a slightly favourable pressure gradient

(Joshi et al., 2014). Furthermore, a reduction is observed in the mean Reynolds stress in the experiments in the region $2 \leq z/h \leq 5$, see Fig. 5.3c. This is most likely attributed to the design and the arrangement of the spires. Nevertheless, as will be shown in the subsequent sections, the differences in characteristics of the approaching flow did not cause significant discrepancies in the development of the flow over the urban canopy.

The Reynolds number (Re) based on U_∞ and h was around 5.0×10^3 for both the numerical simulations and the experiments, which is in the regime where Reynolds number effects are small when flow over sharp-edged obstacles is considered (Cheng and Castro, 2002b). In addition, the wall-friction Reynolds number (h^+), based on u_τ and h, was around 200 in both cases, which is in the fully rough regime (Raupach et al., 1991). A summary of the relevant boundary-layer properties for both the experiments and the simulations can be found in Table 5.1.

Table 5.1: Summary of the properties of the approaching boundary layer; δ_1 is the displacement thickness, δ_2 is the momentum thickness, and H is the shape factor.

	$\frac{\delta_{99}}{h}$	$\frac{\delta_2}{h}$	$\frac{\delta_1}{h}$	H $\left(\frac{\delta_1}{\delta_2}\right)$	$\frac{U_\infty}{U_h}$	$\frac{u_\tau}{U_h}$	Re_τ $\left(\frac{u_\tau \delta_{99}}{\nu}\right)$	h^+ $\left(\frac{u_\tau h}{\nu}\right)$	Re $\left(\frac{U_\infty h}{\nu}\right)$
Exp.	9.6	0.95	1.46	1.56	1.41	0.060	2.0×10^3	213	5.4×10^3
LES	10.3	1.28	1.78	1.39	1.56	0.059	2.0×10^3	194	5.0×10^3

5.3.2 *The Flow over the Urban Canopy*

In this section the acquired rural-to-urban flow fields are compared for the first eight streets in the $y = 0$ plane, see Fig. 5.1. All velocity statistics are normalized with the undisturbed velocity at obstacle height U_h. A snapshot of the spanwise velocity component is shown in Fig. 5.4 for case AR5 for both the experiment and the simulation. The results show similar large turbulent structures arising from the top of the obstacles, that grow in downstream direction and that have a larger magnitude than the velocity fluctuations in the approaching flow. Figure 5.5 visualizes the effect of the roughness transition on the mean flow. It shows the contour plots of the mean streamwise velocity component $\overline{u}$ as well as the mean vertical velocity component $\overline{w}$ for case AR5. As the results were averaged over a duration of the order of $10^3 T$, the statistics were converged to within a few percent. The differences in $\overline{u}$ and $\overline{w}$ between the simulations and the experiments are mostly smaller, indicating that the agreement is very good. The only significant difference is the size of the mean recirculation areas at the top of the first three rows of obstacles. The LES predicts a negative vertical velocity close to the downstream walls of the first two street canyons, while

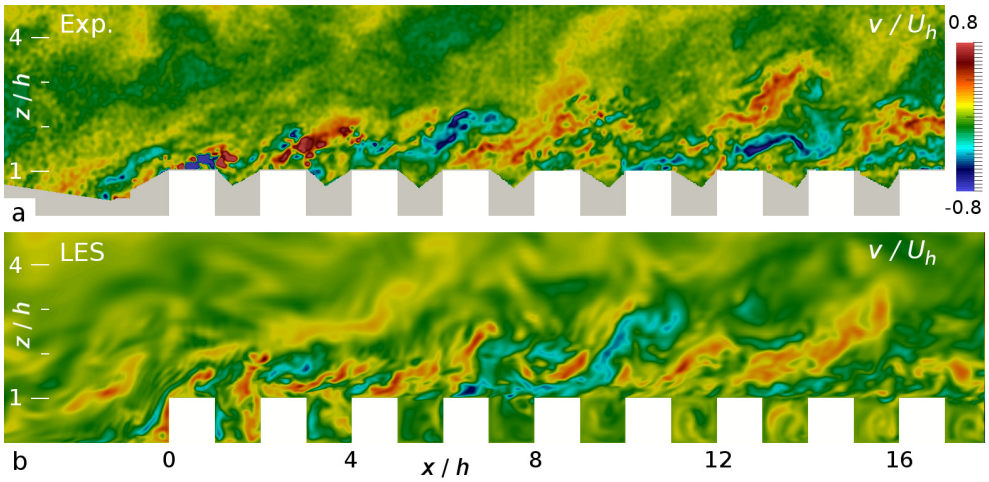

Figure 5.4: Contours of instantaneous spanwise velocity component v/U_h in the midplane of case AR5; (a) experiment and (b) simulation. Areas that could not be illuminated or seen in the experiments have been masked in grey and the obstacles are shown in white.

in the experiment the flow is solely directed out of the street canyons. This difference can be caused by a limitation of the employed methods; especially at the top of the first obstacle the PIV/LIF results should be interpreted with care, because due to high spatial gradients of the velocity and reflections from the obstacle, the PIV results in this region are prone to errors. In this region, too, the numerical errors in the LES can be expected to be largest due to the high velocity near the singularity at the obstacle corners and the large change in velocity gradients. However, these differences could also be purely physical, since the slightly different turbulence characteristics in the approaching flow (see Sect. 5.3.1) can influence the development of the shear layer emanating from the first obstacle (Castro, 1979; Blackman et al., 2015). Nevertheless, downstream of the third row the results of the two methods are nearly indistinguishable.

Figure 5.6 shows the mean Reynolds stresses $\overline{u'u'}$ and $-\overline{u'w'}$ for the same case. The strong shear layer emanating from the upstream corner of the first obstacle generates large turbulent fluctuations resulting in a peak in $\overline{u'u'}$ above the first obstacle and a peak in $-\overline{u'w'}$ above the first street canyon. The flow appears to be also strongly affected by the presence of the second obstacle, above which another peak in $\overline{u'u'}$ is present, while a peak in $-\overline{u'w'}$ is located above the second street canyon. The intensity of the turbulent plume decreases in downstream direction, while weaker plumes of $-\overline{u'w'}$ are produced by the shear layers above the street canyons. Just as for $\overline{u}$ and $\overline{w}$ there are some discrepancies between the experiments and the simulations above the first three obstacle rows due to the aforementioned reasons. The contour plots in Fig. 5.5 and Fig. 5.6 give an overall view of the flow and can be used for a qualitative comparison of the two methods. Figure 5.7 allows for a quantitative

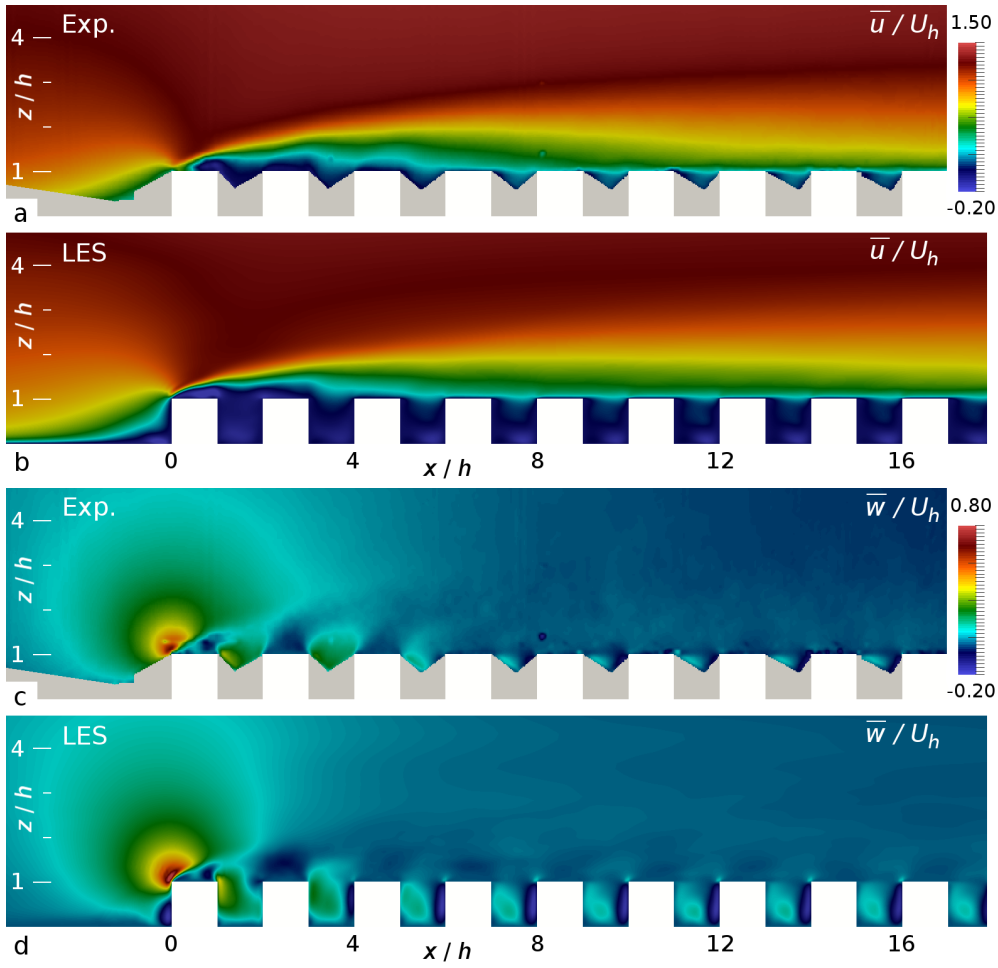

Figure 5.5: Contours of mean streamwise velocity component $\overline{u}/U_h$ (a, b) and mean vertical velocity component $\overline{w}/U_h$ (c, d) in the midplane of case AR5; experiment (a, c) and simulation (b, d). Areas that could not be illuminated or seen in the experiments have been masked in grey and the obstacles are shown in white.

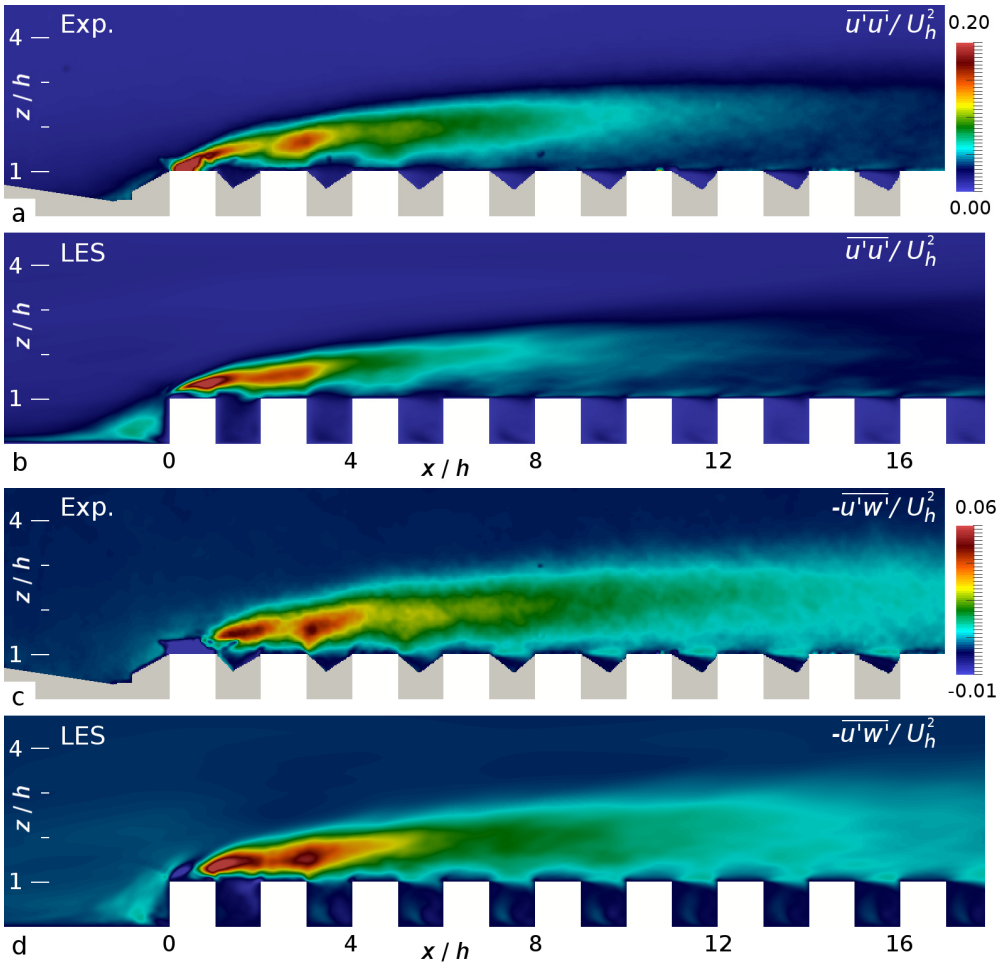

Figure 5.6: Contours of $\overline{u'u'}/U_h^2$ (a, b) and $\overline{u'w'}/U_h^2$ (c, d) in the midplane of case AR5; experiment (a, c) and simulation (b, d). Areas that could not be illuminated or seen in the experiments have been masked in grey and the obstacles are shown in white.

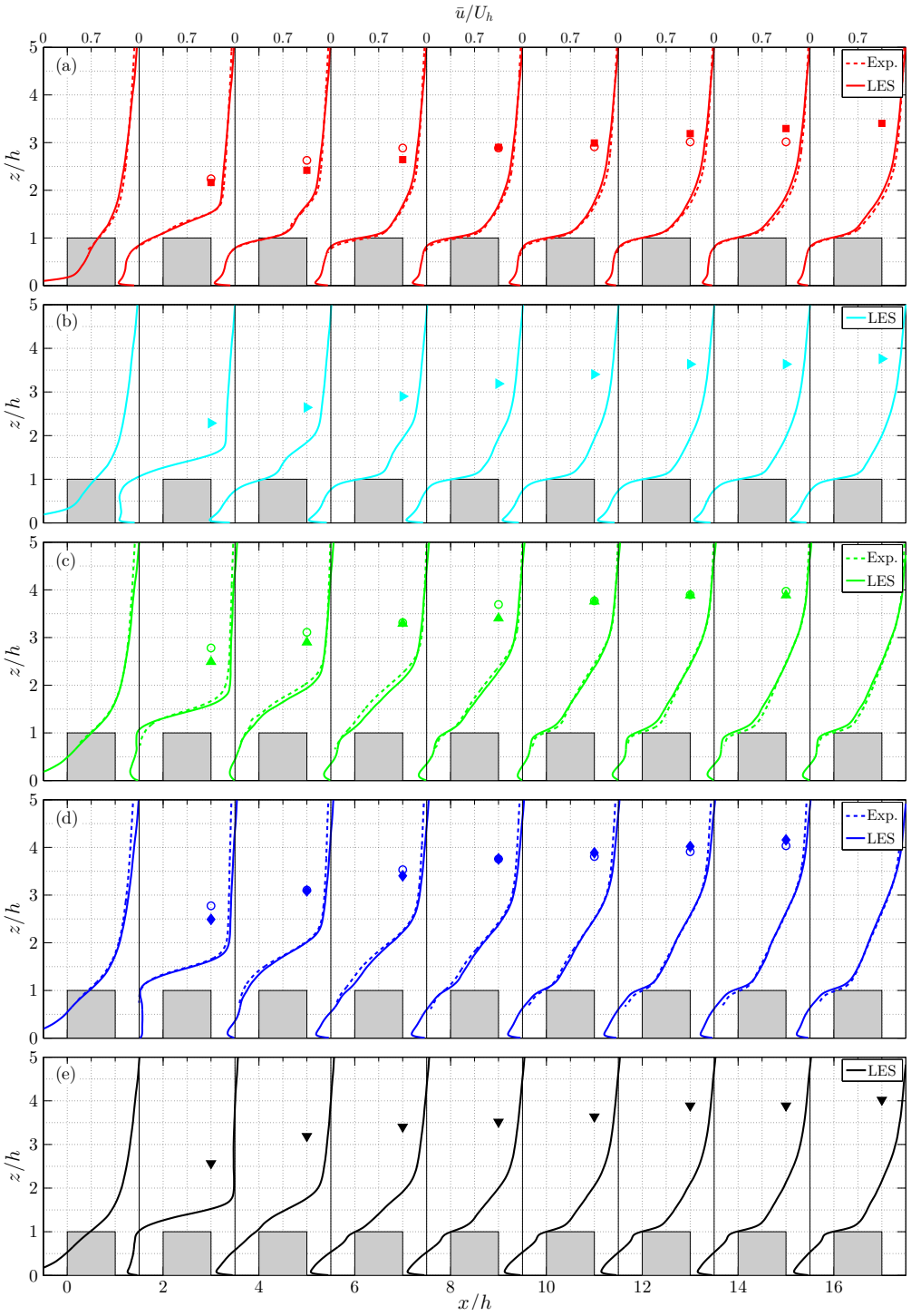

Figure 5.7: Profiles of mean streamwise velocity component $\overline{u}/U_{l_t}$ in the middle of each street canyon for cases AR1 (a), AR2 (b), AR5 (c), AR8 (d), and 2D (e). The internal boundary-layer depth, δ_i, is shown by solid markers for the LES and by open markers for the experiment (if available).

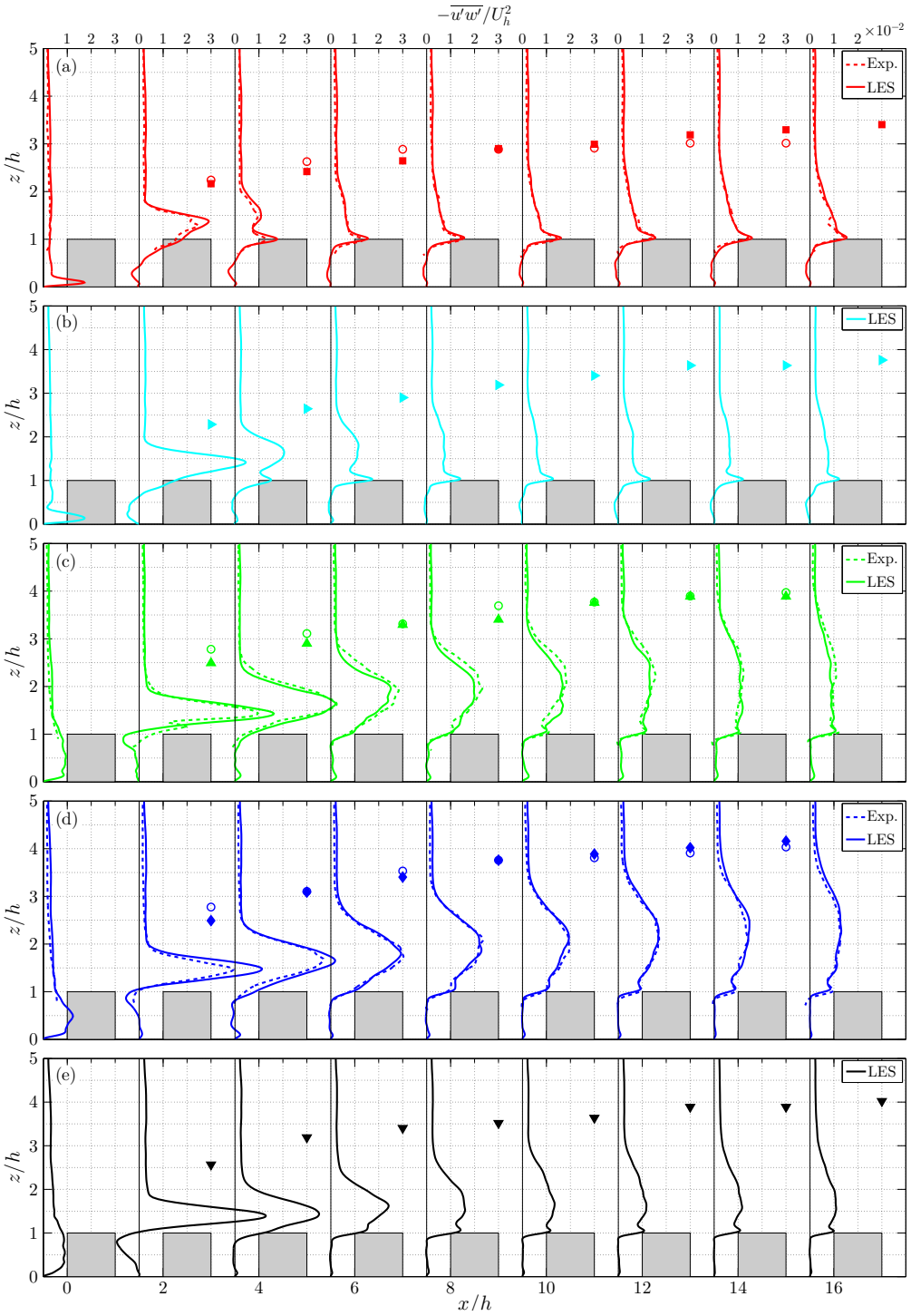

Figure 5.8: Profiles of mean Reynolds stress $-\overline{u'w'}/U_h^2$ in the middle of each street canyon for cases AR1 (a), AR2 (b), AR5 (c), AR8 (d), and 2D (e). The internal boundary-layer depth, δ_i, is shown by solid markers for the LES and by open markers for the experiment (if available).

comparison of cases AR1, AR2, AR5, AR8, and 2D, by showing the vertical profiles of the mean streamwise velocity component $0.5h$ in front of the first obstacle row and in the middle of each subsequent street canyon. The LES data are shown by continuous lines, while, if available, the experimental data are shown by dashed lines. In all cases backflow occured inside the canopy, while above the canopy an internal boundary layer developed, which is defined and discussed in Sect. 5.3.3 and shown in Fig. 5.7 by open symbols for the experiment and by solid symbols for the LES. In all cases the flow profiles in the street canyon change significantly over the first three to four rows of obstacles, while only minor changes are observed from street canyon 4 onwards. For case AR1, and especialy case AR2, $\overline{u}$ is mostly negative at this location in the street canyon, while for cases AR5, AR8, and 2D a 'canyon vortex' arises that is most apparent in case 2D.

Figure 5.8 shows the profiles of the mean Reynolds stress $-\overline{u'w'}$ at the same locations. The differences between the LES and the experiments are minor with the maximum differences occurring in the region with large gradients just above the canopy in the first street canyon. In this region the finite resolution of the PIV acts as a lowpass filter, which results in an underestimation of the peak value of the Reynolds stresses. The fraction of resolved Reynolds stresses can be estimated from the ratio between the PIV resolution and the length scale Λ of the dominating flow structures (Scarano, 2003). Λ is estimated using the distance required for the streamwise two-point correlation of u to decrease to 0.5. Above the first street canyon in case AR8 (Fig. 5.7d) Λ is $0.3h$, resulting in approximately 83% of the Reynolds stress being resolved at that location.

With increasing aspect ratio l/h the blockage of the incoming flow increases, which results in an increase of the peak in $-\overline{u'w'}$ behind the first row of obstacles. Further downstream this peak diffuses and eventually the largest value of $-\overline{u'w'}$ occurs near the top of the canopy, where the rooftop shear layers are the largest sources of turbulence production. In view of blockage of the flow case AR8 approximates the 2D case, which is reflected in a similar peak in $-\overline{u'w'}$ behind the first row. However, in the eighth street canyon the depth of the region with increased Reynolds stress is larger for case AR8 than case 2D. This is because the three-dimensional roughness arrays (all cases other than 2D) induce a secondary flow that causes the internal boundary layer to grow more rapidly in case AR8 than in case 2D. This is further discussed in Sect. 5.3.3.

Furthermore, since the Reynolds stress induced by the first row of obstacles is more than ten times larger than the Reynolds stress in the approaching flow boundary layer, the influence of the slight difference in approaching flow characteristics between experiments and simulations is marginal.

5.3.3 *Surface Forces and Internal Boundary Layer Growth*

To investigate the effect of the roughness transition on the boundary layer the change in drag is quantified by considering the total drag force for each street area A_{street},

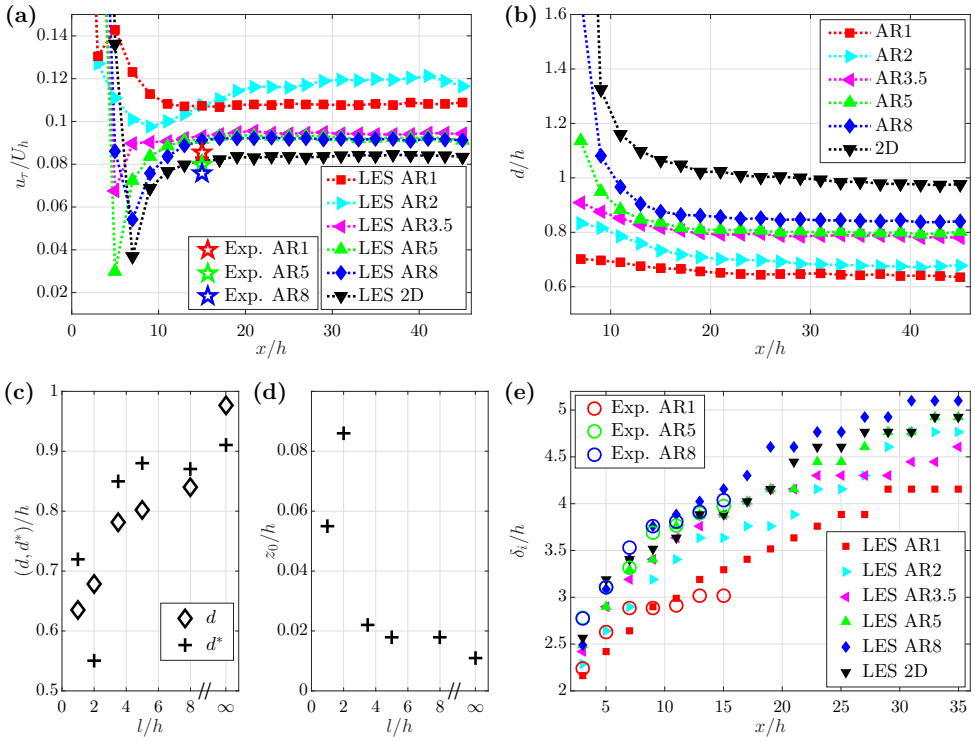

Figure 5.9: Surface drag and resulting internal boundary layer; (a) mean street-averaged friction velocity u_τ, (b) mean street-averaged displacement height d (LES only), (c) fully-developed d and zero-plane displacement height d^* found by fitting with the logarithmic velocity profile (LES only), (d) roughness length z_0 found by fitting with the logarithmic velocity profile (LES only), (e) internal boundary-layer depth δ_i.

which has a length of $2h$ and a width equal to the domain size. The total drag force consists of skin frictional drag, F_τ, and form drag, F_p;

$$F_\tau = \int_{A_s} \overline{\tau}\, dA, \tag{5.4}$$

$$F_p = \int_{A_f} \Delta\overline{p}\, dA, \tag{5.5}$$

where $\overline{\tau} = \rho\nu\left(\partial\overline{u}/\partial n\right)_0$ is the mean wall shear stress, ρ is the fluid density, A_s is the total area of all surfaces in each street (i.e. the top and side faces of the obstacles as well as the ground surface), $\Delta\overline{p}$ is the mean pressure difference between upwind and downwind faces of the obstacles, and A_f is the frontal area of the obstacles in each street. At the 23rd street F_p constituted around 75% of the total drag, which means the viscous drag cannot be neglected at this Reynolds number. In Fig. 5.9a the streamwise development of the total drag is shown for the simulations in the form of the friction velocity $u_\tau = \left[\left(F_\tau + F_p\right) / \left(\rho A_{\text{street}}\right)\right]^{1/2}$. In the experiments the forces on the obstacles and on the ground plate were not measured, so u_τ could not be computed. In fully-developed conditions and under the assumption that the viscous drag is negligible, u_τ can be estimated from the spatially-averaged value of $\overline{u'w'}$ near the top of the canopy (Cheng and Castro, 2002b). For the LES results this method indeed approximates the form drag contribution to u_τ to within 4% when the last street (23rd) is considered. For the experimental results $\overline{u'w'}$ is only available in the midplane and up to the eighth street. The estimation $u_\tau \approx (-\langle\overline{u'w'}\rangle)^{1/2}$, where $\langle\overline{u'w'}\rangle$ is the streamwise-averaged Reynolds stress near the top of the obstacles, is shown in Fig. 5.9a by the red, blue, and green ☆ symbols for case AR1, AR5, and AR8, respectively. The difference of approximately 20 % compared to the LES results is mainly attributed to not taking into account the viscous contribution. However, spanwise variations in $-\overline{u'w'}$ are also a possible source of discrepancy, as will be discussed later. Figure 5.9b shows the streamwise development of the displacement height d, which is the height at which the total drag force acts (Jackson, 1981). It is computed by dividing the total moment of the drag forces by the total drag force. After approximately nine streets d has reached a constant value, where the cases with highest blockage need longest distance to adapt. Moreover, it can be seen that with increasing l/h, d increases to the expected maximum of h for case 2D.

Flows over rough surfaces are commonly parameterized using the logarithmic velocity profile

$$\overline{u} = \frac{u_\tau}{\kappa}\ln\left(\frac{z-d^*}{z_0}\right), \tag{5.6}$$

where κ is the von Kármán constant ($\kappa = 0.4$), z_0 is the roughness length, and d^* is the displacement height, which is written with the superscript * to show that it differs from d; both d^* and z_0 are found by fitting the velocity profile from the LES to Eq. 5.6, while d follows directly from the force balance. In Fig. 5.9c both d and d^*

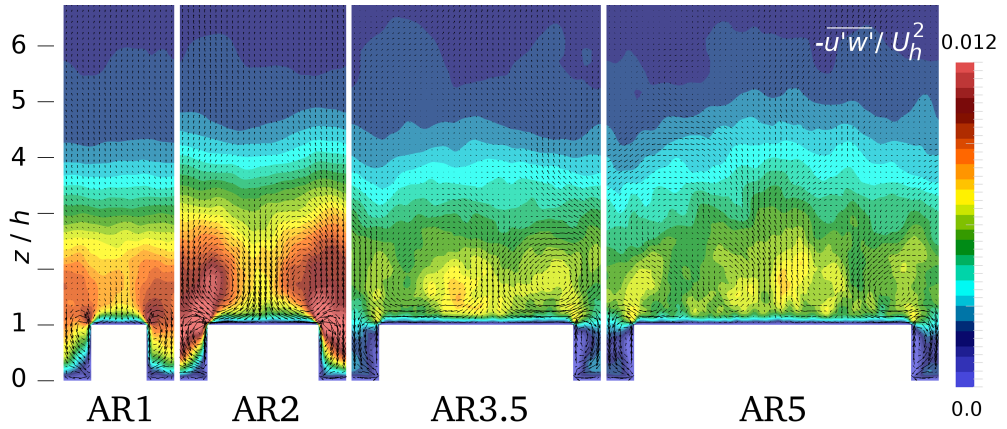

Figure 5.10: Visualization of secondary flow by mean velocity vectors in the $y-z$ plane at $x/h = 44.5$ (the upstream side of street 23) for cases AR1, AR2, AR3.5, and AR5. The contours show the mean resolved Reynolds stress $-\overline{u'w'}/U_h^2$.

are plotted for the 23rd street for all cases, showing a discrepancy that has also been reported by Cheng and Castro (2002b) and Cheng et al. (2007). They suggest that this difference arises from significant dispersive stresses within the canopy, which is confirmed by a DNS investigation by Coceal et al. (2006). Figure 5.9d shows z_0 for all cases at the same location from which it can be concluded that, except for case AR2, z_0 decreases with increasing aspect ratio, which is in agreement with earlier studies that show that for cubical roughness z_0 decreases for $\lambda \gtrsim 0.2$ (Macdonald et al., 1998). Nevertheless, from Fig. 5.9a,c,d it is clear that case AR2 induces the largest drag force and that, unlike the other cases, this drag force has not yet fully developed. In addition, at the end of the domain the velocity profile for case AR2 showed only a small logarithmic region, most likely because it was still developing.

The effect of the change in surface drag on the mean velocity is shown in Fig. 5.9e, where the internal boundary-layer depth δ_i is given for each street for both the experiments and the simulations. δ_i is found by subtracting the smooth-wall inlet velocity profile from the mean velocity field for the roughness transition: $\Delta\langle\overline{u}\rangle = \langle\overline{u}\rangle_{\mathrm{RT}} - \langle\overline{u}\rangle_{\mathrm{inlet}}$. δ_i is defined as the height at which the vertical gradient of $\Delta\langle\overline{u}\rangle$ reaches zero. The threshold $|\mathrm{d}\Delta\langle\overline{u}\rangle/\mathrm{d}z| < 0.005U_h/h$ was used to determine this location. There is a good match between the experiments and the simulations; initially δ_i grows more rapidly for larger aspect ratios. However, the depth of δ_i does not solely depend on the blockage of the flow; secondary flows generated by the three-dimensional roughness geometry also affect the internal boundary-layer growth. This is indicated by the fact that δ_i is slightly larger for case AR8 than for case 2D, while the blockage of the flow is less. The secondary flow is found in all cases, except case 2D, and starts after the first row of obstacles. It is visualized in Fig. 5.10 by vectors of mean velocity in the plane $x/h = 44.5$ (the upstream side of street 23) for cases AR1, AR2, AR3.5, and AR5. The contours of $-\overline{u'w'}/U_h^2$, plotted in the same figure, show

that the secondary flow influences the distribution of $-\overline{u'w'}$. This spanwise inhomogeneity can reach up to the internal boundary-layer depth depending on the l/h ratio. For all cases the contours show spanwise variations that correspond with the size of the repeating element. Local upwash and downwash regions can be identified. These are of largest magnitude in case AR2, resulting in two counter-rotating streamwise vortices that reach up to $2h$ above the canopy. We hypothesize that the strength of the secondary flow, and thus the increase in drag, is largest when the spanwise spacing of the roughness elements is roughly proportional to $\delta_i - h$. This is analogous to the conclusion by Vanderwel and Ganapathisubramani (2015), who measured a fully-developed boundary layer with a depth of $11.3h$ and find that large-scale secondary flows are accentuated when the spanwise spacing of roughness elements is roughly proportional to the boundary-layer depth. Finally, it must be noted that the presence of large-scale secondary flows requires spatial averaging of $-\overline{u'w'}$ over regions of at least the size of the repeating element in order to derive an accurate estimate of u_τ. The experimental results in Fig. 5.9a are based on a spatial average in the midplane only. Fortunately, as shown in Fig. 5.10, the spanwise varation of $-\overline{u'w'}$ is relatively small for these cases (AR1, AR5, and AR8).

5.4 RESULTS — POLLUTANT DISPERSION

Pollutant dispersion was investigated by considering concentrations of a passive tracer released from a line source $2h$ upstream of the urban canopy. The concentrations c^*, retrieved both from measurements and from simulations, are non-dimensionalized using the reference velocity U_h, obstacle height h, source width l_y, source concentration c_s, and source volume flow rate ϕ_s (see Sect. 5.2.2.3):

$$c = \frac{c^* U_h \, h \, l_y}{c_s \, \phi_s} \tag{5.7}$$

Figure 5.11 shows the contours of c for case AR5 corresponding to the instantaneous velocity field shown in Fig. 5.4. The experimental results exhibit more distinctive layers than the simulations due to the larger Schmidt number (Sc). Nevertheless, there is a high degree of similarity when the larger structures are considered. This is reflected in a turbulent Schmidt number of 1.21 in the experiments and 0.77 in the LES, which was estimated by deriving the turbulent viscosity and the turbulent diffusivity using the 'Boussinesq hypothesis'.

5.4.1 *Mean Concentration Fields*

Figure 5.12a-d shows the vertical distribution of mean concentration starting $0.5h$ upstream of the first row of obstacles and in the middle of each subsequent street canyon for cases AR1, AR5, AR8, and 2D. The LES data are shown by continuous lines, while, if available, the experimental results are shown by the dashed lines. The internal boundary-layer depth δ_i is plotted by solid markers for the LES and by open markers for the experiment. Clearly, the vertical profiles for $\overline{c}$ are largely controlled

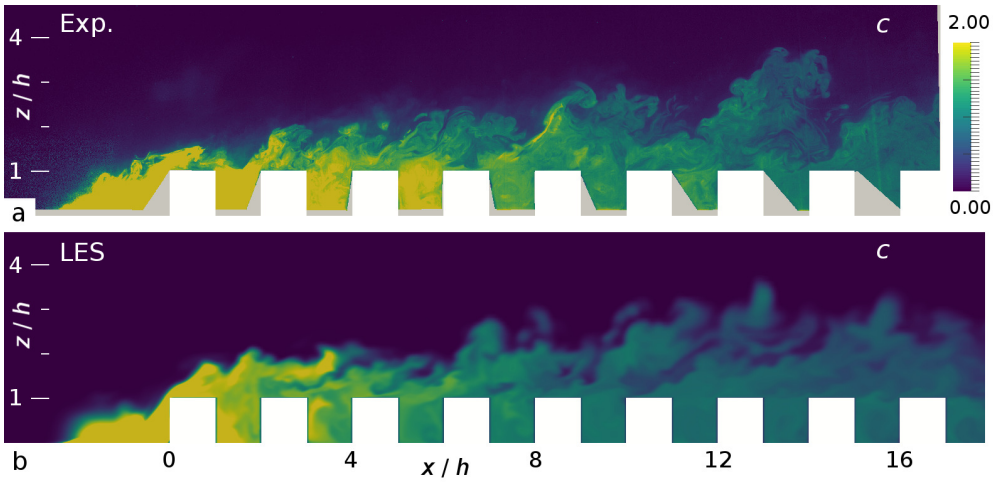

Figure 5.11: Contours of instantaneous concentration c (defined in Eq. 5.7) in the midplane of case AR5; (a) experiment and (b) simulation. The snapshots correspond to the velocity fields shown in Fig. 5.4. Areas that could not be illuminated or seen in the experiments have been masked in grey and the obstacles are shown in white.

by δ_i as high concentrations remain inside the internal boundary layer. The most pronounced differences between the numerical and experimental results are observed inside and just above the street canyons (i.e. $z/h < 1.5$), where the experiments indicate a significantly higher concentration. Additional tests revealed that the line source was slightly non-uniform in spanwise direction with a higher than average flow rate at the location of the measurement plane. Nevertheless, the average flow rate through the line source was kept constant in time. The influence of the spanwise non-uniformity decreases in downstream direction as turbulence decreases this lateral inhomogeneity, leading to a closer match between the two methods farther downstream. This behaviour is also reflected in Fig. 5.12e, where the average street canyon concentration is shown. Since the street canyon is not completely visible in the experimental results, the average street canyon concentration is determined only in the upper part of the street canyon. From the LES results it is concluded that this is a good approximation, as the street canyon concentration is quite uniform (especially in the more downstream street canyons). Considering the different aspect ratios it is clear that cases AR5, AR8, and 2D predict qualitatively similar behaviour: the maximum average concentration occurs in the first street and the average concentration decreases slowly in subsequent streets. Different behaviour is found in the AR1 case, where the street canyon concentration is lower in the first street and subsequently reaches its maximum in the third street canyon. This is because for case AR1 a large part of the concentration is advected with high velocity through the streamwise streets, thereby passing the first two street canyons. As the flow velocity has decreased after two streets, the concentration in the wakes of the cubes increases.

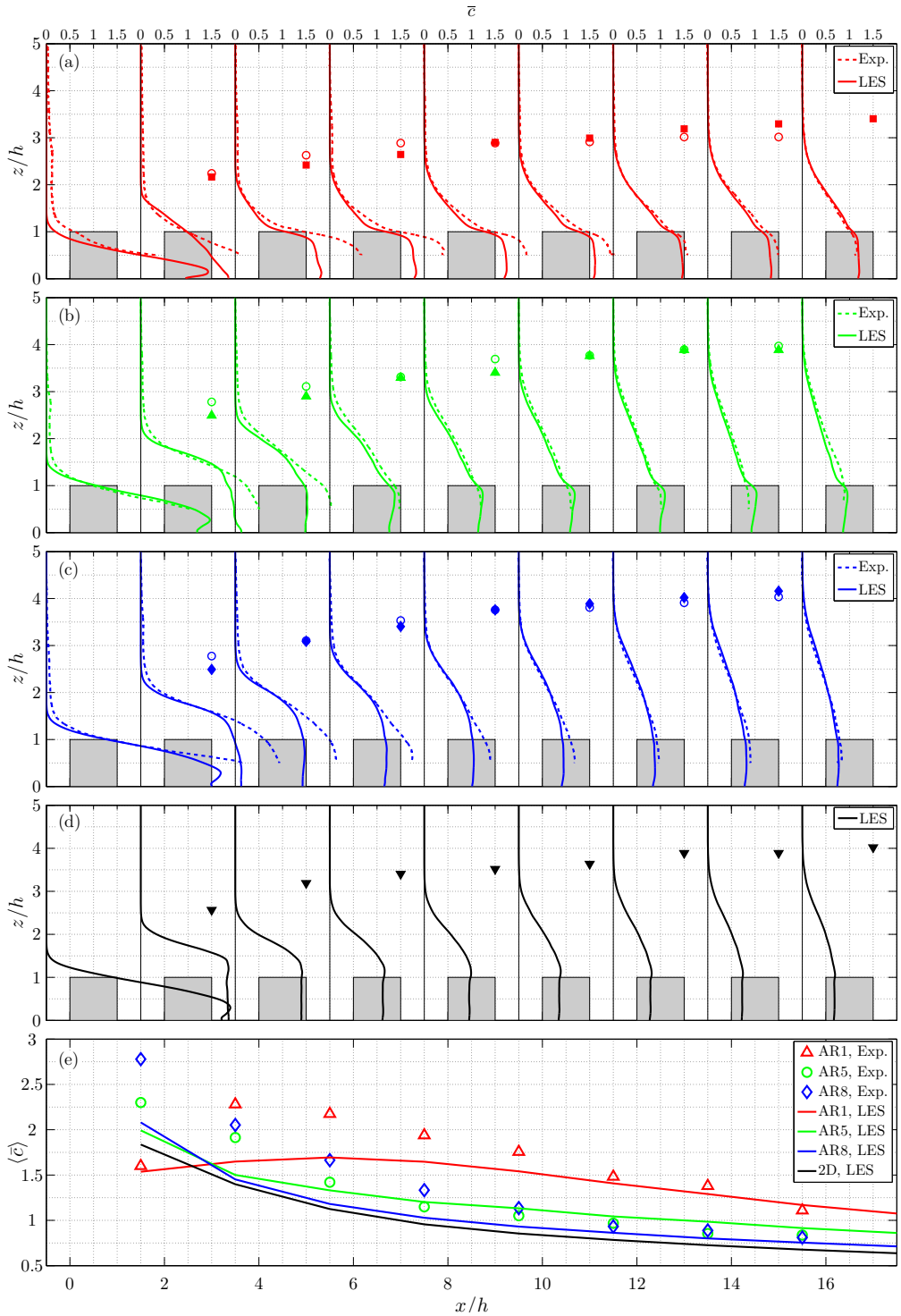

Figure 5.12: Profiles of mean concentration $\overline{c}$ in the middle of each street canyon for cases AR1 (a), AR5 (b), AR8 (c), 2D (d), and spatially-averaged street canyon concentration $\langle\overline{c}\rangle$ (e). In Figures 5.12a-d the internal boundary-layer depth, δ_i, is shown by solid markers for the LES and by open markers for the experiment (if available).

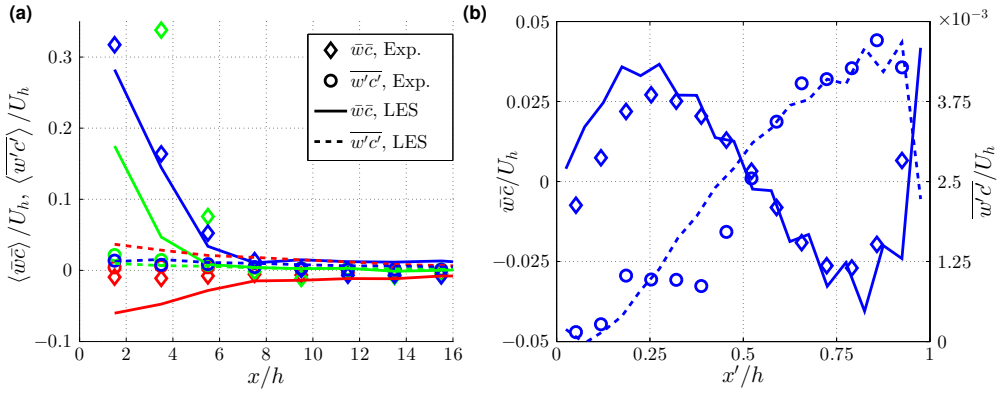

Figure 5.13: Streamwise variation of the advective and turbulent pollutant fluxes for different aspect ratios (a), and spatial variation of advective and turbulent pollutant fluxes for the 5th street of case AR8 (b). Red, green, and blue lines/symbols correspond to case AR1, AR5, and AR8, respectively; $x' = 0$ corresponds to the upstream street canyon wall.

5.4.2 *Pollutant Dispersion Mechanisms*

The geometry of the urban canopy has an influence on the dispersion of pollutants (Belcher, 2005); e.g. in the currently considered geometries pollutants can travel with the mean flow through streamwise streets or above the urban canopy. Sometimes pollutants get trapped inside the wakes of the obstacles and since the considered cases are in the skimming flow regime these wakes form street canyon flows. Pollutants leave the street canyons mostly through the top of the canopy either by being advected with the mean flow or by turbulent velocity fluctuations. Therefore, the average total pollutant flux in the midplane of each street canyon can be separated into an advective and a turbulent contribution:

$$\overbrace{\langle \overline{w}\overline{c} \rangle_{z=h}}^{\text{total}} = \overbrace{\langle \overline{w}\,\overline{c} \rangle_{z=h}}^{\text{advection}} + \overbrace{\langle \overline{w'c'} \rangle_{z=h}}^{\text{turbulence}}, \tag{5.8}$$

where the $\langle .. \rangle|_{z=h}$ symbols represent the average over the region ($0.05 < x'/h < 0.95$, $0.95 < z/h < 1.05$), where $x' = 0$ represents the location of the upstream wall of the street canyon. Figure 5.13a shows the streamwise development of both contributions. Clearly, in the first three streets the advective pollutant flux is significant. Remarkably, case AR1 shows a negative advective pollutant flux both in the experiment and in the LES, in contrast to the spanwise-averaged result (as in Tomas et al. (2016b)). This indicates that the three-dimensionality of the flow causes the advective pollutant flux in the midplane of the obstacles to be opposite to the spanwise-averaged result, which is positive because the mean spanwise-averaged vertical velocity is positive. Furthermore, the experimental and LES results for the average advective flux are approximately the same, except for case AR5, where the experimental res-

ults show a much larger average advective flux from the first three street canyons. This is mostly related to the difference in vertical velocity at these locations (as was discussed in Sect. 5.3.2 and shown in Fig. 5.5) and partly due to the larger mean concentration. Furthermore, Fig. 5.13b shows the spatial distribution of $\overline{w}\,\overline{c}$ and $\overline{w'c'}$ at the top of street 5 of case AR8. The shapes of these profiles are similar from street 4 and onwards. The agreement between the experiment and the LES is good; for the simulation $\overline{w}\,\overline{c}$ shows wiggles that are characteristic for simulations of flow near sharp obstacle corners when using central-differencing for the advection terms in the momentum equations. However, the local values of $\overline{w}$ are relatively small and the agreement with the experiment is satisfactory. It is found that, similar to Michioka et al. (2014), $\overline{w'c'}$ is always positive at the top of the canopy, i.e. turbulence always acts to remove pollutants from the street canyons.

To investigate under which conditions pollutants are ventilated from street canyons, the joint probability density function (JPDF) of streamwise velocity fluctuation u' and instantaneous vertical pollutant flux wc was computed in each street in the region $(0.05 < x'/h < 0.95,\ 0.95 < z/h < 1.05)$, where $x' = 0$ represents the location of the upstream wall of the street canyon. The shape of the JPDF does not vary significantly inside this region. Therefore, the JPDF is averaged over this region and shown for street 6 for cases AR1, AR5, AR8, and 2D in Fig. 5.14, where the JPDF has been multiplied with the associated value of wc to visualize the contribution to the total average pollutant flux $\overline{wc}$. For all cases the pollutant flux wc is mainly negative when $u' > 0$, i.e. pollutants enter the street canyon from above, while for $u' < 0$ the pollutant flux wc can be either positive or negative. It is found that after three streets the JPDFs have the same shape as shown in Fig. 5.14, which suggests the dominating mechanism responsible for pollutant removal has developed after three streets. Accordingly, in (periodic) simulations of fully-developed flow over street canyons qualitatively similar JPDFs are found (Michioka et al., 2014). From the results presented here it can be concluded that ventilation of street canyons is associated with low momentum regions passing the street canyons.

5.4.2.1 *The Mean Fluctuating Velocity Field for Street Canyon Ventilation*

Apart from the knowledge that low momentum regions are responsible for street canyon ventilation, details about the associated flow structure are unknown. Reynolds and Castro (2008) and Michioka et al. (2011) investigated the occurrence of sweeps and ejections in the urban canopy by computing two-point correlations of u. However, the direct correlation between street canyon ventilation and the flow was not made. Here, use is made of linear stochastic estimation (LSE) (Adrian, 1988) to approximate the conditional mean velocity fluctuation for the event of a pollutant flux $\langle wc \rangle_e$ out of the street canyon: $\overline{u_i'(\boldsymbol{x})|\langle wc \rangle_e}$, where $\boldsymbol{x} = (x, y, z)$ and $\langle .. \rangle$ represents the spatial average over the region $(0.05 < x'/h < 0.95,\ 0.95 < z/h < 1.05)$ in

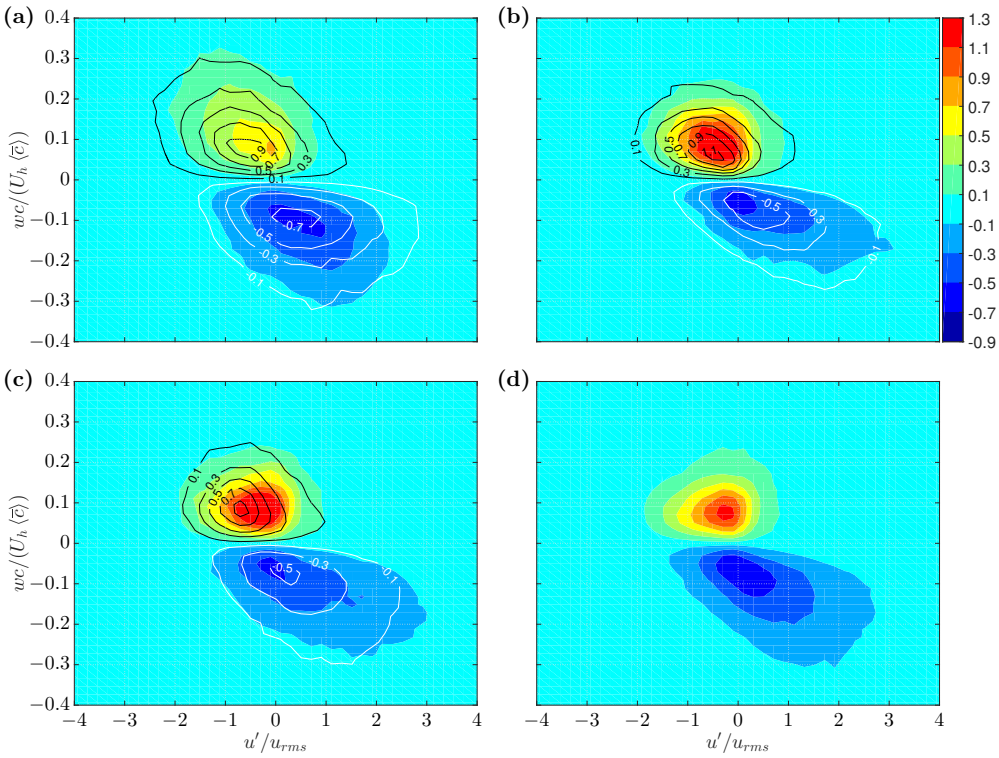

Figure 5.14: Joint probability density function (JPDF) of streamwise velocity fluctuation u' and instantaneous vertical pollutant flux wc multiplied with the associated value of wc; the results are averaged over the region $(0.05 < x'/h < 0.95,\ 0.95 < z/h < 1.05)$ for street 6; (a) AR1 (b) AR5 (c) AR8 (d) 2D; the line contours show the experimental results and the coloured contours show the LES results.

the midplane of the obstacles. Analogously to Christensen and Adrian (2001) this conditional mean is approximated by

$$\overline{u_i'^{\mathrm{e}}} = \overline{u_i'(\boldsymbol{x})|\langle wc\rangle_{\mathrm{e}}} \approx \frac{\overline{\langle wc\rangle u_i'(\boldsymbol{x})}}{\overline{\langle wc\rangle^2}}\langle wc\rangle_{\mathrm{e}}, \tag{5.9}$$

which shows that the mean fluctuating velocity field associated with a given value of $\langle wc\rangle_{\mathrm{e}}$ can be reconstructed using unconditional two-point correlation data. LSE is more practical than the conventional conditional-averaging procedure, because all available samples are used in reconstructing the conditional fluctuating velocity field, so that less samples are required for converged results. As the amplitude of $\overline{u_i'^{\mathrm{e}}}$ depends (linearly) on the chosen magnitude of $\langle wc\rangle_{\mathrm{e}}$ a realistic event is chosen to compare for. Figure 5.14 shows that the event of $\langle wc\rangle_{\mathrm{e}} = 0.1U_h\langle\overline{c}\rangle$ occurs frequently in all considered cases. Therefore, this will be the event for which the considered roughness geometries are compared. Figure 5.15 shows for case AR1 the vector field of the mean fluctuating velocity $\overline{u_i'^{\mathrm{e}}}$ together with contours of $\overline{u'^{\mathrm{e}}}$ found by using Eq. 5.9. The experimental data is shown for street 6, but from street 5 and onwards the structure does not change significantly. Therefore, for the LES the data has been averaged over streets 6 to 21 for statistical convergence. Figure 5.16 shows the same results for case AR8. As expected from the JPDFs, low momentum flow is indeed present above the canopy. The agreement between the results from the experiment and the LES is good; in the proximity of the top of the street canyon the contours are very similar, while the contours further away have a slightly different shape. Nevertheless, both methods predict a flow structure of greater length and height for case AR8 than for case AR1. To indicate the influence of the aspect ratio on the size of these regions the streamwise length scale $\mathcal{L}_x$ and the vertical length scale $\mathcal{L}_z$ of the contour $\overline{u'^{\mathrm{e}}} = -0.04U_h$ are plotted in Fig. 5.17, where $\mathcal{L}_x$ is the length of the contour just above the canopy and $\mathcal{L}_z$ is the maximum height of the contour above the canopy. Using a different value for the contour did not show significantly different behaviour. Figure 5.17 indicates that increasing the aspect ratio mostly affects $\mathcal{L}_z$, which increases linearly. The relative increase is significant, which is evident from Fig. 5.15 and Fig. 5.16. Surprisingly, $\mathcal{L}_z$ is lower for the 2D case. The results for the streamwise length scale $\mathcal{L}_x$ (Fig. 5.17a) do not show a clear trend, because there is less agreement between the experimental and numerical results, and because the relative differences in $\mathcal{L}_x$ are smaller than for $\mathcal{L}_z$. From Fig. 5.17 it can be concluded that the height of the low momentum regions, that pass over the urban canopy during street canyon ventilation, increases with increasing aspect ratio of the obstacles.

Fig. 5.15 and Fig. 5.16 illustrate the average instantaneous flow field associated with street canyon ventilation in the $y = 0$ plane, but what happens inside the urban canopy during such an event? From the simulations $\overline{u_i'^{\mathrm{e}}}$ can also be retrieved in the horizontal plane in the urban canopy, which is shown in Fig. 5.18 for the plane $z/h = 0.5$. Although the contours of $\overline{u'^{\mathrm{e}}}$ in Fig. 5.15 and Fig. 5.16 indicate that the correlation of $\overline{u'^{\mathrm{e}}}$ with $\langle wc\rangle_{\mathrm{e}}$ decreases significantly when considering locations inside the street canyon, $\overline{w'^{\mathrm{e}}}$ inside the street canyon does correlate with $\langle wc\rangle_{\mathrm{e}}$ (as is evident from

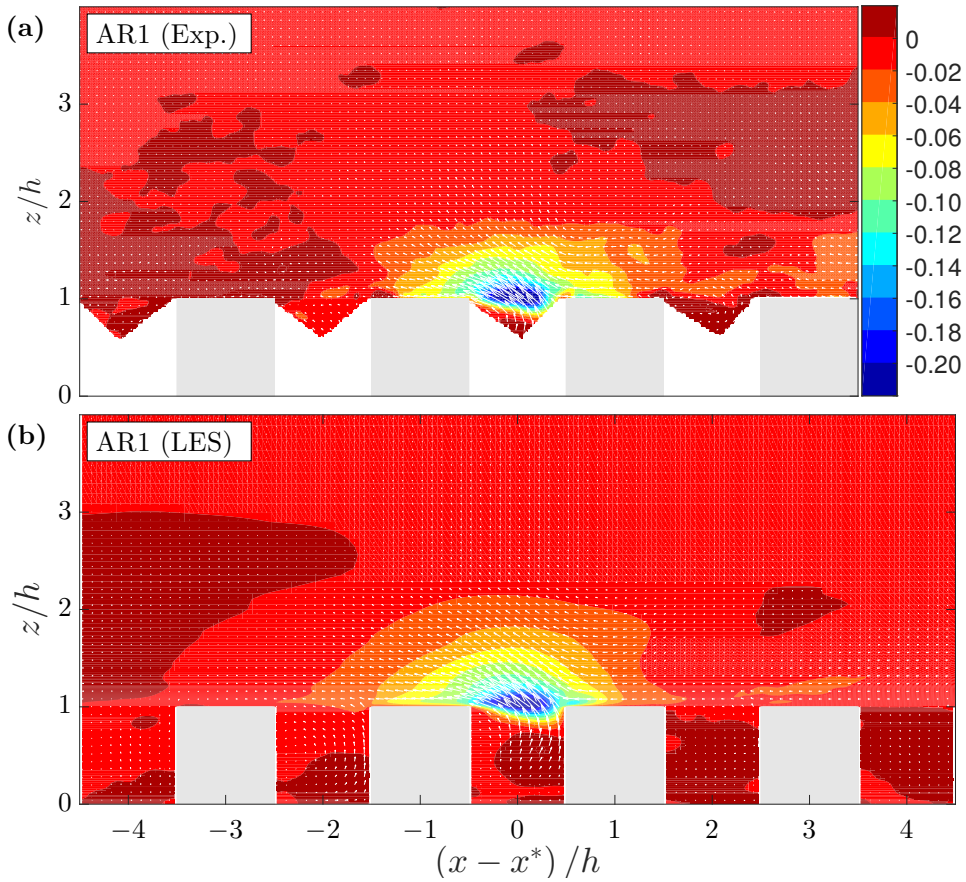

Figure 5.15: Mean fluctuating velocity field $\overline{u_i'^{\mathrm{e}}}$ associated with $\langle wc \rangle_{\mathrm{e}} = 0.1 U_h \langle \overline{c} \rangle$ from linear stochastic estimation for case AR1. Contours of $\overline{u'^{\mathrm{e}}}/U_h$ are shown together with the vector field $(\overline{u'^{\mathrm{e}}}, \overline{w'^{\mathrm{e}}})$ in the $y = 0$ plane for the experiment in street 6 (a), while for the LES the average result of street 6 to street 21 is shown (b). The average streamwise location of the event is indicated by x^*.

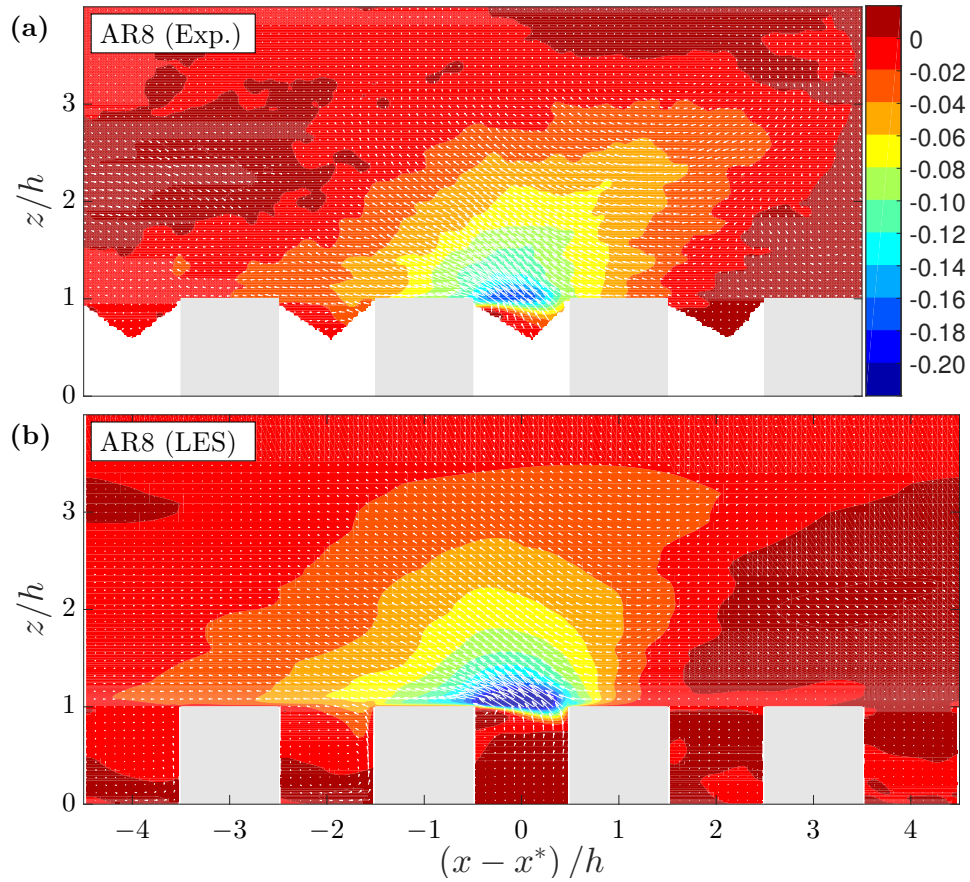

Figure 5.16: Mean fluctuating velocity field $\overline{u_i'^{\mathrm{e}}}$ associated with $\langle wc \rangle_{\mathrm{e}} = 0.1 U_h \langle \overline{c} \rangle$ from linear stochastic estimation for case AR8. Contours of $\overline{u'^{\mathrm{e}}}/U_h$ are shown together with the vector field $(\overline{u'^{\mathrm{e}}}, \overline{w'^{\mathrm{e}}})$ in the $y = 0$ plane for the experiment in street 6 (a), while for the LES the average result of street 6 to street 21 is shown (b). The average streamwise location of the event is indicated by x^*.

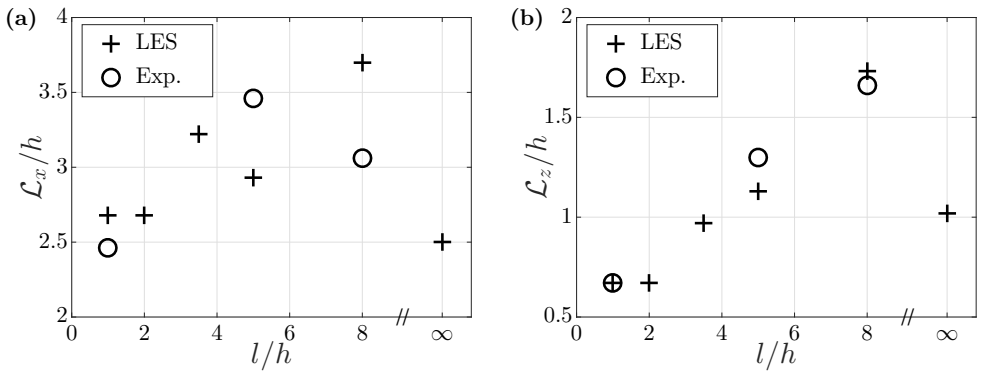

Figure 5.17: Length scales of the contour $\overline{u'^e} = -0.04U_h$ in the plane $y = 0$ for different aspect ratios l/h; (a) streamwise length just above the canopy $\mathcal{L}_x$ and (b) maximum height above the obstacles $\mathcal{L}_z$.

the length of the vectors). In Fig. 5.18 $\overline{w'^e}$ is shown by the contours, while $\overline{u'^e}$ and $\overline{v'^e}$ are shown by the vectors. Cases AR1 and AR2 clearly show a horizontal inflow from the adjacent streamwise streets and even from the neighbouring street canyons to balance the outflow at the top the street canyon. For these cases the region of positive $\overline{w'^e}$ even extends around the obstacle. In the other cases (AR3.5, AR5, AR8, and 2D) outflux in the middle of the top of the street canyon is balanced by inflow within the region of the street canyon itself, such that the velocity fluctuation field looks similar for cases AR3.5 to 2D. The contours of $\overline{w'^e}$ indicate that in all cases the event influences the flow in one or two upstream street canyons.

5.5 CONCLUSIONS

Large-eddy simulations as well as simultaneous PIV and LIF measurements were employed to investigate flow and pollutant dispersion behaviour in regions where the surface changes from rural to urban type roughness. The influence of the aspect ratio of the obstacles, which make up the urban canopy, was investigated for the case of approaching flow over a smooth wall at a roughness Reynolds number, h^+, of 194 for the simulations and 213 for the experiments. The results show that the two methods independently predict practically the same velocity statistics. Furthermore, minor differences in the region of the first row of obstacles can be attributed to the accuracy of both methods and slight differences in the generated smooth-wall boundary layers. The concentation statistics show some differences at the start of the canopy due to a slight non-uniformity in the emission source in the experiment. Nevertheless, qualitatively there is a good agreement between the methods, and the same dispersion mechanisms are identified.

The force balance from the simulations shows that for all cases, except one, after approximately eight streets the surface forces have adapted to the surface roughness.

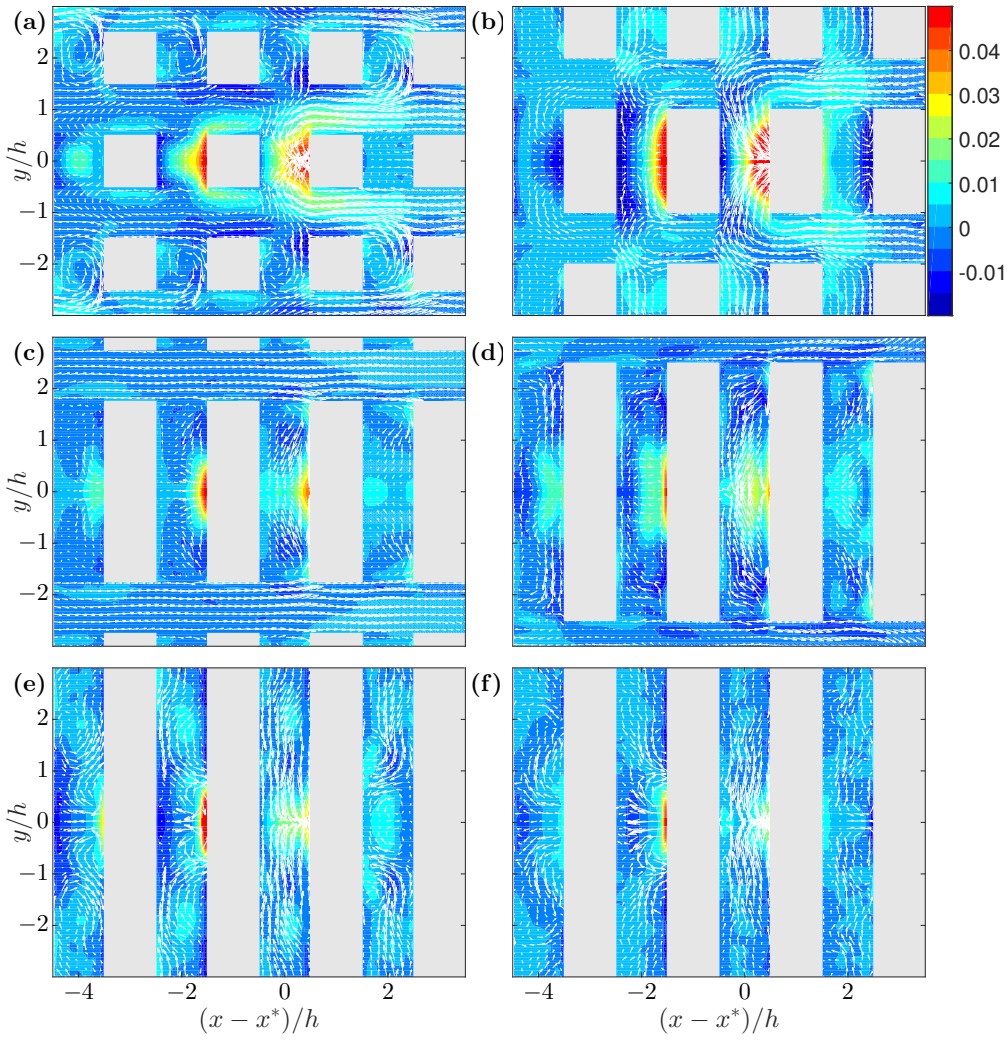

Figure 5.18: Mean fluctuating velocity field $\overline{u_i'^{\mathrm{e}}}/U_h$ associated with $\langle wc \rangle_{\mathrm{e}} = 0.1 U_h \langle \bar{c} \rangle$ from linear stochastic estimation for cases AR1 (a), AR2 (b), AR3.5 (c), AR5 (d), AR8 (e), and 2D (f). Contours of $\overline{w'^{\mathrm{e}}}/U_h$ are shown together with the vector field $(\overline{u'^{\mathrm{e}}}, \overline{w'^{\mathrm{e}}})$ in the $z/h = 0.5$ plane. The average result of street 6 to street 21 is shown, while use is made of symmetry. The average streamwise location of the event is indicated by x^*.

However, for $l/h = 2$ the surface forces are still developing at $x = 46h$ (which is the end of the considered numerical domain) due to the occurrence of large-scale secondary flow. As a consequence, the roughness length z_0 and the zero-plane displacement height d^*, as used in the standard log-law parameterization, are discontinuous when plotted against l/h. It is hypothesized that this phenomenon occurs because for $l/h = 2$ the spacing of the roughness elements is proportional to $\delta_i - h$, analogous to conlusions by Vanderwel and Ganapathisubramani (2015). As to whether or not this large-scale secondary flow eventually disappears, as the internal boundary layer grows, remains an open question. Nonetheless, it is concluded that estimating u_τ by using $\overline{u'w'}$ from single plane measurements only, can be inaccurate due to the spanwise variation caused by this secondary flow. In addition, it is found that with $l/h > 2$ the surface drag decreases as the flow is characterized to a larger extent by the skimming flow regime.

The effect of the roughness transition on pollutant dispersion is that the mean vertical pollutant flux at the top of the street canyons is dominated by the advective pollutant flux $\overline{w}\,\overline{c}$ in the first three streets, after which the profiles of $\overline{w}\,\overline{c}$ and $\overline{w'c'}$ along the streamwise extent of the street canyons become similar to those for the fully-developed cases described by Michioka et al. (2014). Likewise, the JPDFs of streamwise velocity fluctuation u' and instantaneous vertical pollutant flux wc have a comparable shape from the fourth street onwards. In addition, it is found that, in agreement with Michioka et al. (2014), the JPDFs are qualitatively similar for all considered l/h, showing that street canyon ventilation of pollutant is mostly associated with $u' < 0$.

Subsequently, the flow structure that is responsible for street canyon ventilation was identified by means of linear stochastic estimation. It is found that for larger l/h street canyon ventilation is associated with larger regions of $u' < 0$, and that their vertical length scale increases linearly with increasing l/h. However, the result for the 2D case does not result in the largest structure. In addition, during such a ventilation event the flow structure inside the urban canopy shows more variation in the horizontal plane for $l/h = 1$ and $l/h = 2$ than for larger aspect ratios, for which the variation is confined mostly to the considered street canyon.

5.6 ACKNOWLEDGEMENTS

All experimental measurements in this study were performed by Jerke Eisma. The author is grateful for his contributions to this chapter. This study was done within the STW project DisTUrbE (project no. 11989) using the computational resources of SURFsara with the funding of the Netherlands Organisation for Scientific Research (NWO), project no. SG-015.

6

CONCLUSIONS & PERSPECTIVES

Because this thesis is based on journal papers the conclusions of each study have been treated in the corresponding chapters. Therefore, those conclusions will not be repeated here. Instead, the conclusions drawn from the research as a whole are presented and perspectives on future research and developments are given.

6.1 OBSTACLE-RESOLVING LARGE-EDDY SIMULATION

A model has been developed that is capable of simulating turbulent flow and pollutant dispersion in urban environments. By extending the LES model with an immersed boundary method the flow around obstacles could be accurately resolved, while maintaining the advantage of using a direct solver for the pressure equation (Eq. 2.18). In addition, methods to generate realistic turbulent velocity and temperature boundary layers were implemented, such that streamwise developing situations could be studied. These developments allowed for the investigation of the flow and dispersion in regions where the character of the surface roughness changes from a rural to an urban type of roughness. The model proved to accurately capture the relevant physics as comparisons of the results with data acquired from experiments showed good agreement.

When the flow and dispersion inside the urban canopy is the focus of interest the use of experimental methods can be challenging; optical methods like PIV and LIF suffer from shadows and reflections induced by the obstacles. The LES model has the advantage that (instantaneous) three-dimensional flow fields and concentration fields can be easily obtained. Moreover, generating and maintaining stably stratified conditions in experiments is a challenging task; the scarcity of available experimental data is indicative of this difficulty. Therefore, LES modelling can be a very useful tool to gain more insight in stratified flows.

If realistic urban geometries are to be investigated in detail, the currently employed IBM might not be ideal since the geometry needs to coincide with the coordinate lines. However, there are other IBMs that allow for full geometric variation by interpolating the IBM forces to the points where the equations are evaluated (Mittal and Iaccarino, 2005). However, these methods have the drawback that fluxes can only be prescribed approximately, and not exactly, as in the currently employed IBM.

6.2 REYNOLDS NUMBER AND LENGTH SCALES

Although earlier studies showed that the influence of the Reynolds number on the mean flow over sharp-edged obstacles is small if $\mathrm{Re} = U_\infty h/\nu \gtrsim 4 \times 10^3$ (Huppertz and Fernholz, 2002; Castro, 1979; Cheng and Castro, 2002b), it is recommended to verify this for the cases considered in this thesis (where $\mathrm{Re} = 5 \times 10^3$ is used).

Furthermore, in this study the approaching rural flow is assumed to be in approximate equilibrium, i.e. the turbulent velocity fluctuations are in equilibrium with the mean flow. Although the employed recycling method satisfies this condition, the simulations can be made more realistic if situations are investigated where the ratio of the obstacle height to the boundary-layer height is smaller than 0.1, which is used in this study. This would approach real-life conditions, especially for neutral stability, where this ratio can be in the order of 0.01. However, such a study would imply considering a boundary layer at a much larger Reynolds number in order to keep the Reynolds number based on the obstacle height the same. The required computational resources for such an LES are beyond current capabilities. Still, if the flow in the regions near walls is modelled by using 'wall functions', this investigation can be feasible. Concluding, increasing the Reynolds numbers would increase the logarithmic region of the mean velocity profile, which allows for an investigation of internal boundary-layer growth rates that occur in reality.

6.3 PARAMETERIZATION OF THE FLOW BASED ON ROUGHNESS TOPOLOGY

Because the obstacles that make up urban environments vary greatly in size and shape it is difficult to capture urban roughness characteristics in a parameterized model for the flow. Besides that, ideally such a parameterization should also take into account the influence of the wind direction, as well as atmospheric conditions. For neutral conditions parameterization is commonly done by means of the 'law of the wall' (Eqs. 4.5), such that the effect of roughness is reduced to a zero-plane displacement (d^*) and a roughness length (z_0). As was shown in Chapter 5 for a regular array of obstacles, varying the spanwise aspect ratio of the obstacles (l/h) results in a maximum surface drag for $l/h = 2$ caused by a large-scale secondary flow. As a result z_0 shows a local maximum when plotted agains l/h. This discontinuity is not predicted by parameterized models, such as proposed by Macdonald et al. (1998) and Belcher et al. (2003). It is striking that a small variation in the geometry of a regular roughness array can have such a large-scale effect. Therefore, it is argued that a parameterization based on few geometric characteristics of the roughness array might be inadequate to predict u_τ, z_0, and d for all types of urban roughness.

6.4 STRATIFICATION EFFECTS

As discussed in Chapter 1 practical dispersion models can take into account obstacles reasonably well as long as the flow is not stratified. In turn, for stratified flows mean

dispersion can be predicted by Gaussian plume modelling as long as no obstacles are present. However, when the combination of obstacles and stable conditions is considered, both type of methods cannot be used. Therefore, the combination of obstacles and stable conditions is a rather unexplored field. The LES model developed in this study allowed for a detailed study on this topic. It showed that for flow over a single two-dimensional obstacle as well as for flow over an array of cubical obstacles stably stratified boundary layers require much longer distances to adapt to a change in surface roughness than neutral boundary layers. Moreover, the flow cannot be considered effectively neutral, as is often assumed in urban dispersion studies.

The mechanisms that make up pollutant dispersion are not fundamentally different for stable conditions. Nevertheless, compared to neutral conditions the concentrations in the canopy are higher due to a lower mean advection velocity. In addition, in rural-to-urban cases pollutants emitted close to the ground are contained in the internal boundary layer, which grows less rapidly in stable conditions. This is a second cause for higher concentrations in stable conditions.

Finally, it is recommended to do real-life measurements in (rural-to-)urban environments to determine what kind of thermal boundary conditions represent urban environments best, and to verify the stratification effects found in this research.

6.5 TRANSLATION TO FULL-SCALE APPLICATIONS

In the simulations the internal boundary layer induced by the rural-to-urban transition affected pollutant dispersion farther than the end of the considered domain, which extended up to a distance of 48 times the height of the obstacles downstream of the start of the urban canopy. If we apply these results to cities where the buildings have an average height in the order of 10 m, this means that the rural-to-urban transition can influence urban air quality up to distances greater than 0.5 km from the edge of the city. Moreover, this distance increases with higher levels of atmospheric stability, as discussed in the previous section.

Furthermore, especially near the transition the layout of the buildings that make up the city has a large influence on the mean concentration in the urban canopy. This is mainly determined by the level of blockage of the flow, which influences the initial internal boundary-layer growth. It is recommended to further investigate the influence of roughness geometry on urban air quality in order to eventually take into account these effects during urban planning.

6.6 FUTURE URBAN DISPERSION MODELS

Recently, first steps were made in using so-called 'turbulence-resolving' methods for weather and climate simulation (Schalkwijk, 2015). With increasing computational resources 'roughness-resolving' methods, such as used in this thesis, will eventually become feasible within the same framework. Nevertheless, at the moment less

resource-demanding models have to be developed for urban dispersion. Therefore, here the conditions for such a model are given.

First of all, in reality the surface roughness is generally not homogeneous and its character can change within horizontal length scales that are smaller than the boundary-layer depth. This means that the flow in and just above the urban canopy is continuously adapting to a new roughness, while the outer flow is practically unaltered, apart from a vertical displacement due to the presence of the canopy. Each change in roughness induces a new internal boundary layer with a corresponding interface that bounds the region of the flow that is affected by the new roughness. Pollutants are also bounded by these regions, as shown in Chapters 4 and 5. Consequently, requirements for an accurate dispersion model are a good prediction of the location of these interfaces, and the ability to consider streamwise developing flow. Basically, such a model would be a practical extension of the theoretical considerations on self-preserving velocity deviations by Townsend (1965). Less computationally demanding methods than LES, such as computational fluid dynamics models (CFD) based on the Reynolds-averaged Navier-Stokes (RANS) equations, could be used to resolve the surface roughness. It is recommended to investigate whether RANS models predict the internal boundary-layer growth correctly, especially for stable flows. Nevertheless, by definition RANS models can only be used to predict the mean flow and mean pollutant dispersion.

A more advanced approach would be to take into account the dominating flow structures that make up dispersion, such as those found in Chapter 5, through the use of linear stochastic estimation. Methods for so-called 'reduced-order modelling' (ROM), such as *proper orthogonal decomposition* (Berkooz et al., 1993), can be used to represent the temporal behaviour of the flow by its most dominant modes without solving the full physics. ROM has the advantage that the required computational resources are only a fraction of those for the full LES. The periodic character of the instantaneous spanwise velocity component shown in Fig. 5.4 illustrates that a dominant mode occurs in the cases considered in Chapter 5, which indicates that such an approach might be successful. In view of a practical dispersion model it is recommended to study the performance of ROM methods derived from an urban LES. In addition, it is proposed to investigate how many LES realizations are required to set up a ROM framework that can describe flow and pollutant dispersion for an urban region in practical conditions, e.g. for various wind directions and atmospheric conditions.

In conclusion, the work presented in this thesis shows that urban dispersion can be simulated by means of obstacle-resolving LES, while taking into account atmospheric stability. Perspectives are given on future developments, such that the knowledge gained from this research can be implemented in new generation practical models for urban dispersion.

A

STATISTICS OF THE INFLOW BOUNDARY LAYERS

TWO-POINT CORRELATIONS, INTEGRAL LENGTH SCALES, AND ENERGY SPECTRA

In this supplementary material it is checked if the horizontal domain size of the driver simulations used in Chapter 3 is sufficient to accurately generate the inflow boundary layers. Figure A.1 shows the streamwise two-point correlation for each velocity component, defined as $R_{u_i u_i}(r) = \overline{u_i'(x)\, u_i'(x+r)}$, for BL0 (neutral) and BL2 (stable). The data was taken along a streamwise line at $z/\delta_0 = 0.16$. For both cases the streamwise two-point correlation drops to approximately zero before half of the domain length is reached. The correlations for the stable boundary layer decrease more rapidly than for the neutral case. The corresponding streamwise integral length scales, l_x^{uu}, l_x^{vv}, and l_x^{ww} are defined as:

$$l_x^{u_i u_i} = \frac{1}{R_{u_i u_i}(0)} \int_0^{\frac{1}{2}L_x} R_{u_i u_i}(r)\, dx \tag{A.1}$$

The vertical distributions of l_x^{uu}, l_x^{vv}, and l_x^{ww} are plotted in Fig. A.2 for both BL0 and BL2. From $z = 0 - 0.8\delta$ the streamwise integral length scale l_x^{uu} is significantly smaller for the stable case than for the neutral case.

Figure A.3 shows the spanwise two-point correlation for each velocity component, defined as $R_{u_i u_i}(r) = \overline{u_i'(y)\, u_i'(y+r)}$, for BL0 (neutral) and BL2 (stable). The data was taken along a spanwise line at $z/\delta_0 = 0.16$. At half of the domain width the absolute value of the spanwise two-point correlation has dropped below 0.07 for all three velocity components. The corresponding spanwise integral length scales, l_y^{uu}, l_y^{vv}, and l_y^{ww} are listed in Table A.1. They are defined as:

$$l_y^{u_i u_i} = \frac{1}{R_{u_i u_i}(0)} \int_0^{\frac{1}{2}L_y} R_{u_i u_i}(r)\, dy \tag{A.2}$$

The largest integral length scale occured for $\overline{v'v'}$ for neutral conditions ($l_y^{vv} = 0.086\delta$). At least 18 spanwise integral length scales l_y^{vv} fit the domain. Comparing with the streamwise integral length scales it is not expected that the spanwise integral length scales will increase significantly with height. Using the criterion that at least 5 integral length scales should fit the domain, the spanwise dimension of the domain can be considered sufficiently large.

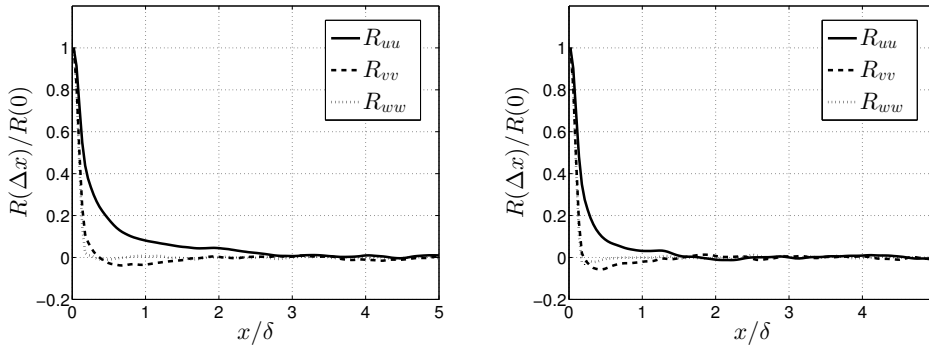

Figure A.1: Streamwise two-point correlation for simulations (a) BL0 (Ri = 0.000) and (b) BL2 (Ri = 0.098) at $z/\delta_0 = 0.16$.

	l_y^{uu}/δ	l_y^{vv}/δ	l_y^{ww}/δ
BL0	0.061	0.086	0.043
BL2	0.049	0.062	0.043

Table A.1: Spanwise integral length scales at $z/\delta_0 = 0.16$.

Finally, to check if the grid resolution is adequate Fig. A.4 shows the spanwise energy spectrum, $E(k_y)$, for each velocity component for the BL0 (neutral) and BL2 (stable). The spanwise energy drops five orders of magnitude, which indicates that a large part of the turbulence is resolved.

The presented data demonstrates that the domain size and its resolution are sufficient to accurately capture the relevant flow physics. Also taking into account the good agreement of the first and second order velocity statistics of BL0 with data from the literature (Fig. 3.2 and Fig. 3.3 in Chapter 3), it is concluded that the inflow boundary layers can be considered accurate for this dispersion study.

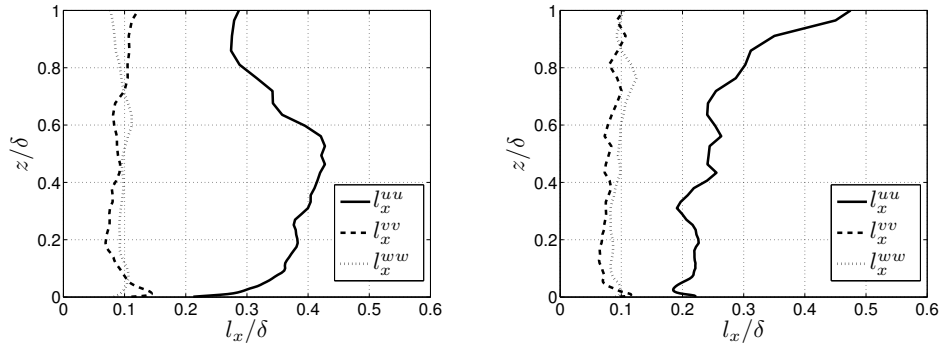

(a) (b)

Figure A.2: Vertical profiles of the streamwise integral length scales for simulations (a) BL0 (Ri = 0.000) and (b) BL2 (Ri = 0.098).

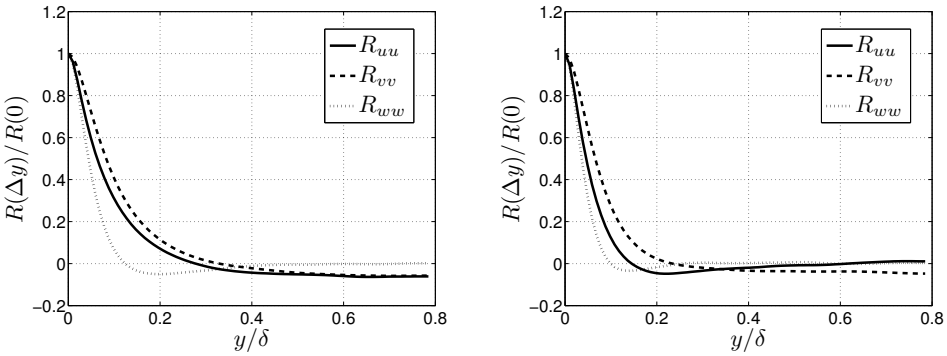

(a) (b)

Figure A.3: Spanwise two-point correlation for simulations (a) BL0 (Ri = 0.000) and (b) BL2 (Ri = 0.098) at $z/\delta_0 = 0.16$.

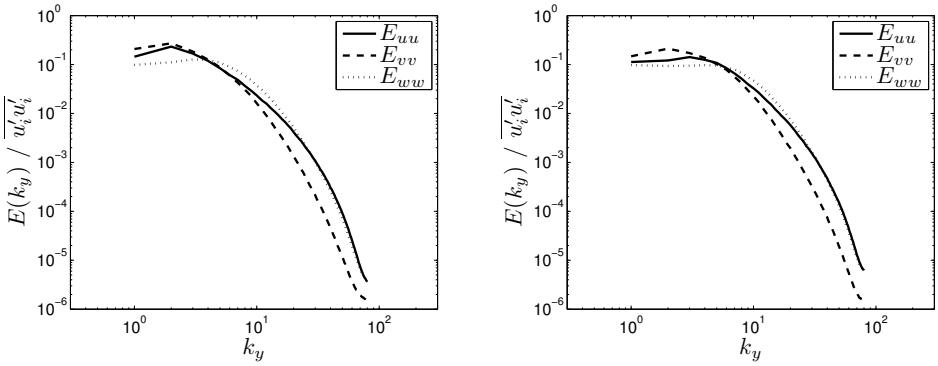

Figure A.4: Spanwise energy spectra for simulations (a) BL0 (Ri = 0.000) and (b) BL2 (Ri = 0.098) at $z/\delta_0 = 0.16$.

REFERENCES

Abdalla, I. E., Yang, Z., and Cook, M. (2009). Computational Analysis and Flow structure of a Transitional Separated-reattached Flow over a Surface Mounted Obstacle and a Forward-facing Step. *Int. J. Comput. Fluid Dyn.*, 23(1):25–57.

Adrian, R. J. (1988). *Linking correlations and structure. Stochastic estimation and conditional averaging*, pages 420–436. Hemisphere Publ Corp, Dubrovnik.

Allwine, J. and Leach, M. (2007). Editorial. *J. Appl. Meteorol. Climatol.*, 46(12):2017–2018.

Bailey, D. (1993). *Computational Frameworks for the Fast Fourier Transform (Charles Van Loan)*, volume 35. Society for Industrial and Applied Mathematics.

Barlow, J. F. (2014). Progress in observing and modelling the urban boundary layer. *Urban Clim.*, 10(P2):216–240.

Barnes, M. J., Brade, T. K., Mackenzie, A. R., Whyatt, J. D., Carruthers, D. J., Stocker, J., Cai, X., and Hewitt, C. N. (2014). Spatially-varying surface roughness and ground-level air quality in an operational dispersion model. *Environ. Pollut.*, 185:44–51.

Belcher, S. E. (2005). Mixing and transport in urban areas. *Philos. Trans. A. Math. Phys. Eng. Sci.*, 363(1837):2947–2968.

Belcher, S. E., Jerram, N., and Hunt, J. C. R. (2003). Adjustment of a turbulent boundary layer to a 'canopy' of roughness elements. *J. Fluid Mech.*, 488:369–398.

Berkooz, G., Holmes, P., and Lumley, J. L. (1993). The Proper Orthogonal Decomposition in the Analysis of Turbulent Flows. *Annu. Rev. Fluid Mech.*, 25(1):539–575.

Berkowicz, R. (2000). OSPM - a parameterised street pollution model. *Environ. Monit. Assess.*, 65(1):323–331.

Blackman, K., Perret, L., and Savory, E. (2015). Effect of upstream flow regime on street canyon flow mean turbulence statistics. *Environ. Fluid Mech.*, 15(4):823–849.

Bohr, E. (2005). *Inflow generation technique for large eddy simulation of turbulent boundary layers*. PhD thesis, Rensselaer Polytechnic Institute, Troy, New York.

Boppana, V. B. L., Xie, Z. T., and Castro, I. P. (2014). Thermal Stratification Effects on Flow Over a Generic Urban Canopy. *Boundary-Layer Meteorol.*, 153(1):141–162.

Boussinesq, J. (1877). *Essai sur la théorie des eaux courantes, Mémoires présentés par divers savants à l'Académie des Science de l'Institut de France, XXIII*. Impremerie nationale, Paris, first edition.

Boussinesq, J. (1903). *Théorie de la chaleur mise en harmonie avec la thermodynamique et avec la théorie méchanique de la lumière*. Impremerie Gauthier-Villars, Paris, vol. 2 edition.

Castro, I. P. (1979). Relaxing wakes behind surface-mounted obstacles in rough wall boundary layers. *J. Fluid Mech.*, 93(04):631–659.

Castro, I. P., Cheng, H., and Reynolds, R. (2006). Turbulence over urban-type roughness: Deductions from wind-tunnel measurements. *Boundary-Layer Meteorol.*, 118(1):109–131.

Cheng, H. and Castro, I. P. (2002a). Near-wall flow development after a step change in surface roughness. *Boundary-Layer Meteorol.*, 105(3):411–432.

Cheng, H. and Castro, I. P. (2002b). Near wall flow over urban-like roughness. *Boundary-Layer Meteorol.*, 104(2):229–259.

Cheng, H., Hayden, P., Robins, A. G., and Castro, I. P. (2007). Flow over cube arrays of different packing densities. *J. Wind Eng. Ind. Aerodyn.*, 95(8):715–740.

Cheng, W. C. and Porté-Agel, F. (2015). Adjustment of Turbulent Boundary-Layer Flow to Idealized Urban Surfaces: A Large-Eddy Simulation Study. *Boundary-Layer Meteorol.*, 155(2):249–270.

Christensen, K. T. and Adrian, R. J. (2001). Statistical evidence of hairpin vortex packets in wall turbulence. *J. Fluid Mech.*, 431:433–443.

Coceal, O., Thomas, T. G., Castro, I. P., and Belcher, S. E. (2006). Mean flow and turbulence statistics over groups of urban-like cubical obstacles. *Boundary-Layer Meteorol.*, 121(3):491–519.

Counihan, J., Hunt, J. C. R., and Jackson, P. S. (1974). Wakes behind two-dimensional surface obstacles in turbulent boundary layers. *J. Fluid Mech.*, 64(03):529.

Crimaldi, J. P. (2008). Planar laser induced fluorescence in aqueous flows. *Exp. Fluids*, 44(6):851–863.

Deardorff, J. (1970). A numerical study of three-dimensional turbulent channel flow at large Reynolds numbers. *J. Fluid Mech.*, 41(02):453–480.

di Mare, L. and Jones, W. P. (2003). LES of turbulent flow past a swept fence. *Int. J. Heat Fluid Flow*, 24(4):606–615.

Eisma, H. E., Tomas, J. M., Pourquie, M. B. J. M., Elsinga, G. E., Jonker, H. J. J., and Westerweel, J. (2016). Effects of a Fence on Pollutant Dispersion in Boundary Layers Exposed to a Rural-to-Urban Transition. *(submitted)*.

Garratt, J. R. (1990). The internal boundary layer - A review. *Boundary-Layer Meteorol.*, 50(1-4):171–203.

Heus, T., Van Heerwaarden, C. C., Jonker, H. J. J., Pier Siebesma, A., Axelsen, S., Van Den Dries, K., Geoffroy, O., Moene, A. F., Pino, D., De Roode, S. R., and Vilà-Guerau de Arellano, J. (2010). Formulation of the Dutch Atmospheric Large-Eddy Simulation (DALES) and overview of its applications. *Geosci. Model Dev.*, 3(2):415–444.

Hundsdorfer, W., Koren, B., Van Loon, M., and Verwer, J. G. (1995). A Positive Finite-Difference Advection Scheme. *J. Comput. Phys.*, 117(1):35–46.

Huppertz, A. and Fernholz, H. H. (2002). Active control of the turbulent flow over a swept fence. *Eur. J. Mech. B/Fluids*, 21(4):429–446.

Irwin, H. P. A. H. (1981). The design of spires for wind simulation. *J. Wind Eng. Ind. Aerodyn.*, 7(3):361–366.

Jackson, P. S. (1981). On the displacement height in the logarithmic velocity profile. *J. Fluid Mech.*, 111:15–25.

Jonker, H. J. J., van Reeuwijk, M., Sullivan, P. P., and Patton, E. G. (2013). On the scaling of shear-driven entrainment: a DNS study. *J. Fluid Mech.*, 732:150–165.

Joshi, P., Liu, X., and Katz, J. (2014). Effect of mean and fluctuating pressure gradients on boundary layer turbulence. *J. Fluid Mech.*, 748:36–84.

Kaltenbach, H. J. and Janke, G. (2000). Direct numerical simulation of flow separation behind a swept, rearward-facing step at Re_H=3000. *Phys. Fluids*, 12(9):2320–2337.

Kanda, M., Moriwaki, R., and Kasamatsu, F. (2004). Large-eddy simulation of turbulent organized structures within and above explicity resolved cube arrays. *Boundary-Layer Meteorol.*, 112(2):343–368.

Kolmogorov, A. N. (1991). The local structure of turbulence in incompressible viscous fluid for very large Reynolds numbers. *Proc. Math. Phys. Sci.*, 434(1890):9–13.

Kong, H., Choi, H., and Lee, J. S. (2000). Direct numerical simulation of turbulent thermal boundary layers. *Phys. Fluids*, 12(10):2555–2568.

Kothari, K. M., Peterka, J. A., and Meroney, R. N. (1986). Perturbation analysis and measurements of building wakes in a stably stratified turbulent boundary layer. *J. Wind Eng. Ind. Aerodyn.*, 25(1):49–74.

Krug, D., Holzner, M., Lüthi, B., Wolf, M., Tsinober, A., and Kinzelbach, W. (2014). A combined scanning PTV/LIF technique to simultaneously measure the full velocity gradient tensor and the 3D density field. *Meas. Sci. Technol.*, 25(6):065301.

Lee, J. H., Sung, H. J., and Krogstad, P.-Å. (2011). Direct numerical simulation of the turbulent boundary layer over a cube-roughened wall. *J. Fluid Mech.*, 669:397–431.

Lilly, D. K. (1962). On the numerical simulation of buoyant convection. *Tellus*, 14(2):148–172.

Lund, T. S., Wu, X., and Squires, K. D. (1998). On the Generation of Turbulent Inflow Conditions for Boundary Layer Simulations. *J. Comput. Phys.*, 140(2):233–258.

Macdonald, R. W. (2000). Modelling the mean velocity profile in the urban canopy layer. *Boundary-Layer Meteorol.*, 97(1):25–45.

Macdonald, R. W., Griffiths, R. F., and Hall, D. J. (1998). An improved method for the estimation of surface roughness of obstacle arrays. *Atmos. Environ.*, 32(11):1857–1864.

Mason, P. J. and Callen, N. S. (1986). On the magnitude of the subgrid-scale eddy coefficient in large-eddy simulations of turbulent channel flow. *J. Fluid Mech.*, 162:439–462.

Michioka, T., Sato, A., Takimoto, H., and Kanda, M. (2011). Large-Eddy Simulation for the Mechanism of Pollutant Removal from a Two-Dimensional Street Canyon. *Boundary-Layer Meteorol.*, 138(2):195–213.

Michioka, T., Takimoto, H., and Sato, A. (2014). Large-Eddy Simulation of Pollutant Removal from a Three-Dimensional Street Canyon. *Boundary-Layer Meteorol.*, 150(2):259–275.

Minister VROM (2007). Regeling Beoordeling Luchtkwaliteit. *Minist. van Volkshuisvesting, Ruimtelijke Ordening en Milieubeheer*, (LMV 2007.109578).

Mittal, R. and Iaccarino, G. (2005). Immersed Boundary Methods. *Annu. Rev. Fluid Mech.*, 37(1):239–261.

Monin, A. S. and Obukhov, A. M. (1954). Basic laws of turbulent mixing in the surface layer of the atmosphere. *Contrib. Geophys. Inst. Acad. Sci. USSR*, 24(151):163–187.

Obukhov, A. M. (1971). Turbulence in an atmosphere with a non-uniform temperature. *Boundary-Layer Meteorol.*, 2(1):7–29.

Ogawa, Y. and Diosey, P. G. (1980). Surface roughness and thermal stratification effects on the flow behind a two-dimensional fence-II. A wind tunnel study and similarity considerations. *Atmos. Environ.*, 14(11):1309–1320.

Oke, T. R. (1988). Street design and urban canopy layer climate. *Energy Build.*, 11(1-3):103–113.

Orellano, A. and Wengle, H. (2000). Numerical simulation (DNS and LES) of manipulated turbulent boundary layer flow over a surface-mounted fence. *Eur. J. Mech. B/Fluids*, 19(5):765–788.

Pope, S. B. (2000). *Turbulent Flows*, volume 1. Cambridge University Press.

Pourquie, M., Breugem, W. P., and Boersma, B. J. (2009). Some Issues Related to the Use of Immersed Boundary Methods to Represent Square Obstacles. *Int. J. Multiscale Comput. Eng.*, 7(6):509–522.

Prasad, A. K. and Jensen, K. (1995). Scheimpflug stereocamera for particle image velocimetry in liquid flows. *Appl. Opt.*, 34(30):7092–7099.

Projectgroep Revisie Nationaal Model (1998). *Het Nieuwe Nationaal Model*. InfoMil, Den Haag, 2002 edition.

Raupach, M. R., Antonia, R. A., and Rajagopalan, S. (1991). Rough-Wall Turbulent Boundary Layers. *Appl. Mech. Rev.*, 44(1):1–25.

Reynolds, R. T. and Castro, I. P. (2008). Measurements in an urban-type boundary layer. *Exp. Fluids*, 45(1):141–156.

Roberts, O. F. T. (1923). The Theoretical Scattering of Smoke in a Turbulent Atmosphere. *Proc. R. Soc. London A Math. Phys. Eng. Sci.*, 104(728):640–654.

Savory, E., Perret, L., and Rivet, C. (2013). Modelling considerations for examining the mean and unsteady flow in a simple urban-type street canyon. *Meteorol. Atmos. Phys.*, 121(1-2):1–16.

Scarano, F. (2003). Theory of non-isotropic spatial resolution in PIV. *Exp. Fluids*, 35(3):268–277.

Schalkwijk, J. (2015). *Toward Turbulence-resolving Weather and Climate Simulation*. PhD thesis, Delft University of Technology.

Schofield, W. H. and Logan, E. (1990). Turbulent shear flow over surface mounted obstacles. *J. Fluid Eng.*, 112(4):376–385.

Schrijvers, P., Jonker, H., Kenjereš, S., and de Roode, S. (2015). Breakdown of the night time urban heat island energy budget. *Build. Environ.*, 83:50–64.

Schumann, U. (1975). Subgrid scale model for finite difference simulations of turbulent flows in plane channels and annuli. *J. Comput. Phys.*, 18(4):376–404.

Sillero, J. A., Jiménez, J., and Moser, R. D. (2013). One-point statistics for turbulent wall-bounded flows at Reynolds numbers up to $\delta^+ \approx 2000$. *Phys. Fluids*, 25(10):105102.

Smagorinsky, J. (1963). General Circulation Experiments With the Primitive Equations. *Mon. Weather Rev.*, 91(3):99–164.

Smart, P. L. and Laidlaw, I. M. S. (1977). An evaluation of some fluorescent dyes for water tracing. *Water Resour. Res.*, 13(1):15–33.

Soulhac, L., Salizzoni, P., Cierco, F.-X., and Perkins, R. (2011). The model SIRANE for atmospheric urban pollutant dispersion; part I, presentation of the model. *Atmos. Environ.*, 45(39):7379–7395.

Stull, R. B. (1988). *An Introduction to Boundary Layer Meteorology*, volume 13. Springer Netherlands.

Sweet, R. A. (1974). A Generalized Cyclic Reduction Algorithm. *SIAM J. Numer. Anal.*, 11(3):506–520.

Tennekes, H. and Lumley, J. L. (1972). *A first course in turbulence*. MIT Press.

Tomas, J. M., Eisma, H. E., Pourquie, M. J. B. M., Elsinga, G. E., Jonker, H. J. J., and Westerweel, J. (2016a). Pollutant Dispersion in Boundary Layers Exposed to Rural-to-Urban Transitions: Varying the Spanwise Length Scale of the Roughness. *(under review)*.

Tomas, J. M., Pourquie, M. J. B. M., Eisma, H. E., Elsinga, G. E., Jonker, H. J. J., and Westerweel, J. (2015a). Pollutant dispersion in the urban boundary layer. In Fröhlich, J., Kuerten, H., Geurts, B. J., and Armenio, V., editors, *Direct and Large-Eddy Simulation 9 Workshop*, pages 435–441. Springer.

Tomas, J. M., Pourquie, M. J. B. M., Eisma, H. E., and Jonker, H. J. J. (2015b). Pollutant Dispersion in Neutral and Stable Boundary Layers Entering an Urban Environment. In *Proc. TSFP-9*, volume 3, pages 1–6, Melbourne, Australia.

Tomas, J. M., Pourquie, M. J. B. M., and Jonker, H. J. J. (2015c). The influence of an obstacle on flow and pollutant dispersion in neutral and stable boundary layers. *Atmos. Environ.*, 113:236–246.

Tomas, J. M., Pourquie, M. J. B. M., and Jonker, H. J. J. (2016b). Stable Stratification Effects on Flow and Pollutant Dispersion in Boundary Layers Entering a Generic Urban Environment. *Boundary-Layer Meteorol.*, 159(2):221–239.

Tomas, J. M., van der Weide, E. T. A., de Vries, H., and Hoeijmakers, H. W. M. (2010). Numerical simulation of flow control by synthetic jet actuation. In *27th Congr. Int. Counc. Aeronaut. Sci.*, Nice, France.

Tominaga, Y. and Stathopoulos, T. (2013). CFD simulation of near-field pollutant dispersion in the urban environment: A review of current modeling techniques. *Atmos. Environ.*, 79:716–730.

Townsend, A. A. (1965). Self-preserving flow inside a turbulent boundary layer. *J. Fluid Mech.*, 22(4):773–797.

Townsend, A. A. (1966). The flow in a turbulent boundary layer after a change in surface roughness. *J. Fluid Mech.*, 26(02):255.

Trifonopoulos, D. A. and Bergeles, G. C. (1992). Stable stratification effects on the flow past surface obstructions: A numerical study. *Int. J. Heat Fluid Flow*, 13(2):151–159.

Turner, J. S. (1973). *Buoyancy effects in fluids*. Cambridge Monographs on Mechanics. Cambridge University Press, London.

United Nations (2014). World Urbanization Prospects: The 2014 Revision, Highlights (ST/ESA/SER.A/352). Technical report, United Nations.

Vanderwel, C. and Ganapathisubramani, B. (2015). Effects of spanwise spacing on large-scale secondary flows in rough-wall turbulent boundary layers. *J. Fluid Mech.*, 774:R2.

Vinçont, J.-Y., Simoëns, S., Ayrault, M., and Wallace, J. M. (2000). Passive scalar dispersion in a turbulent boundary layer from a line source at the wall and downstream of an obstacle. *J. Fluid Mech.*, 424:127–167.

Vreman, A. W. (2004). An eddy-viscosity subgrid-scale model for turbulent shear flow: Algebraic theory and applications. *Phys. Fluids*, 16(10):3670–3681.

Westerweel, J., Fukushima, C., Pedersen, J. M., and Hunt, J. C. R. (2009). Momentum and scalar transport at the turbulent/non-turbulent interface of a jet. *J. Fluid Mech.*, 631(2009):199–230.

Westerweel, J. and Scarano, F. (2005). Universal outlier detection for PIV data. *Exp. Fluids*, 39(6):1096–1100.

Wicker, L. J. and Skamarock, W. C. (2002). Time-Splitting Methods for Elastic Models Using Forward Time Schemes. *Mon. Weather Rev.*, 130(8):2088–2097.

Wood, C. R., Lacser, A., Barlow, J. F., Padhra, A., Belcher, S. E., Nemitz, E., Helfter, C., Famulari, D., and Grimmond, C. S. B. (2010). Turbulent Flow at 190 m Height Above London During 2006-2008: A Climatology and the Applicability of Similarity Theory. *Boundary-Layer Meteorol.*, 137(1):77–96.

ACKNOWLEDGEMENTS

I enjoyed doing my PhD research. At times it was difficult and almost nerve-wracking, but that made the satisfaction even greater when goals were reached. I especially enjoyed to be surrounded by people who challenge themselves by doing research. Following their achievements and personal developments was inspiring, and I am grateful that I have been part of this group of researchers for over four years.

I would like to thank some people that contributed to the realization of this thesis. First of all, I would like to thank my promotor, Harm Jonker. The discussions we had and the suggestions you gave were very helpful. I really appreciate your ability to take a step back and describe a problem or phenomenon in essence. I believe this talent will also make you a successful entrepreneur. I am very grateful for the time I spent with my copromotor Mathieu Pourquie. Mathieu, I enjoyed learning from you about fluid dynamics and numerical methods, but just as much I enjoyed your stories about our lab and about the history of mankind. Jerry and Gerrit, your expertise in turbulence and experimental techniques is admirable and I learned a lot from you. Jerke, my experimental partner in research, we worked closely together the last year and I can honestly say that this was the most enjoyable time of my PhD. I am very grateful for your contribution to this thesis. My roommates, Jeanette, Marc, Sita, Gem, Dries, Marieke, Manu, and Florian, thank you for enduring my lectures on all kinds of topics and for being such great company. I would like to thank our secretaries, Caroline and Ria, for making everything go smoothly in the lab. Martijn and Sander, it was a great experience to supervise you during your Master research and I wish you all the best in your careers. In addition, I would like to thank everybody in the Laboratory for Aero- and Hydrodynamics as well as in the Clouds, Climate & Air Quality group for the inspiring article discussions, lunch talks, and coffee breaks. I appreciate the efforts of all the Panta Rhei board members. Of course, my dear paranimfs, Timo and Coen, thank you for our friendship and for standing by my side on this exciting day.

Papa, mama, Sonja, Sjoerd, Şahin en Annemieke, ik vind het heel fijn dat jullie altijd voor mij klaar staan. Papa en mama, ik voel me verzekerd van jullie onvoorwaardelijke steun en daar ben ik jullie heel dankbaar voor. Marc, Diet, Marjolein, Thijs, Annemarie, Roland, Laura, Gilles, Aleid, Charlotte en Pim, ik prijs me gelukkig met jullie. Heel erg bedankt voor de broodnodige en fijne afleiding van mijn werk. Als laatste wil ik degene noemen aan wie ik het meeste te danken heb. Claartje, ik ben je heel erg dankbaar voor je steun en geduld de afgelopen jaren.

ABOUT THE AUTHOR

Jasper Tomas was born on March 22 1985 in Leiden. After completing his secondary education at the Stedelijk Gymnasium Leiden in 2003, he started studying Mechanical Engineering at the University of Twente. In 2006 he joined Solar Team Twente with whom he designed and built the solar car 'Twente One' and participated in the World Solar Challenge 2007 in Australia. In 2009 he did a four-month internship at the Italian Aerospace Research Centre (CIRA), where he developed a numerical model to simulate helicopter rotors. In 2010 he obtained a Master of Science degree in Mechanical Engineering under supervision of Dr. ir. E.T.A. van der Weide and Prof. dr. ir. H.W.M. Hoeijmakers. The title of his Master thesis is *Numerical Simulation of Active Flow Control on Airfoils*. After graduating he worked on a temporary research project related to his Master research. Subsequently, he joined the company TMC Physics being employed at the Netherlands Organisation for Applied Scientific Research (TNO), where he developed models that predict heat radiation from fires as well as dispersion of hazardous materials. The latter triggered his interest in the fluid mechanics of urban dispersion. In February 2012 he returned to academia by starting his research on large-eddy simulation of urban flow and dispersion at the Delft University of Technology. The results of that investigation are presented in this thesis. He currently works as a scientific researcher at the National Institute for Public Health and the Environment (RIVM), where he is involved in atmospheric dispersion modelling.

JOURNAL PUBLICATIONS

Eisma, H. E., Tomas, J. M., Pourquie, M. B. J. M., Elsinga, G. E., Jonker, H. J. J., and Westerweel, J. (2016). Effects of a Fence on Pollutant Dispersion in Boundary Layers Exposed to a Rural-to-Urban Transition. *(submitted)*

Tomas, J. M., Eisma, H. E., Pourquie, M. J. B. M., Elsinga, G. E., Jonker, H. J. J., and Westerweel, J. (2016a). Pollutant Dispersion in Boundary Layers Exposed to Rural-to-Urban Transitions: Varying the Spanwise Length Scale of the Roughness. *(under review)*

Tomas, J. M., Pourquie, M. J. B. M., and Jonker, H. J. J. (2016b). Stable Stratification Effects on Flow and Pollutant Dispersion in Boundary Layers Entering a Generic Urban Environment. *Boundary-Layer Meteorol.*, 159(2):221–239

Tomas, J. M., Pourquie, M. J. B. M., and Jonker, H. J. J. (2015c). The influence of an obstacle on flow and pollutant dispersion in neutral and stable boundary layers. *Atmos. Environ.*, 113:236–246

CONFERENCE PROCEEDINGS

Tomas, J. M., Pourquie, M. J. B. M., Eisma, H. E., and Jonker, H. J. J. (2015b). Pollutant Dispersion in Neutral and Stable Boundary Layers Entering an Urban Environment. In *Proc. TSFP-9*, volume 3, pages 1–6, Melbourne, Australia

Tomas, J. M., Pourquie, M. J. B. M., Eisma, H. E., Elsinga, G. E., Jonker, H. J. J., and Westerweel, J. (2015a). Pollutant dispersion in the urban boundary layer. In Fröhlich, J., Kuerten, H., Geurts, B. J., and Armenio, V., editors, *Direct and Large-Eddy Simulation 9 Workshop*, pages 435–441. Springer

Tomas, J. M., van der Weide, E. T. A., de Vries, H., and Hoeijmakers, H. W. M. (2010). Numerical simulation of flow control by synthetic jet actuation. In *27th Congr. Int. Counc. Aeronaut. Sci.*, Nice, France

OTHER SCIENTIFIC CONTRIBUTIONS

Tomas, J. M., Pourquie, M. J. B. M., Eisma, H.E., Jonker, H. J. J., The effect of stable stratification on boundary-layer development and pollutant dispersion behind an obstacle. (poster), *EUROMECH Colloquium 567: Turbulent mixing in stratified flows*, 22-25 March 2015, DAMTP, Centre of Mathematical Sciences, Cambridge, UK

Tomas, J. M., Pourquie, M. J. B. M., Jonker, H. J. J., Pollutant dispersion in neutral and stable boundary layers entering an urban-like environment. (poster), *Physics@FOM*, 20-21 January 2015, Veldhoven, The Netherlands